Silicidation process : Modelling nickel deposition and diffusion from silicide/silicon interfaces through ab initio calculations and machine learning approach

Cesar Andres Jara Donoso

To cite this version:

Cesar Andres Jara Donoso. Silicidation process : Modelling nickel deposition and diffusion from silicide/silicon interfaces through ab initio calculations and machine learning approach. Material chemistry. Université Paul Sabatier - Toulouse III, 2023. English. NNT : 2023TOU30124 . tel-04414908v2

HAL Id: tel-04414908
https://theses.hal.science/tel-04414908v2

Submitted on 24 Jan 2024

Université Fédérale
Toulouse Midi-Pyrénées

THÈSE

En vue de l'obtention du

DOCTORAT DE L'UNIVERSITÉ DE TOULOUSE

Délivré par l'Université Toulouse 3 - Paul Sabatier

Présentée et soutenue par

CESAR ANDRES JARA DONOSO

Le 17 juillet 2023

Procédé de siliciuration : Modélisation du dépôt et de la diffusion du nickel à partir des interfaces siliciure/silicium par des calculs ab initio et une approche d'apprentissage automatique.

Ecole doctorale : **GEETS - Génie Electrique Electronique,Télécommunications et Santé : du système au nanosystème**

Spécialité : **MicroNano Systèmes**

Unité de recherche :
LAAS - Laboratoire d'Analyse et d'Architecture des Systèmes

Thèse dirigée par
Anne HEMERYCK

Jury
Mme Emilie GAUDRY, Rapporteure
M. Guy TREGLIA, Rapporteur
Mme Charlotte BECQUART, Examinatrice
M. Guilhem LARRIEU, Président
M. Julien LAM, Encadrant
Mme Anne HEMERYCK, Directrice de thèse

Contents

Abstract

Procédé de siliciuration du nickel : Modélisation du dépôt et de la diffusion du nickel à partir des interfaces siliciure/silicium par des calculs ab initio et une approche d'apprentissage automatique

Alors que les couches minces de siliciures à base de nickel sont déjà présentes dans de nombreuses applications technologiques de la microélectronique, leurs mécanismes de formation sont encore loin d'être compris et maîtrisés, ce qui rend leur intégration industrielle difficile. Il est montré que le procédé de siliciuration est piloté dès les toutes premières interactions Ni-Si lors du dépôt de nickel sur le substrat de silicium avant la phase d'activation thermique formant le siliciure final. Dans cette thèse, une stratégie de modélisation à plusieurs niveaux associant des calculs ab initio, des simulations de dynamique moléculaire et des méthodes d'apprentissage automatique est utilisée pour décrire quelques étapes clés du procédé de siliciuration. L'étape de dépôt est étudiée par des méthodes ab initio. La phase d'activation est étudiée par dynamique moléculaire, pour laquelle le développement d'un potentiel interatomique de type Machine Learning a été effectué.

Dans un premier temps, les calculs ab initio sont utilisés pour élucider les premières étapes de la formation du siliciure de nickel. Notre travail démontre que lors du dépôt de nickel sur une surface de silicium, une couche alliée d'interface est formée même à température ambiante avant toute activation thermique. Cette couche interfaciale a une composition riche en nickel de type (011)Ni_3Si qui est favorisée par la capacité des atomes de nickel à pénétrer les couches en surface du substrat de silicium. Ces calculs sont validés par des mesures expérimentales de réflectivité des rayons X et de microscopie électronique à transmission à balayage à haute résolution. Ensuite, les interfaces nickel-silicium/silicium susceptibles d'apparaître après la phase d'activation thermique du procédé de siliciuration sont étudiées à l'aide de calculs ab initio. Les propriétés structurales et les charges sont analysées. Notre travail met en évidence la présence de dislocations et de transferts de charge comme mécanismes de stabilisation en relation avec l'orientation et l'empilement. En particulier, nous constatons que les tentatives de rotation du siliciure pour minimiser les énergies élastiques produites par les désaccords de maille des deux matériaux sont liées à de grandes dislocations dans les régions d'interface. Ces interfaces sont ensuite utilisées pour la construction d'une base de données ab initio pour construire un potentiel interatomique. Enfin, l'étape d'activation thermique est étudiée. Nous dévrivons le développement d'un potentiel interatomique de type Machine Learning fondé sur des méthodes de régression linéaire (Lassolars). A l'aide de ce potentiel, les dynamiques atomiques sont simulées aux interfaces nickel-siliciure/silicium pendant des temps de simulation Lassolars machine-learning en utilisant la dynamique moléculaire en utilisant différents bilans thermiques. Des analyses structurales et chimiques des structures de siliciure formées au cours de la simulation sont fournies.

Nickel silicidation process: Modelling of nickel deposition and diffusion from silicide/silicon interfaces through ab initio calculations and machine learning approach

Although nickel-based silicide thin films are already used in many technological applications in microelectronics, their formation mechanisms are still far from being understood and controlled, which makes their industrial integration difficult. It has been shown that the silicidation process is controlled from the very first Ni-Si interactions when nickel is deposited on the silicon substrate, before the thermal activation phase that forms the final silicide. In this thesis, a multi-level modelling strategy combining ab initio calculations, molecular dynamics simulations and machine learning methods is used to describe some key stages of the silicidication process. The deposition stage is studied using ab initio methods. The activation phase is studied using molecular dynamics, for which a Machine Learning interatomic potential has been developed.

First, first-principles calculations are used to unravel the early stages of nickel silicide formation. Our work demonstrates that during the deposition of nickel on top of a silicon surface, an interface alloyed layer is formed even at room temperature before any thermal activation. Moreover, we have succeeded in determining that this interfacial layer has a nickel-rich composition (011)Ni_3Si which is favored by the ability of nickel atoms to penetrate the surface layers of the silicon substrate. These calculations are validated by experimental measurements of X-ray reflectivity and high resolution scanning transmission electron microscopy.

Then, the nickel-silicon/silicon interfaces likely to appear after the thermal activation phase of the silicidation process are studied using ab initio calculations. The structural properties and the charges are analyzed. Our work evidences the presence of dislocations and charge transfers as stabilization mechanisms in relation to orientation and stacking. In particular, we find that attempts of silicide rotation to minimize the elastic energies produced by the lattice mismatches of the two materials are related to large dislocations in the interface regions. These interfaces are then used for the construction of an ab initio database to build an interatomic potential for the long time simulation of interface dynamics.

Finally, the nickel silicidation process after thermal activation is studied thanks to the development of an interatomic interaction potential of Machine Learning type based on linear regression methods (Lassolars). Using this potential, atomic dynamics are simulated on nickel-silicide/silicon interfaces during long simulation times using molecular dynamics with different thermal budgets. Structural and chemical analyses of the silicide structures formed during the simulation are provided.

Acknowledgements

This thesis represents the end of a process in which many people have been part. I want to say to these people that thanks to you I have felt deeply accompanied and supported. This is why I want to give you my sincere thanks to:

To my mother, for her infinite support and dedication,

To my father, for teaching me that we should always do right.

To my beloved Jessica, who has become my life partner.

To my colleagues and friends, who made my PhD very confortable.

To my tutors Anne Hémeryck and Julien Lam, for guiding me through this process.

Chapter 1

Introduction

1.1 The importance of miniaturization in the Microelectronics industry

Microelectronics plays an essential role in the information and communication technology industry, and has already contributed to worldwide breakthroughs in human innovation, notably to improve everyday life. For over seven decades, the microelectronics industry has distinguished itself by constantly improving the performance of its products. Still today, going further in this direction has become a necessity with the emergence of new concepts such as the cloud and instant data, which require abundant computing and memory resources [1]. The past and present success of microelectronics stems mainly from its efforts to reduce the size of components included in integrated circuits and to think up new architectures.

Since their first apparition, transistors have been used in microprocessors, which constitute the building blocks of the computing and telecommunications technologies. Silicon is an indispensable semiconductor material, present in most of the transistors since their first design. Most of these transistors belong to the so-called MOSFET family of transistors, which are field effect transistors (FET) based on the Metal Oxide Semiconductor (MOS) technology [2]. The MOSFET transistors, shown in Figure 1, operate by allowing the current to flow when the gate provides enough charge. This current flows through the channel from the source to drain parts of the device, while an electric field controls the current in the channel.

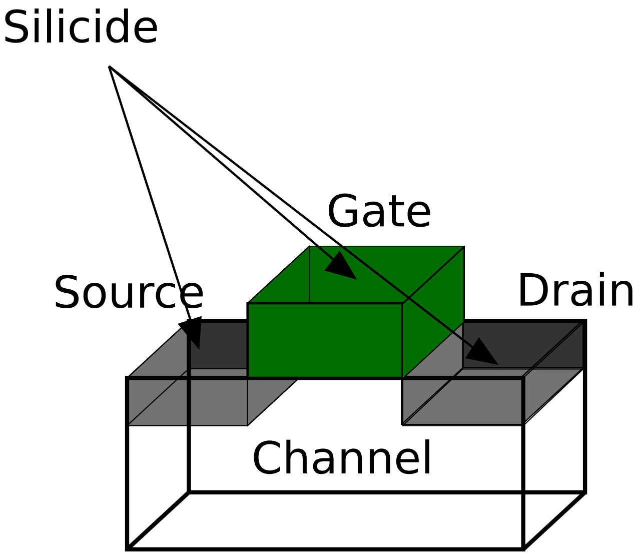

Figure 1: Representation of a MOSFET device.

The aim of reducing transistor size is to increase the number of these components in integrated circuits, and therefore, their power performance. With regard to the number of these components in integrated circuits, the Moore's law [3], which is based on observations and projections of historical trends, predicts that the number of transistors in an integrated circuit doubles about every two years. Moore's Law has now reached its limits (i.e. downscaling planar devices and reducing energy consumption), and new strategies (More Moore, More than Moore) are already being developed. According to the International Roadmap for Devices and Systems, the challenges for the next generation of integrated circuits (2025-2033) are focused on the 3D very large scale integration. It is predicted that after 2027 there is no room for 2D geometries [1].

In this context, it becomes crucial to go further in the scaling down of devices, particularly transistors. However, device downscaling still has many limitations, and Moore's scaling is increasingly challenged. The choice of appropriate materials for transistor manufacture is therefore crucial. It is also necessary to control each stage of the manufacturing process in order to cope with new difficulties such as the use of low process temperatures, contamination problems and control of interface layers [2]. As far as interface layers are concerned, they have become omnipresent with the new 3D complex architectures and predominant in terms of the dimension of the integrated layers reached. It is all about mastering them.

In this thesis and in the context to search for new material with improved performances, we focus on the problem of how to better integrate metal contacts in devices. The new promising technological strategy is the silicidation process, which allows direct integration of the material and direct formation of the metal contact from a silicon substrate, forming a so-called silicide.

1.2 Silicides

1.2.1 Definition and applications

Thanks to their excellent physical properties, silicides are a potential material for downscaling devices.

The synthesis of metal silicides in the form of ultra-thin films remains a major challenge in complementary metal-oxide semiconductor (CMOS) technology [2]. Silicides are formed by the direct reaction of a metal on a silicon substrate, forming a metal alloy: the silicides are alloys formed by the reaction of the metal with the silicon substrate during thermal annealing in a process that involves solid phase transition. This direct integration process offers a number of technological improvements: metal silicides reduce contact resistances in the active areas of transistors, and ensure electrical continuity between transistors and interconnections. This direct integration also means that silicon, and therefore silicides, can be kept small.

Silicides are of interest in many applications, including contact formation and interconnections in microelectronics. In the so-called advanced CMOS technology, the metal silicide is used to make contact with the gate, source and drain of the transistor (See Fig 1). Along with the transistor application, these silicides are widely used in the microelectronics industry in all types of technology, such as imaging, flash, photonics [2, 4, 5] ... Different silicides have been used depending on the technological application and on the dimension of the transistor gate, thus the study on the growth of thin films by silicidation process is crucial to improve the scaling down of devices with the use of low and/or short time thermal budgets.

1.2.2 Silicides of interest according to technological nodes

Silicide contacts have evolved significantly over the past three or four decades [2, 6]. The evolution has been such that the current criteria for building a successful device connection have little in common with what was only a few years ago: starting with Al and subsequently transitioning to Ti, Co and Ni silicides; and more recently, back to Ti. Initially, titanium silicide was widely used in nano- and microelectronics as ohmic contacts and interconnect materials. Indeed, titanium was the first metal widely used in industry to form a silicide, and the $TiSi_2$ compound was typically exploited up to the 0.25 micron technology [6]. However, early, the $TiSi_2$ contacts suffered problems of phase transformation when scaling down was tried, forming high resistivity phases instead of the desired low resistivity phase. These problems related to the phase transformation in titanium silicide prompted a switch to cobalt silicides. The cobalt silicide $CoSi_2$ was used in 130 nm CMOS technology due to its low sheet resistance and high stability [7]. However, the $CoSi_2$ process was found to be much more sensitive to oxygen. Here, the cleaning of the contact areas before metal deposition became crucial, and the process also required a capping layer for the Co film. In addition, other main factors that limited its use in new thinner devices were the increase of its resistance when going to very narrow sheets and its high silicon consumption. As such, in devices with nodes below 65 nm, the Ni-based silicides became widely used in replacement of $TiSi_2$ and $CoSi_2$ [4]. However, as we will see in the next sections, a rigorous understanding of the nickel silicidation process is required for its technological integration.

Phase	Resistivity ($\mu\Omega$ cm)	Temperature process °C
$TiSi_2$	$\sim$ 15-60 [8]	$\sim$ 600-800 [8]
$CoSi_2$	$\sim$18 [9]	$\sim$600 [9]
NiSi	$\sim$10-20[4]	$\sim$300 [9]

Table 1: Resistivity of titanium, cobalt, and nickel silicides.

1.2.3 The outstanding properties of NiSi silicide

The synthesis of nickel silicides instead of other metal silicides is far more efficient and cost-effective due to low Si consumption, low reaction temperature, and low resistivity (10.5–18 $\mu\Omega$cm) [4]. In addition, the formation of NiSi leads to a much smoother surface and interface. Due to these specific properties, NiSi silicide was considered in applications in the field of solar cells and transistors. In the last decade, an increasing interest took place in using polymeric materials as substrates for many Si-based electronic applications, such as poly-Si Thin Film Transistors (TFT) [10] employed for two-dimensional imaging sensors and liquid crystal displays. Schottky Barrier (SB) type TFTs were also proposed [11], with the idea of replacing the impurity-doped source-drain contacts with a metallic junction (e.g., Ni-silicides).

Ni silicidation is a diffusion controlled process, where the growth fronts of the new phases are planar and move uniformly following the standard relation where the thickness is proportional to the square root of time. Another early advantage found was that as Ni is the mostly diffusing species [12], the formation of silicides generates a new interface below the original Si interface, which renders the process much less sensitive to interfacial cleaning and the presence of oxygen. The second advantage of Ni diffusion is that vacancies generated by the diffusion itself are mainly located in the metal layer instead of in the Si layer as is the case when silicon diffuses, thus avoiding the problems that could be generated by vacancies present in the silicon substrate [13].

Ni silicide is therefore of major interest today, and to maintain this interest it is necessary to better control its formation [2].

1.3 Nickel silicides: achieving NiSi silicide

1.3.1 Phase diagram

The first complete phase diagram of Nickel silicide was published by Guertler and Tammann in 1906 [14]. After its revision by Massalski, this phase diagram is shown in Fig. 2. Later, numerical simulations including ab initio energetic calculations managed to retrieve the experimental phase diagram [15]. All these studies show that the Ni-Si system exhibits a complex structural landscape with 14 different phases of Ni-Si which are all metallic, such as the shown in Fig 2. Among them, the most preponderant are the Ni_3Si, Ni_2Si, NiSi and $NiSi_2$ phases.

Indeed, in cases of nickel silicide formation, during deposition, Ni_xSi_y alloys and their polymorphs form rapidly, changing from one phase to another of the phase diagram at temperatures right below 500 °C. The formation of the silicide

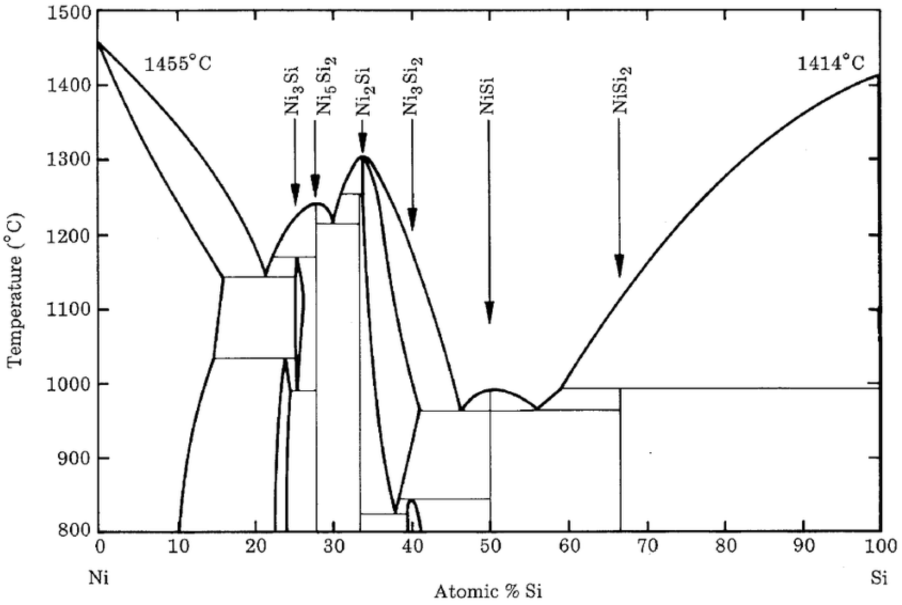

Figure 2: Ni–Si phase diagram from Massalski [16].

sequence can be divided into three stages based on the phase diagram: Ni-rich, NiSi and $NiSi_2$ phases. In this range of temperature, it is thus possible to form silicon-rich layers, which are then undesirable because of their lower conductivity of less interest for their integration in the devices.

1.3.2 Elaboration processes

One of the most widely studied methods for producing nickel silicides is thermal annealing [17]. It has been observed that during the thermal annealing process in a vacuum, the production of the NiSi phase begins. Many factors such as environment, temperature, dopant, and annealing duration must be adjusted during the thermal annealing process to achieve the desired phase. The annealing time and temperature can be chosen depending on the thickness of the nickel layer. For microelectronics applications, the effects of nickel thickness, annealing procedure, and substrate doping have been thoroughly described using the Physical Vapor Deposition (PVD) method [18]. The uniformity of silicide resistance is improved by furnace annealing during the first anneal. The uniformity of sheet resistance is also improved by increasing the temperature of the initial anneal. Second anneal temperature promotes the development of the $NiSi_2$ phase. NiSi has been synthesized using this two-step method [19]. In this approach, the first step forms the Ni_2Si phase, followed by an annealing procedure to synthesize NiSi in the second step.

Alternatively, in ion irradiation method [20], the ion beam leads to significant atomic rearrangements inside a material including atomic bond breakage, intermixing of atoms and alloying at interface regions, and material degradation. In the case of nickel silicidation, different silicide phases may be observed when an ion beam of a particular energy and fluence penetrates the Ni/Si interface [20]. During the ion bombardment, the NiSi develops at first and then increases as the ion doses rise. Cleanness of the interface is also one of the essential requirements for the utilization of NiSi in microelectronics. Even in the presence of purposefully added interfacial impurity layers, ion irradiation aids in the development of homogeneous Ni silicide layers. A disadvantage of using ion irradiation is the availability of irradiation facilities and the involved cost.

1.3.3 Progress in the understanding of NiSi formation

On the early research of silicides, the focus was on their formation and basic properties (phase diagram, conductivity, corrosion resistance, chemical stability, etc.). The thermodynamic behaviors of silicides were measured in the 20th century, and the stability of the bulk phases as a function of parameters like temperature, pressure, and composition were well known. The silicide/silicon hetero-structures were first realized by Solid State Reaction (SSR) of a metallic layer on silicon [21].

Then, the need to push forward as far as possible the scaling down of devices was accompanied by new experimental techniques [2]. The kinetic conditions in these new techniques to manipulate materials nullified the bulk thermodynamics prerequisites (namely, infinite volume and infinite time), thus allowing the occurrence of systems and phases (i.e., different micro-structural arrangements) away from the constraints reported in the available phase diagrams. In a bulk system reacting by SSR, different phases coexist in equilibrium conditions, while in thin films only one stable phase at a given time is usually observed at relatively high temperatures. The layer composition depends on the supply of metal atoms (that is limited in thin layers) with respect to the silicon availability, and also on the reaction temperature. Because of this intricate relationship, further studies of silicide formation processes were necessary in this regime of interfaces. This Ni-Si reaction couple took the interest of the material scientists since a rich variety of reaction pathways could be exploited to fabricate structures with tailored and/or innovative properties, with applications especially in micro-electronics [4].

Two decades ago the nickel silicide took on new importance for advanced technologies beyond the 65 nm technology node. Then, the need to push below the 28 nm technology in the last decade aggravated the importance of detailed materials control.

Large efforts were devoted to the comprehension of the phenomena involved during the early stages of reaction [4], prospecting to gain capability in the control of the structure of the reaction products. A perfect control of the silicide layer formation is sought to achieve the desired composition and structure of the target phase NiSi to preserve the expected outstanding properties [22, 23].

From a technological point of view and experimental characterizations

The first main observation from marker experiments in the understanding of NiSi formation it is that in the formation of metal-rich silicides (which are to be likely formed first by thermal annealing procedures), the dominant diffusing species are mostly metal atoms. Indeed, nickel is not only the dominant diffusing specie but also a fast diffusing specie in the silicon substrate [12]. For example, when comparing for example with cobalt, the solubility of nickel in silicon is close to six orders of magnitude larger than that of cobalt at 500 °C [12]. In the nickel diffusion during the silicidation process, nickel atoms distribute deeply inside the silicon substrate with a progressive reduction of the Ni supply while entering to the silicon substrate. Here, while the nickel supply is reduced, the nickel-rich phases form first, and the formation generally follows a sequence that can be divided into three stages based on the phase diagram: Ni-rich (such as Ni_3Si and Ni_2Si), NiSi and $NiSi_2$ phases. Being the silicon-rich layers undesirable because of their lower conductivity. In particular, in ref [24] it was demonstrated that a mixed layer with a Ni:Si concentration ratio of 3:1 (i.e. Ni_3Si chemical composition) was found to be formed by nickel deposition at only 70 °C. This mixed layer was found to have 6 nm of thickness and to be amorphous. This study gives account of the early Ni-Si interactions in a study that used a low temperature.

The study of these early interactions has become extremely important, in some studies it has been shown how these early stages of the Ni-Si interaction impact on the sequence of phases and on their lattice properties [25]. Nevertheless in ref [24] the Ni_3Si chemical composition was found, in-situ investigations of the Ni-Si(100) interfacial reaction during thin film deposition at 300 K present contradicting results finding either Ni_2Si [26, 27] or Ni_3Si [28] as initial mixing layer composition. Successive ex-situ investigations using Transmission Electron Microscopy (TEM) and X-ray reflectivity (XRR) measurements support the observation of such an amorphous Ni-Si mixing layer but have remained unable to provide a clear identification of the composition as either Ni_2Si or Ni_3Si [29]. In contrast, XRR results obtained for thicker Ni films clearly state the formation of Ni_2Si [30] thereby highlighting the suitability of XRR measurements for the phase analysis of such thin layers with amorphous structure. We insistently remind that the early stages of the material impact on the sequence of phases that will take place during the thermal activation phase of the silicidation process. It has been shown that the composition of the precursor layer can impact in such a way that pseudo-epitaxial orthorhombic silicides made of transrotational domains can be formed depending on the boundary conditions and on the reaction temperature [25]. These Trans-Ni silicide domains are easily recognizable by Transmission Electron Microscopy (TEM) analyses. Once the phase sequence takes place and the transition to the desired NiSi occurs, the challenge is to control its stability in order to avoid the formation of silicon-rich phases. With this goal, the silicidation process has been performed adding a few atomic percent of platinum [23].

From atomic scale modeling

On the other hand, on atomistic simulations, ab initio simulations were performed by Connetable and Thomas [31] to characterize different nickel-silicides structures. In this work emphasis was put on the phases (low and high temperatures) identified in the Ni-Si phase diagram, namely: Ni_3Si-β_1, -β_1, and -β_1, $Ni_{31}Si_{12}$-γ, Ni_2Si-δ, -θ, Ni_3Si_2-ϵ, NiSi-MnP and $NiSi_2$-α. From their results, the simulations were able to reproduce with a high accuracy measurements such as lattice parameters and formation energies of main experimental structures, except for β_2 and β_3. Also, the crystallographic nature of the γ structure was clarified. In their study, they pointed out that the comparison of experimental Raman spectra and vibrational calculations will help experimentalists to identify without ambiguity $NiSi_3$ structures.

In addition to the characterization of all these nickel-silicide structures, Connetable and Thomas studied in ref [32] the pure bulk NiSi from ab initio simulations. In this work, a range of properties were studied such as structural, electronic, vibrational, and elastic properties. From their results, the ab initio measurements such as optimized lattice parameters, formation energy, and vibrational properties were found be in agreement with experimental data. Particularly, by measuring elastic constants, the NiSi structure was shown to be highly anisotropic. Here, the linear bulk modulus along a specific axis was found to be much larger than along other axes.

In addition to bulk silicides, computational studies have addressed the electronic properties of the interface between silicon and nickel silicide [33, 34] due to the importance of nickel silicide as a contact material in CMOS devices. These studies have addressed measurements such as the Schottky barrier height. In these studies, properties such as interface energies are calculated for two structures of the $NiSi_2$/Si(111) interface, which are named as type-A and type-B. From their results they found that interface energies varied when the $NiSi_2$ layer was made thicker, concluding that the interface structure with lowest energy changes from type-A to type-B as the thickness of the $NiSi_2$ layer is increased. In ref [34], density-functional theory calculations were used to identify trends in both thermodynamic stability and magnetism of several transition-metal silicide films on Si(001) were studied. Particularly, the electronic properties of the NiSi/Si interface were addressed. It is important to point out that these interfaces are not stable indefinitely. Here, the metal atoms that are close to the interface regions are able to diffuse into the silicon substrate during the device fabrication and operation. The diffused atoms not only produce impurity states, but also the Schottky barrier change, and leakage currents in Si channels are observed [35]. In this context, the ability of the metal atom to penetrate in the silicon substrate was investigated in ref [36]. In this study, the difference in chemical potential between bulk metal and bulk Si was calculated for various metal atoms using the first-principles calculations. In this study is discussed that such differences are adequate measurements for the penetration energy of a metal atom from a metal/Si interface into a Si substrate.

As mentioned in the last section, in some cases, the silicidation process has been performed in experiments adding a few atomic percent of platinum with aims to control the fast nickel diffusion into the silicon substrate. In atomistic simulations, the formation of Ni(Pt)silicides on a Si(001) surface was investigated using ab initio molecular dynamics simulations [37]. In this study, after deposition of a nickel-overlayer alloyed with platinum, the calculations revealed fast diffusion of nickel atoms into the silicon lattice. Here, the formation of Ni_2Si silicide was initially observed. At the same time, silicon atoms were also found to diffuse into the silicide substrate, observing that the transformation of Ni_2Si into NiSi is likely to proceed via a vacancy-assisted diffusion mechanism.

On the other hand, the silicidation process was also studied with the help of a neural network potential [38]. In this study the transition from the Ni/Si interface to the Ni_3Si/Si interface was observed by performing assisted molecular dynamic simulations. However, their study was focused into study an uncertainty estimator and in to prove that their approach could spatially and temporally trace simulation errors with atomic resolution.

Besides of the progress that has been made in the understanding of the silicidation process, the knowledge in this subject is far from being complete. Moreover, not only the NiSi silicide formation is not completely understood but also its stability must be also studied. Here, besides its outstanding properties, the sheet resistance of NiSi increases with annealing temperature due to the phase transition from NiSi to $NiSi_2$. In this context, the stability of nickel silicides is discussed in the next section.

1.3.4 The stability problem of NiSi

Besides the outstanding properties of NiSi, its integration in microelectronic applications remains a challenge due to its poor thermal stability, which leads to an increase of the electrical resistivity. Indeed, two types of thermal degradation have been observed.

On the one hand, since NiSi is not the phase in thermal equilibrium in contact with Si, it is expected that the $NiSi_2$ phase emerges upon heating. In the meantime, this alternate phase exhibits three disadvantages for microelectronic applications: (1) it is two times more resistive than NiSi and (2) it consumes twice as much Si, (3) it is much rougher as it forms through a nucleation controlled reaction. In the past years, a fair amount of work was published on stabilizing the NiSi while preventing from any transformation to $NiSi_2$ [39, 40]. As a general purpose, the synthetic conditions stabilizing the NiSi phase need to be expanded and several methods have been proposed such as ion implantation [41], interlayers [42], or protecting caps [43, 44], or adding a small amount of other atomic species to nickel. Among the specified methods, the addition of either Pd and Pt was shown to push the formation of $NiSi_2$ to the highest temperatures [23].

On the other hand, the NiSi film can also degrade at high temperatures through the formation of undesirable silicide grains. The structure of NiSi shows surprisingly a very large anisotropy in thermal expansion along the different axis directions. This high anisotropy is an important factor at higher temperatures when grains can be formed easily. Although this morphological instability was not expected to be dominant at first because the early studies were performed with thicker Ni films, for thinner films relevant to the current microelectronic devices, the formation of undesirable grains becomes the main degradation mechanism at high temperatures [22].

Among the different possible doping elements that can be used to improve the NiSi stability, Pt seems to effectively reduce the formation of undesirable grains, while it is also useful to prevent the $NiSi_2$ formation. Indeed, in ref [45] it was demonstrated that the presence of Pt increases the phase transition temperature from NiSi to $NiSi_2$ by roughly 100 °C. Unfortunately, it was also demonstrated that the sheet resistance increased approximately in 10 % due to the presence of platinum, limiting the amount of platinum that can be used. Cojocaru-Miredin et al. [46] studied the redistribution of platinum after heat treatment at 290 °C for 1 h. Here, two silicides Ni_2Si and NiSi were found. It is important to point out that, besides of the benefits of adding platinum, the presence of additional elements (such as platinum) in the nickel-silicidation process complicates the understanding of the process. Here, it is required to also consider the presence of these additional elements in the identification of the nickel-silicide phases, and the possibility of the formation of additional phases which are, of course, not present in the Ni-Si phase diagram. Indeed, it is necessary to consider that both the Ni-Si and the Pt-Si phase diagrams are rich in phases, and platinum silicides do not generally have the same crystal structure as nickel silicides [47].

As an alternative to the addition of doping elements to improve the NiSi stability, the growing conditions in the silicide formation can also be adjusted to obtain a better stabilization of the NiSi phase. In particular, rapid thermal annealing (RTA) on Si (111) substrates can be used [19]. This technique consists in a two-step process: in the first step, Ni_2Si is made by annealing at low temperature, followed by an annealing at 500 °C to make NiSi.

1.4 Strategy and goals of the present work

1.4.1 Objectives of the work

Today, a perfect control of the silicide layer formation is sought to achieve materials with outstanding properties [22, 23]: the key step is to control the formation up to the NiSi silicide, avoiding the formation of $NiSi_2$. Mastering the growth of NiSi directly integrated from a silicon substrate remains a major challenge. The complete reaction pathways involved in NiSi formation are still debated [2, 48, 49] thus making the industrial integration of Ni-based silicides difficult. It requires an understanding of each of the steps before and after thermal activation, and the associated phase transformation throughout the entire silicidation process. The modeling of the whole silicide process, including the deposition and annealing steps, has not yet been achieved.

The aim of this work is to contribute to the fundamental understanding of the formation of nickel silicides as close as possible to the technological deposition process used, using atomic-scale modeling and simulation tools. The silicidation process takes place in two stages, i.e. deposition of the metallic element on the substrate and thermal activation at controlled temperature to form the final silicide.

- The first objective of this work will therefore be to simulate the two stages of the silicidation process from a modeling strategy point of view.
- The second objective is to describe the state of the material after deposition, which will influence the second step of thermal activation to the final silicide. In particular, it has been shown how the early stages of the Ni-Si interaction impact on the sequence of phases and on their lattice properties. Silicidation is indeed driven by what occurs since the first Ni-Si interaction during the nickel deposition step.
- The third objective will be to study the dynamics of the interface from an as-deposited state of the material towards the diffusion deeper in the material.

1.4.2 A multilevel modeling strategy to get insight in the nickel silicide growth

To achieve the objectives described above, we cannot be satisfied with a single modeling tool and a single scale of description. In this thesis, a multi-level modeling strategy involving first-principles calculations, molecular dynamics simulations and machine learning methods is used to describe some key steps in the silicidation process.

Chapter 2 will describe the strategy employed in this thesis.

In Chapter 3, first-principles calculations are used to understand the first steps in the formation of nickel silicide. The aim is to demonstrate the formation of an interface alloy layer during the deposition of nickel on a silicon surface. These calculations are validated by experimental measurements of X-ray reflectivity and high-resolution transmission electron microscopy.

Then, in Chapter 4, the nickel-silicon/silicon interfaces likely to appear after the thermal activation phase of the silicidation process are studied using ab initio calculations. The first aim is to build a database containing interfaces for the development of a Machine Learning-type interatomic potential, which will be described in Chapter 5 and used to simulate interface dynamics using molecular dynamics. The construction of this database of interfaces, although not exhaustive, enables structural and charge analysis for some of them.

Finally, the silicidation process of nickel after thermal activation is studied through the development of a Machine Learning interatomic interaction potential based on linear regression methods (Lassolars). In Chapter 5, we therefore discuss the database used to build this Machine Learning potential and how this potential is constructed. Using this potential, atomic dynamics are simulated on nickel-silicon/silicon interfaces over long simulation times using molecular dynamics with different heat balances.

Chapter 2

A multi-level modeling strategy for studying the nickel silicidation process

2.1 Why use a multi-level modeling approach?

2.1.1 General overview

As seen in the previous chapter, the silicidation process consists of mainly two steps; deposition and annealing (Please see Figure 3). As shown in the left part of Figure 3, in the deposition of nickel atoms on the silicon surface, the nickel adsorption, diffusion on the silicon surface, and insertion into the silicon substrate are produced until the formation of an as-deposited interface alloy (shown in the middle part of the figure). Subsequently, a budget of temperature (typically lower than 700 K) is applied to produce the phase transformation from the as-deposited material to the final desired silicide (NiSi) (shown in the right part of the figure).

Ideally, atomistic simulations should help to understand the silicidation process and it would be insightful to perform large-scale simulations of hundreds of atoms in the nanosecond regime. In particular, by initializing a simulation with an interface made of nickel-rich silicide and silicon, one could observe how thermal activation can lead to the formation of each of the other silicide stoichiometries. However, such large-scale simulations can hardly be obtained with

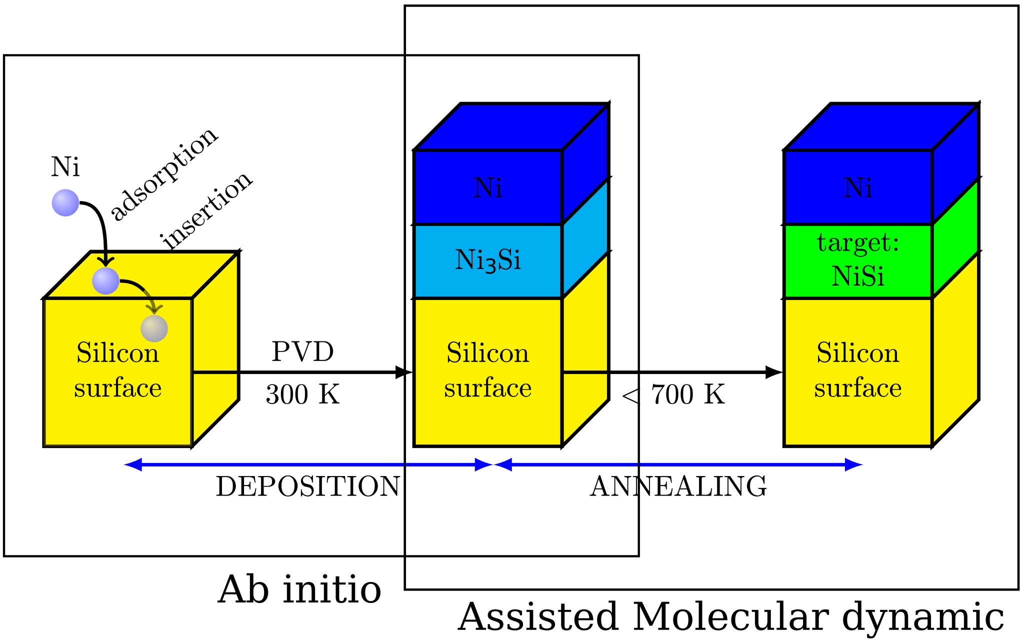

Figure 3: Multilevel modelling strategy used for the understanding of an optimized NiSi silicide formation. A schematic representation of the two main stages needed to obtain NiSi silicide is shown: In the deposition step, Ni atoms are deposited with Physical Vapor Deposition (PVD) at ambient temperature forming an as-deposited silicide interface, which is then thermalized in the annealing step by using temperatures below 700 K to form the targeted NiSi layer. In the strategy, ab initio calculations are used for the study of the deposition step and for the creation of an accurate machine learning database, which is then used in the development of a machine learning potential. The annealing step is performed through assisted molecular dynamic simulations.

the current state-of-the-art in terms of computational tools. The high computational cost of the quantum accurate models including DFT [50] prevents from performing large-scale simulations and can only simulate systems containing a few hundred atoms. In this context, the tool of choice would be molecular dynamics (MD) [51] which uses empirical interatomic potentials to describe the interaction between atoms and allows the simulation of a large number of atoms with bearable calculation costs. However, today there is no empirical potential that matches our needs. Machine-learning interaction potentials (MLIP) have been proposed in recent years to bridge the gap between the quantum accurate models and classical potentials [52, 53]. The success of these methods can be seen in the large variety of materials that they managed to model including pure metals [54], organic molecules [55], water [56], amorphous materials [57], and hybrid perovskites [58]... In general, MLIP relies on a set of DFT calculations from which a database is constructed using forces and energies of given structures and on a machine-learning engine to construct the interaction potential.

2.1.2 Our approach

Thus in this work, we use **ab initio calculations** with a double objective:

- to describe the first steps of the silicidation process to get a realistic picture of the as-deposited material before the thermal activation.
- to develop a new interatomic potential based on Machine Learning approaches from the ab initio database thus constructed.

To begin, we focus on obtaining a precise atomic scale characterization of the interface alloy formed during the deposition of Ni on a Si(100) substrate, before thermal activation (left part of Figure 3) using **density functional theory calculations** (DFT). We carry out a comprehensive theoretical study, based on detailed considerations of first principles of possible pathways for Ni adsorption, diffusion, and insertion into the surface layers of the Si substrate until the formation of a nucleus interface alloy. Then, we use the **activation-relaxation technique** (ART) [59] coupled with DFT Quantum Espresso software [60, 61] to find the transition state located between two different minimized structures. Meanwhile, in the scope of the second objective, which is the construction of an ab initio database for the **development of an interatomic machine learning potential**, we also study silicide/silicon interfaces using DFT calculations in order to further understand silicidation process by comparing the stability of some of the relevant interfaces and their stabilization mechanisms. Finally, all of the considered DFT calculations are included in a database made of structures and the associated forces that is employed for the development of a machine-learning interaction potential. In particular, we use the **Physical LassoLars Interaction Potential** (PLIP) model [62], which is a linear model whose theoretical basis will be described in this chapter. After validating the potential's accuracy, we perform large-scale **MD simulations** of thermal activation in a silicide/Si(100) interface to study dynamics of atoms.

In the following, we describe each of the methods used in this thesis.

2.2 Ab initio methods

2.2.1 The density functional theory (DFT)

The density functional theory (DFT) has been widely used for the calculation of the electronic structure of materials in all kinds of areas of physics and chemistry [63, 64]. This theory is part of the so-called ab initio or first-principles techniques, and allows for the calculation of electronic properties of a system based on the Schrödinger equation. However, although DFT is based on the Schrödinger equation, the complexity of the Schrödinger equation when applied to a many-body system makes its practical usage too computationally demanding. The Schrödinger equation thus has to be adapted to be implemented into efficient numerical algorithms. The approximations and concepts employed in this adaptation are the constituents of the DFT theory. In the following, the main concepts explaining the density functional theory are described.

The problem of the matter structure

Schrödinger equation, published in 1926, was soon applied to atoms, molecules and solids. Here, we can unambiguously describe all the systems as a set of electrons and nuclei interacting through the forces of Coulomb. In these systems, the Hamiltonian is written as follows:

$$\begin{aligned}\hat{H} = &-\sum_{I=1}^{M}\frac{\hbar^2}{2M_I}\nabla_I^2 - \sum_{i=1}^{N}\frac{\hbar^2}{2m}\nabla_i^2 + \frac{e^2}{2}\sum_{I=1}^{M}\sum_{J\neq I}^{M}\frac{Z_I Z_J}{\parallel \mathbf{R_I} - \mathbf{R_J} \parallel} \\ &+ \frac{e^2}{2}\sum_{i=1}^{N}\sum_{j\neq i}^{N}\frac{1}{\parallel \mathbf{r_i} - \mathbf{r_j} \parallel} - \sum_{I=1}^{M}\sum_{i=1}^{N}\frac{e^2 Z_I}{\parallel \mathbf{R_I} - \mathbf{r_i} \parallel}\end{aligned} \tag{2.1}$$

where **R** and **r** are the nuclear and electronic coordinates respectively, and Z_I and M_I are the charges and masses of the nucleus. In principle, all the properties of the systems can be obtained by solving the time-independent Schrödinger equation:

$$\hat{H}\psi_n(\mathbf{R},\mathbf{r}) = \epsilon_n\psi(\mathbf{R},\mathbf{r}) \tag{2.2}$$

where ϵ_n are the energy eigenvalues and $\psi_n(\mathbf{R},\mathbf{r})$ are the wave-functions. However, this method is very difficult to implement in practice. As such, analytic or numerical exact solutions exist only in few cases. The main difficulty is that the system is made of many bodies and the Schrödinger equation becomes inseparable. Therefore, the usual choice is to resort to a few well-controlled approaches to address the problem of non-separability. In this context, the Born-Oppenheimer Approximation is used. This approximation states that nuclear masses being much larger than electron mass, the atomic nucleus can be treated as a classical particle with electrons responding immediately to any nuclei movements. The dynamics of electrons and nuclei can thus be decoupled.

The Kohn-Sham equations

To solve this problem of the non-separability of the wave-functions, Kohn and Sham proposed a theory that simplified drastically the picture. Kohn and Sham's idea (1965) [65] started with the observation that a system of non-interacting electrons is exactly described by an anti-symmetric wave-function constructed using Slater determinants of electron orbitals. Kohn and Sham stated that if one can find a system of electrons non-interacting particles that produce the same electron density as a system of interacting electrons, then the system of N non-interacting particles can thus be decomposed into single-electron Hamiltonians $\hat{h}_i$, whose sum constitutes the total Hamiltonian for the non-interacting system $\hat{H}_{NI}$:

$$\hat{H}_{NI} = \sum_{i}^{N} \hat{h}_i \tag{2.3}$$

with:

$$\hat{h}_i = -\frac{\hbar^2}{2m}\nabla_i^2 + v_R(\mathbf{r}_i) \tag{2.4}$$

where N is the number of electrons and v_R is the potential that ensures that the electron density is the same as in the interacting system. This is known as the Kohn-Sham formulation. In this case, the Hohenberg-Kohn theorem ensures that the energy in the ground state is the same as the energy of the interacting system. In this Hamiltonian, there are no electron-electron interactions, so its wave-functions can be written as Slater determinants.

$$\psi = \frac{1}{\sqrt{N_s!}} SD[\phi_1(1), ..., \phi_N(N)] \tag{2.5}$$

where ϕ_1 are the electron wavefunctions and N$_s$ is the number of doubly occupied orbitals, that is, there is no spin dependence. Thus, the electron density can be written as:

$$\rho(\mathbf{r}) = 2\sum_{i=1}^{N_s} |\phi_i(\mathbf{r})|^2 \tag{2.6}$$

where the Kohn-Sham orbitals are the result of a mathematical construction and, in principle, they do not have a trivial meaning except for allowing the construction of the electronic density. The Kohn-Sham orbitals satisfy the Kohn-Sham equation, however, the reference potential is not known v_R. What is known about v$_R$ is that is a potential that ensures that the electron density of the non-interacting system is the same as that of the interacting system. Therefore, it is possible to find the density of the interacting system minimizing the Kohn-Sham functional with respect to density, under the restriction that the density integrates the number of particles.

The variational principle is as follows:

$$\left(-\frac{1}{2}\nabla_i^2 + v_R(\rho, \mathbf{r})\right)\phi_i(\mathbf{r}) = e_{KS}\phi_i(\mathbf{r}) \tag{2.7}$$

where e$_{KS}$ is the Kohn-Sham energy and v_R the so-called Kohn-Sham potential. As the Kohn-Sham potential depends on the density, the equation must be solved self-consistently by the following procedure:

1. An initial guess is made for the electronic density.
2. Kohn-Sham potentials are calculated.
3. Kohn-Sham equations are solved.
4. The electronic density is updated.
5. Come back to step 2 considering the new electronic density.

This procedure is performed iteratively until the electronic density is found to be converged, which indicates that the ground state of the system has been found. To extend the method to spin-polarized systems it is enough to consider the total electron density as the sum of two independent spin densities.

Approximations to exchange and correlation terms

To solve the Kohn-Sham equations, a good strategy is to separate the energy into different pieces of decreasing importance from the energetic point of view. By following this idea the energy of the system can be expressed as:

$$E[\rho] = T_{ni}[\rho] + V_{ne}[\rho] + E_H[\rho] + E_{xc}[\rho] \tag{2.8}$$

where T_{ni} is the kinetic energy in the non-interacting system, V_{ne} is an external potential, E$_H$ is named the Hartree energy, and E$_{xc}$ the so-called exchange-correlation energy. Here, the Hartree energy corresponds to the classical density-density interaction energy and the kinetic energy must be written as a function of the electronic density. Here, all the ignorance of the system is displaced to the exchange-correlation energy.

Many approximations to the exchange-correlation term exist to reproduce accurately the desired properties of a studied system. Between them, one computationally efficient is the Generalized Gradient Approximation (GGA). In this approximation, a semi-local inhomogeneity of the electronic density is introduced by expanding the exchange-correlation term as a series that depends on the density and its gradients.

$$E_{xc}^{GGA} = \int \rho(\mathbf{r})\epsilon_{xc}(\rho, \nabla\rho, \nabla^2\rho)d\mathbf{r} \tag{2.9}$$

The GGA approximations have been carried out using different methods. One of them is to write a theoretical expression and then fit its coefficients in such a way that they reproduce some exact limits. The way to perform this is not unique as it is not possible to force all behaviors at the same time. In 1996, Perdew, Burke, and Ernzerhof proposed an exchange-correlation functional that satisfies many formal properties and limits [66], sacrificing only some properties that are less important from the energetic point of view. This approximation has been called PBE and is widely used in solid-state physics.

Computational details

In this thesis, DFT calculations are performed Quantum Expresso (QE) [61]. The PBE generalized gradient approximation of the exchange and correlation functional is used altogether with Projected Augmented Waves pseudo-potentials (PAW) [67]. A plane wave basis set with an energy cutoff of 50 Ry is used to describe the wave functions. The Brillouin zone is sampled at the Gamma point only. Forces on each atom of the stable structures are all lower than 0.025 eV/Å. The magnetization of Ni disappears as soon as Ni interacts with Si, which permits not to use a spin polarization calculation.

For the deposition calculations, we compute the adsorption energy E_{ads} of the N-th Ni atom using:

$$E_{ads} = E_{N\times Ni} - E_{(N-1)\times Ni} - E_{Ni}, \tag{2.10}$$

where $E_{N \times Ni}$ is the energy of the relaxed supercell containing N adsorbed Ni atom(s), $E_{0Ni} = E_{surface}$ is the energy of the Si reconstructed surface, and E_{Ni} is the energy of an isolated Ni atom.

2.2.2 ARTn & DFT

In the last decades, there has been considerable interest in the development of methods able to sample the energy landscape of materials. Applications of those methods include chemical reactions and defect diffusion in long-time periods, which could be associated with systems composed of thousands of atoms. Most of the approaches focus on the search for transition states and the computation of energy barriers, requiring the knowledge of both the initial and final states. However, such approaches have limited application in complex systems where only a few states are known. In these situations, methods such as the activation-relaxation technique (ART nouveau) [59, 60] are preferred because they do not require knowing the final states to sample the energy landscapes (so-called open-ended methods). Sampling of the energy landscapes allows us to find the saddle points and adjacent minima near a local minimum, providing information on the possible evolution of systems. This approach has been applied with success to a range of problems from Lennard-Jones clusters to proteins and amorphous silicon [68, 69, 70]. In Figure 4, a schematic representation of an exploration of the energy landscape of a material by using the ARTn method is shown. This exploration is done for the finding of transition states and diffusion pathways. Here, ARTn method uses and proceeds in three steps:

1. Leaving the harmonic well: the initial configuration typically a minimum structure, as shown in Figure 4) is deformed locally to identify a direction of negative curvature on the energy landscape, which indicates the presence of a nearby saddle point

2. Convergence to a first-order saddle point: once a direction of negative curvature is identified, the system is pushed along this direction, while the energy of the system is minimized in the perpendicular hyperplane orthogonal to this direction until the total force is lower than a threshold value. Using this procedure the saddle point is found (saddle point represented by a black dot in Figure 4).

3. Relaxation into a new minimum: the configuration is pushed over the transition state, and the total energy is relaxed to find the new minimum.

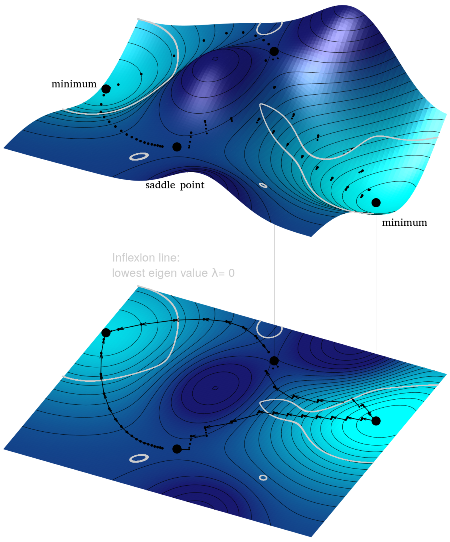

Figure 4: Schematic representation of an exploration of the energy landscape of a material for the finding of transition states and diffusion pathways by using the ARTn method. On top, three dimensional representation; energy values are plotted perpendicular to two spatial dimensional coordinates. On down, two dimensional representation; two spatial dimensional coordinates are shown and energy values are only shown by color coding, in which light blue and blue indicate low and high energy values respectively. Minimums and saddle points are indicated by black dots, while the paths followed are indicated by dotted lines. Picture from [60].

This kind of methods can also be coupled with various accept/reject schemes for the finding of energy minima in structures, as done in the kinetic version of ARTn, so-called kinetic ARTn [71, 72].

In this work, the activation-relaxation technique (ART) is used in its ART-DFT version where it is coupled with a DFT software, here QE, for the force and energy evaluations [60, 73] Two kinds of calculations are performed:

- When only the initial structure is known (exploration mode), an exploration of the potential energy surface to obtain all the saddle points and minima surrounding this initial structure
- When the initial and final structures are known, convergence to the saddle point from an interpolation of these two structures.

We used 0.05 eV/Å as threshold for force convergence when defining the transition state structure. In the exploration mode, atoms are pushed in random directions that are restricted to a cone of angle 10, when we want to guide the calculation in a given search zone.

2.3 Molecular dynamics

Molecular Dynamics (MD) [51] is a computational method to simulate the movements of atoms in a many-body system under different external conditions such as temperature, pressure and applied forces. These simulations are essential in chemistry, physics, biology, engineering and other fields. This method originated with simulations of interacting hard spheres and the extraction of thermodynamic data from the simulation. Today, molecular dynamics is one of the most flexible and popular tools available for exploring molecular structure, thermodynamic properties and dynamics. Molecular dynamics is a classical model in the sense that Newton's equations are used to solve the evolution of the system. Here, Newton's equations are solved sequentially in time by discrete timesteps. Crucial for MD simulations is the way to compute forces between the atoms. One possibility is to use the DFT framework in so called ab initio MD simulations. Alternatively, different classical formulations were developed to mimic interatomic interactions and avoid the explicit modelling of electrons. The development of such models includes the choice a functional form and the fitting of the associated parameters which is usually done for a given material to match with experimental data or data obtained from DFT modeling. The simplest model for a molecular interaction potential is the hard-sphere model, which was the first model treated in molecular dynamic simulations. In that model, atoms are not interacting with each other except for small distances where the interactions is infinite. Then, other traditional interaction potentials include using Lennard-Jones, Coulomb or Morse potentials. In some cases, it may also be necessary to incorporate three-body interactions with explicit angular contributions. Finally, for metals, both the Embedded Atom potentials (EAM) and their modified forms (MEAM) are usually employed with success [74]. These potentials incorporate a simplified approximation of the local electron cloud density due to the presence of neighboring atoms. In comparison to ab initio MD, the use of explicit functional formulations allows for a drastic gain in computational performance. However, classical interaction potentials also suffer from lack of accuracy and can not always be used to model the most complex systems. In this thesis, molecular dynamic simulations are performed by using the open-source code Large-scale Atomic/Molecular Massively Parallel Simulator (LAMMPS) package [75].

2.4 Machine learning methods

Machine-learning interaction potentials (MLIP) aim to build a bridge between quantum models and classical interaction potentials, allowing to perform large-scale simulations with similar accuracy to those obtained with first-principle calculations. For that purpose, the total potential energy of the system is always expressed as the sum of the individual contribution of each atom as in most traditional interaction potentials. Then, the local environment of atoms is mapped into a list of descriptors, and the atomic energy is expressed as a function of this list.

The two most popular approaches are based on artificial neural network architectures and kernel similarity measurements [76, 77]. Although these approaches allow for building very accurate potentials, the considered functions are mathematically complex and made of numerous fitting parameters. As an alternative, simple functions describing a polynomial development of the descriptor space have been also proposed [78, 79]. The main advantage of these linear models is that the training process and their use are quicker when compared to the other methods. Indeed, the finding of fitting parameters is made by using simple linear regression schemes, while other MLIPs employ more complex iterative optimization protocols. In addition, the simplicity of the linear relationship allows for better interpretability of the obtained potential.

Regarding the construction of a linear model for machine-learning interaction potentials, the main problem consists in determining an appropriate basis of descriptors X and linear coefficients $\hat{w}$ with the following relationship:

$$y \sim X\hat{w}. \tag{2.11}$$

where y is the list containing all the quantum accurate measurements of all structures considered, such as total energy, forces, and/or stress tensor components. In practice, this relationship can only be an approximation and several methods exist to estimate the best vector $\hat{w}$.

The Physical LassoLars Interaction Potential (PLIP) model

In this thesis, we use the Physical LassoLars Interaction Potential (PLIP) model [62], which is a linear model that uses the LassoLars regression for the search of the fitting parameters. In this model, the descriptors are constructed to explicitly exhibit the physical nature of the interactions, by describing the atomic interactions as two-body [2B], three-body [3B], and N-body [NB]. In this model, the total energy of the system is described as follows:

$$E^{(i)} = \sum_{n} \omega_{n}^{(2B)} 2B_{n}^{(i)} + \sum_{n,p} \omega_{n,p}^{(3B)} 3B_{n,p}^{(i)} + \sum_{n,m} \omega_{n,m}^{(NB)} NB_{n,m}^{(i)} \tag{2.12}$$

where $\omega_{n,p}$ are the coefficients that need to be determined and the explicit form of the descriptors are the following:

$$2B_{n}^{(i)} = \sum_{j} f_{n}(R_{ij}) \tag{2.13}$$

$$3B_{(n,p)}^{(i)} = \sum_{j}\sum_{k} f_{n}(R_{ij}) f_{n}(R_{ik}) cos^{p}(\theta_{ijk}) \tag{2.14}$$

$$NB_{(n,m)}^{(i)} = \left[\sum_{j} f_{n}(R_{ij})\right]^{m} \tag{2.15}$$

Here, the R$_{ij}$ and R$_{ik}$ are interatomic distances with angles θ_{ijk} associated, p and m are two positive integers, and the f_n terms can be any kind of function. For example, classical functions such as Gaussian, Lorentzian, and Slater-type functions can be implemented. In this work, we use Gaussian functions at different central positions and widths. Altogether, we have a list of 154 descriptors and for each of them is ascribed one linear coefficient that needs to be fitted to match DFT results.

Among the different methods for obtaining the linear coefficients, PLIP employs the LassoLars [80] algorithm which consists in adding a penalizing constraint on top of the normal minimization scheme:

$$\hat{\mathbf{w}} = \underset{\mathbf{w} \in \mathbf{R}^{D}}{argmin} \frac{1}{2} \sum_{i=1}^{N} \left(y_{i} - \sum_{j}^{D} x_{ij} \hat{w}_{j} \right)^{2} + \alpha \sum_{i} \omega_{i} \tag{2.16}$$

where an additional constraint α on the linear weights distribution is considered. Since this equation can not be solved in closed form, several optimization strategies were developed to estimate such a constraint solution. In our case, the Least angle regression selection (Lars) method is used:

1. All the $\mathbf{w}$ values are set to 0.
2. A first descriptor is selected by measuring the dot product between $\mathbf{y}$ and the columns of $\mathbf{X}$.
3. The selected coefficient is optimized and chosen as the largest value possible until a second descriptor has a higher correlation with a residual value.
4. Coefficients of both vectors are optimized in a direction equiangular until a third vector becomes most correlated to the new residual.
5. Reiterate to Step 2.

As such, the most appropriate descriptors are sequentially selected while keeping the others with linear coefficients exactly equal to 0. This strategy allows for starting with a large number of available descriptors and reducing the complexity for the obtained potential in an agile manner.

Chapter 3

A comprehensive atomistic picture of the as-deposited Ni-Si interface before thermal silicidation process

3.1 Introduction

As mentioned in the introduction, a perfect control of the silicide layer formation is sought to achieve the desired composition and structure of the target phase NiSi. In addition, the early stages of the Ni-Si interaction impact on the sequence of phases and on their lattice properties [25, 81, 82].

The process of silicidation is primarily driven by what occurs since the very first Ni-Si interaction during the nickel deposition step. During nickel deposition onto a silicon surface, nickel atoms start to diffuse rapidly into the silicon substrate, creating an interface alloyed layer before any thermal activation [4]. The composition and thickness of this interfacial layer significantly influence the subsequent stages of the silicidation process following thermal activation, as well as the desired formation of the target phase. The study of the interface alloyed layer formed before thermal activation becomes therefore relevant to predict and control the silicidation process. Previous research has revealed that the interfacial layer formed before thermal activation exhibits a nickel-to-silicon ratio of 3:1 when the deposition phase is conducted at room temperature [4]. However, today the as-deposited state of the material before thermal activation is far from being understood and experimental and theoretical studies are scarce.

The objective of this chapter is to describe the initial steps of the nickel silicidation process prior to the thermal activation step and access what the state of the material before thermal activation to form the final silicide. This study is important for understanding the origin of the sequence of the different Ni_xSi_y phases during the silicidation process. We therefore focus on the material, as-deposited prior to thermal activation, through a precise atomic scale characterization of the alloyed interface layer formed during the deposition of nickel on a silicon substrate, as depicted as deposition phase. We present the results of the deposition of Ni atoms: this includes an analysis of adsorption, surface diffusion and insertion of Ni on the Si surface until the formation of an alloyed pattern using first principles calculations.

This DFT study, carried out step by step by gradually increasing the Ni coverage, can be divided into two parts:

- At first, we will describe the initial steps of the nickel deposition including the adsorption of Ni on the surface of the silicon substrate, the diffusion of Ni atoms on the surface, and the insertion of Ni atoms into the topmost layers of the silicon substrate. Our results will include formation energies altogether with activation barriers. The study is carried out for a single nickel atom (see section 3.2) and two interacting nickel atoms (see section 3.3).
- Then, we will describe the formation of an alloyed interface layer. This last part (section 3.4) is performed by increasing the nickel coverage. We describe thermodynamic effects that appear on the early formation of the interface alloy.

3.2 The behaviour of one Ni atom regarding a Si(100) substrate

3.2.1 One Ni atom adsorption on Si(100)

The deposition step starts with the adsorption of Ni atoms on the surface of the silicon substrate. As can be seen in Figure 5-c, the Ni atom is initially positioned on top of several distinct adsorption sites. Using the specific topology of the silicon reconstructed surface [83], we identified 8 different possible initial sites. In addition, we assume that the surrounding areas of each site produce the same results. The Figure 5 also shows the specific reconstruction of the (100)-(2x1) silicon surface, featured by dimers row and a channel. Here, the Si(100) surface is simulated using a $2\times2\times7.5$ supercell of crystalline silicon that contains fifteen layers of sixteen silicon atoms.

After structural relaxation through energy minimization, for each of the 8 initial sites, we obtained 8 different stable adsorbed configurations (See Fig. 6)

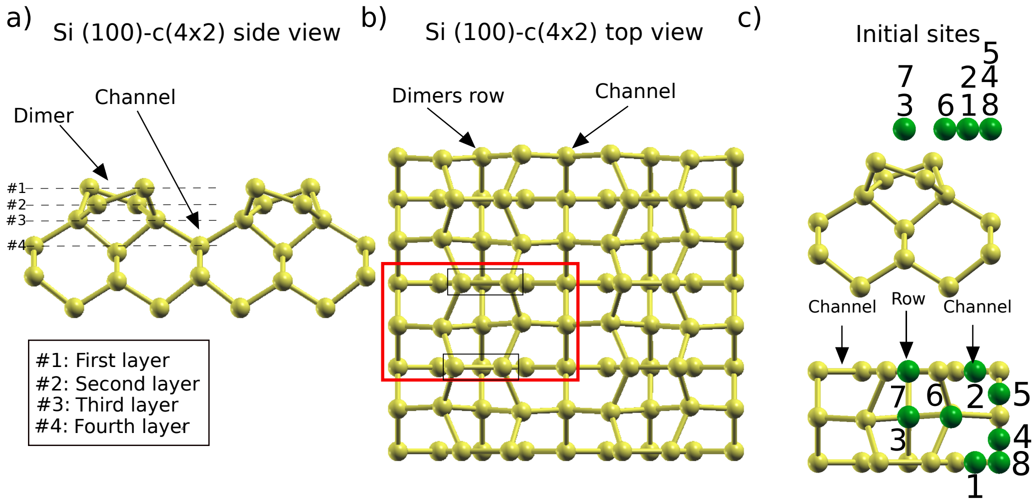

Figure 5: Deposition of Ni atoms on the surface. a) Side view of the used Si(100)-c(4x2) surface reconstruction. Arrows indicate dimers rows separated by channels, and the four topmost layers are indexed. b) Top view of the same surface. c) Side and top view of the initial positions investigated in the Ni deposition. Yellow and green spheres represent Si and Ni atoms, respectively.

that we will describe in the following. The corresponding adsorption energy for each configuration is given according to eq. 2.10 of Methods Chapter.

In this catalogue, the three starting configurations #1, #2 and #3 on Fig. 5 lead to the three most stable configurations namely a, b an c in Fig. 6. We label them respectively as *Channel-down (CH-down)*, *Channel-up (CH-up)* and *Dimerbed (DB)*.

- In CH-up and CH-down, the configurations are reached upon adsorption above the channel. In these configurations the Ni atom is located inside the channel between the third and fourth layers. Here, the Ni atom forms six bonds with the surrounding Si atoms. These configurations have adsorption energies of -4.58 and -4.34 eV.

- In DB, the Ni atom is located between two adjacent dimers in the same row between the first and second layers. In this configuration, the Ni atom forms six bonds with surrounding Si atoms. A small rotation of the nearest dimers in the (001) plane is also observed. This configuration has an adsorption energy of -4.41 eV.

Other configurations can be reached upon adsorption:

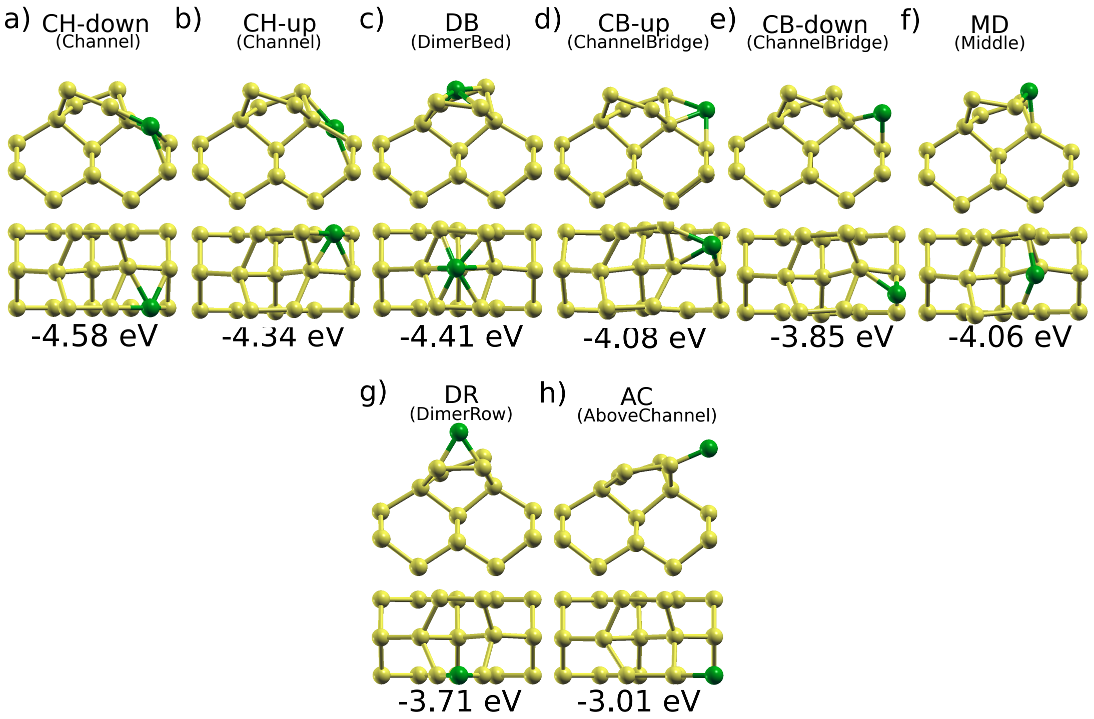

Figure 6: Stable adsorption sites of Ni on the Si (001) surface with their corresponding adsorption energies E_{ads} in eV.

- Sites #4 and #5 produce the configurations labeled as *ChannelBridge-down (CB-down)* and *ChannelBridge-up (CB-up)* (shown in Figure 6-d and -e). In CB-up and CB-down, the Ni atom is centered on the channel between the second and third layers and the Ni atom forms three bonds with the surrounding Si atoms. These configurations have adsorption energies of -3.85 and -4.08 eV, respectively.

- Site #6 produces the configuration labeled as *Middle (MD)* (Note: in this chapter we will use the label MD for Middle. In the rest of the thesis, MD refers to the Molecular Dynamics methodology), shown in Figure 2-f. In MD configuration, the Ni atom is located between two silicon atoms of two adjacent dimers of the same row. The Ni atom forms three bonds with the surrounding Si atoms. This configuration has an adsorption energy of -4.06 eV.

- Among the least energetically favorable sites, site #7 leads to a configuration labelled as *DimerRow (DR)* and shown in Fig. 5-g. In DR, the Ni atom is situated above a dimer, centered on the row axis. In this configuration, the Ni atom forms two bonds with the surrounding Si atoms. This configuration has an adsorption energy of -3.71 eV.

- Finally, site #8 produces the configuration labeled as *AboveChannel (AC)*, shown in Figure 6-h. In AC, the Ni atom is centered on the channel, above the first topmost Si layer. In this configuration, the Ni atom forms two bonds with the surrounding Si atoms. This configuration has an adsorption energy of -3.10 eV.

Through the analysis of energies associated with various stable configurations, our investigation has successfully identified the CH-up, CH-down, and DB configurations as the most energetically favorable adsorption sites for Ni on the Si(001) surface. We have observed that DB configurations exhibit formation energies that are only, respectively, 0.17 and 0.07 eV lower than CH configurations. Furthermore, these three preferred configurations exhibit a favorable energy difference of at least 0.33 eV compared to other adsorbed configurations. This observation is consistent with the higher number of bonds present in the CH-up, CH-down, and DB structures.

3.2.2 Surface diffusion of one Ni atom on Si(100) surface

After adsorption, we study the surface diffusion of Ni atoms on the Si(100) to validate the most favorable configurations on the surface. To do this, we start from the adsorbed stable configurations previously identified and we estimate the diffusion paths connecting them to the two most favorable adsorbed configurations, CH (up and down) and DB.

The results plotted on Fig. 7 show small activation barriers ranging from a low value of 0.002 to 0.35 eV, altogether with stabilization energies ranging from 0.35 eV to a large value of 0.73 eV. As can be seen in Figure 7, the diffusion from CB, down and up, to CH, down and up, requires small activation barriers of 0.01 and 0.10 eV with large energy gains of 0.73 and 0.25 eV, suggesting a fast diffusion from this configuration at the early stages of the deposition process. The diffusion from MD to DB requires an activation barrier of 0.14 eV, with an energy gain of 0.35 eV, in comparison with the diffusion to CH, up and down which requires activation barriers of 0.27 and 0.74 eV, but with favorable energy gains of 0.52 and 0.21 eV, respectively. Note that the diffusion from DR to DB requires a very low activation barrier of 0.002 eV (not plotted).

At this stage, based on the analysis of adsorption and surface diffusion studies, the two most favorable sites of the surface CH and DB are indeed the two most likely configurations on the Si surface at low temperatures due to the low activation barriers and associated energy gains.

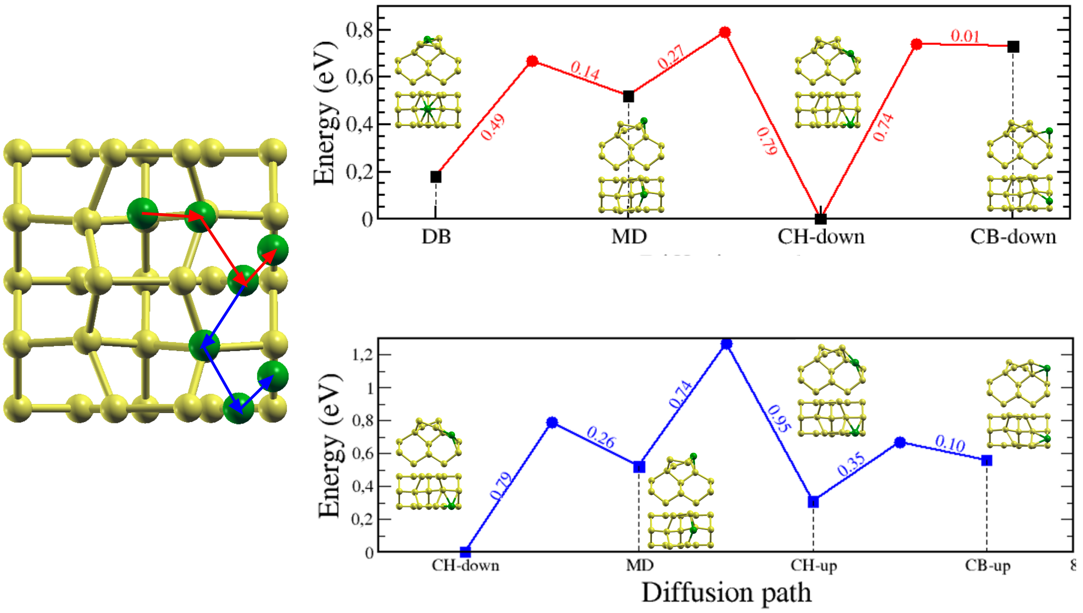

Figure 7: Energy diagrams of the surface atomic diffusions of one Ni atom adsorbed on the Si(100) surface. Activation barriers (numerical values in red and blue) are given in eV.

3.2.3 Insertion of one Ni atom in the topmost layers of the Si(100) substrate

In this section, we study the mechanisms of insertion of the nickel atom into the topmost layers of the silicon substrate. The objective is to estimate the ability of Ni, with the help of the characterization of the activation barriers, to insert into the surface layers of the silicon substrate as a function of the Ni coverage on the surface. This study is carried out first for one Ni atom. Prompted by results from the previous steps, we initialize this insertion step with the two most favorable configurations CH and DB.

3.2.4 Insertion from one adsorbed Ni atom

Insertion in the topmost layer

In the case of one Ni atom adsorbed on the surface, the Ni atom is able to find new stable inserted configurations when initialized in both CH and DB configurations. In the following, we describe the minimum energy path for the insertion from the DB configuration in Figure 8 from left to right, and from the CH configuration in Figure 8 from right to left.

The insertion of the Ni atom from the DB configuration is obtained after crossing an activation barrier of 0.32 eV. The system exhibits an energy gain of 1.32 eV compared to the DB configuration. This configuration is labelled Inserted Dimer Bed (IDB). In this configuration, the Ni atom is located between the third and fourth layers centered below the dimer row and is bonded to 6 Si atoms. The inserted configuration from CH is labeled Inserted Channel (ICH). This insertion exhibits a low activation barrier of 0.16 eV and is associated to an energy gain of 0.10 eV. In ICH, the Ni atom is located at the fourth layer and is bonded to 6 Si atoms. Finally, from ICH, it is also possible to diffuse towards IDB with a low activation barrier of 0.10 eV along with an energy gain of 1.05 eV.

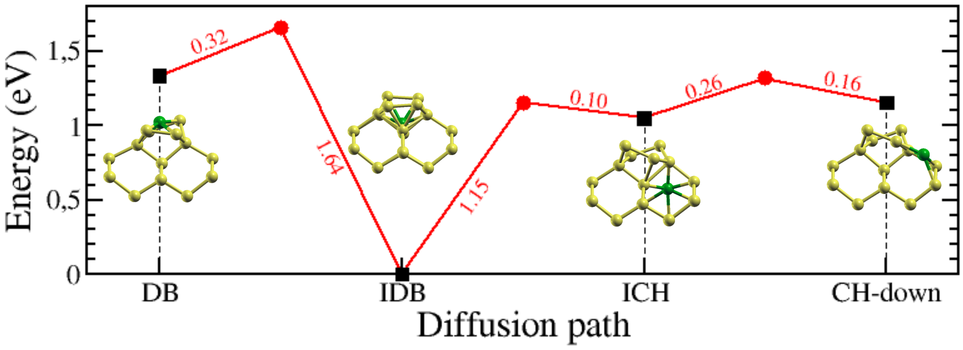

Figure 8: Insertion paths from DB (from left to right) and CH (from right to left) configurations into the topmost layers of the silicon substrate. The resulting configurations are labeled IDB (InsertedDimerBed) and ICH (InsertedChannel). Activation barriers (numerical values in red) are given in eV.

We also investigate the insertion barrier using CH-up/down to investigate if the activation barriers are affected by the dimer tiltings.

The insertion from the CH-up exhibits an activation barrier of less than 0.01 eV, even more favorable than the insertion from CH-down. Tilting of the dimers impacts the diffusion but results in the same final configuration once inserted.

From these two adsorption states DB and CH, the insertion is then favored over surface diffusion events. The Ni insertion is limited to the topmost layer of

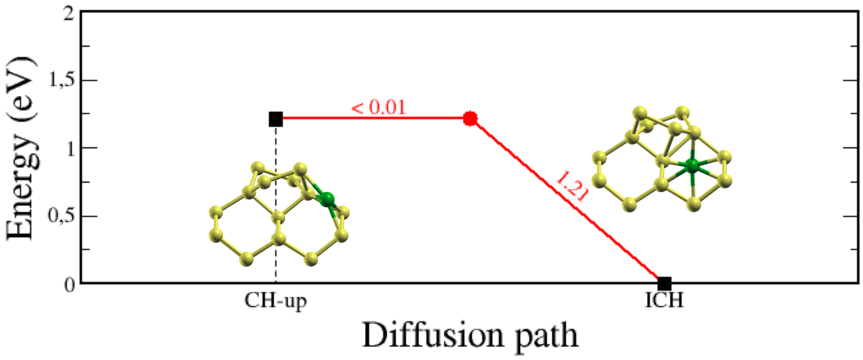

Figure 9: Diffusion path from CH-up to ICH configuration.

the surface below the dimer row. The resulting configuration is the first structuring configuration of the alloy formation where the Ni atom is located in IDB configuration.

Insertion deeper in the silicon bulk

On Figure 8, we observe that the diffusion from the 3rth layer (IDB) to the 4rth layer (ICH) is not favorable. In the following, we investigate the ability of the Ni atom to insert into deeper layers of the surface. For this, we investigate the formation energy of the Ni atom as a function of the surface penetration (See Figure 10).

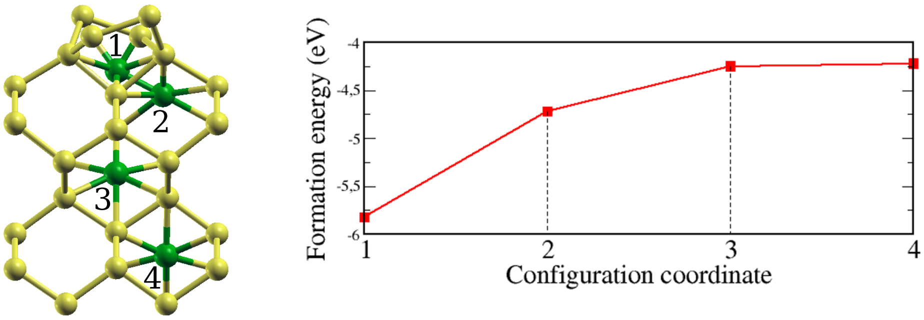

Figure 10: Stability of Ni atom from topmost layer (position 1) to deeper layer from the surface (position 4).

We observe a decrease in the formation energy as the Ni atom penetrates deeper into the surface. The formation energy tends to stabilize once the penetration reaches a depth of more than 7 layers, indicating that the Ni atom has reached the bulk region of the Si slab.

For the insertion process with the activation barriers associated with the diffusion of a single Ni atom in the bulk silicon (See Figure 11). We describe the minimum energy path from left to right. Initially, the Ni atom is positioned in a tetrahedral configuration and no activation barrier is found for the diffusion to a hexagonal configuration. Then, the Ni atom can diffuse to another hexagonal configuration with an activation barrier of 0.083 eV. After reaching this configuration, the Ni can diffuse in two different paths, one requiring an activation barrier of 0.088 eV and one requiring an activation barrier of 0.014 eV depending of the diffusion inside a hexagon or changing from one hexagon to another hexagon of the typical pattern of the silicon crystal. These diffusion barriers differ in one order of magnitude respect to the insertions from the surface.

3.3 Study of the behavior of a second Ni atom regarding a Si(100) substrate

3.3.1 Adsorption of a second Ni atom onto the Si(100) surface

Upon obtaining the initial adsorbed configurations for the first Ni atom, we proceed to investigate the adsorption of a second nickel (Ni) atom, focusing on the distance between the Ni atoms and its potential effects on the adsorbed configurations, as well as the associated energies and structural properties. As can be seen in Figure 12, the study is done for Ni atoms previously adsorbed in CH and DB configurations separately. For deposition, we use the sites of Figure 5 and we assume that the surrounding areas of each site will produce the same results.

Following relaxation, formation energies are calculated (Table 2). For that, we take the energy of DB and CH as references.

For the DB case, we observe that CH atoms tend to diffuse to CB and MD configurations. We observe this in #1, #2, #4, #5, #6, #7, and #8. Conversely, DB

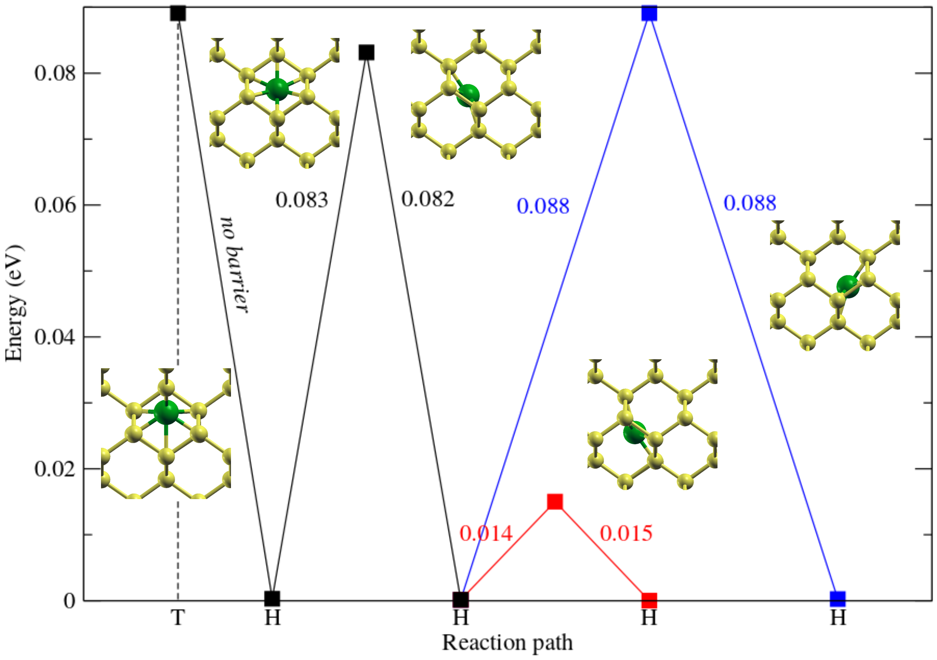

Figure 11: Diffusion paths for Ni diffusion in bulk Si. The complete set of transitions is divided in three parts, each showing their corresponding activation barriers in black, blue and red. T and H refer to Tetrahedral and Hexagonal respectively.

and DR do not exhibit diffusion. For the MD, the atoms placed on #16 and #18 diffused to DB configurations, while AC atoms diffused to CB configurations (as we can see in #23, #24, and #25). In the following, we compare the adsorption energies of the second adsorption with the values obtained for one adsorption. DB configurations are 0.19 eV less favorable while CH-down configuration are 0.10 eV more favorable. In the case of CB-up configurations, they are 0.24 eV less favorable, whereas the CB-down configuration exhibits an increased favorability of 0.22 eV. MD configurations have the same adsorption energy of MD alone. Finally, DR configurations are 0.18 eV less favorable.

In the case of CH adsorption, we focused on the CH-down configuration, assuming that CH-up would yield similar results. Similar to the observations made for the DB adsorption, we found that CH sites are prone to producing configurations different from the initial site. Consequently, we investigated the

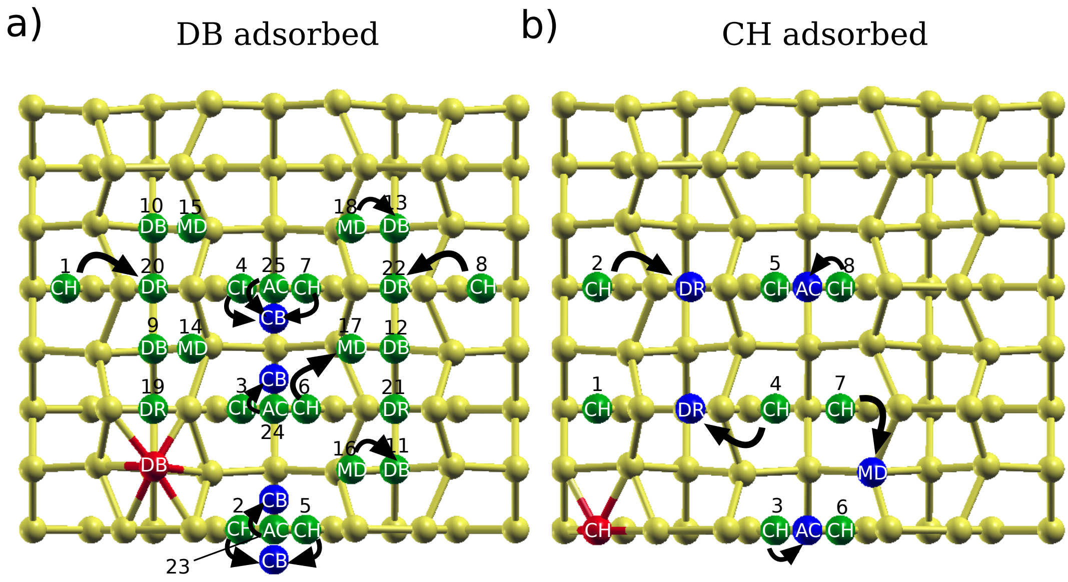

Figure 12: Top view of initial sites investigated on the deposition of a second Ni atom with their final adsorbed configurations. On left and right, the starting configurations contain a Ni atom previously adsorbed in DB and CH, respectively. These previously adsorbed atoms are indicated by red spheres. Initial sites for deposition are indicated by numbers while Ni atoms being deposited are indicated by green spheres. Arrows indicate the migration of Ni atoms being deposited from initial sites to final adsorbed configurations indicated by blue spheres. When no migration from sites is observed, deposition sites do not indicate arrows.

adsorption of a second CH atom using the same methodology as employed for DB. The resulting adsorption energies are presented in (Table 2).

On Figure 12 we can observe that, as in DB absorbed, CH sites tend to diffuse to other sites. Regarding the adsorption energies, the final configurations of CH-up exhibit an average value of -4.06 eV, which is 0.28 eV less favorable than the single adsorption. On the other hand, the average value for MD configurations is -4.25 eV, indicating an increased favorability of -0.19 eV compared to the single adsorption. The average value for DR configurations is -3.61 eV, representing a decrease in favorability of 0.10 eV compared to the single adsorption. Finally, the average value for AC configurations is -3.18 eV, reflecting a slight increase in favorability of -0.08 eV.

We can conclude that the potential energy surface of the system is modified under the presence of a first adsorbed atom in such a way that the deposition and further diffusion of a second atom can be affected.

To examine the impact of increasing the nickel coverage on the surface, we systematically augmented the DB coverage until all available DB sites on the surface were occupied. Following energy minimization, we observed that the DB configurations exhibited a notable penetration into the silicon (Si) surface, with an average penetration depth of 0.57 Å. This observation indicates that the penetration phenomenon is favored as the coverage of nickel is increased.

To summarize, configurations CH and DB are the two most energetically favorable sites of adsorption for the Ni on the Si(100)-c(4x2) surface. We also show that the presence of a first atom already adsorbed on the surface affects the stability of nearby sites and tends to favor interaction between Ni. A complementary study is then necessary to definitively confirm that CH and DB sites are the most favorable by studying the surface diffusion, *i.e.* determining the activation barrier, from other stable configurations of the catalogue toward CH and DB.

In addition, the configurations CH and DB, which are in strong interaction with the silicon substrate, seem to be good candidates suitable for allowing the insertion of nickel atoms into the topmost layers of the substrate. Noticing that the penetration of DB is favored when the coverage is increased.

3.3.2 Insertion of Ni with a first adsorbed Ni atom in the vicinity

We begin by initializing the structure with two Ni atoms positioned in two adjacent DB sites on the same dimer row (See Fig. 13 from left to right). The first insertion of one DB atom exhibits an activation barrier of 0.33 eV and is associated to an energy gain of 1.15 eV compared to the DB+DB. In the reached configuration the Ni atom reaches an IDB configuration while the second Ni atom slightly penetrates the topmost layer of the silicon substrate. The corresponding activation barrier shows that it is not affected by the presence of the second DB atom (0.33 eV vs. 0.32 eV obtained in the case of a single Ni atom). We observe that the energy gain is affected, being 0.17 eV less favorable in comparison with the insertion of one DB atom. From this DB/IDB configuration, two insertion

DB				CH			
Site (#)	Initial	Final	E_F (eV)	Site (#)	C_I	C_F	E_F (eV)
#1	CH-down	DR	-3.43	#1	CH-up	CH-up	-4.71
#2	CH-up	CB-up	-4.29	#2	CH-down	DR	-3.70
#3	CH-down	CH-down	-4.87	#3	CH-up	AC	-3.16
#4	CH-up	CB-up	-4.06	#4	CH-down	DR	-3.62
#5	CH-up	CB-up	-4.28	#5	CH-up	CH-up	-4.34
#6	CH-down	MD	-4.07	#6	CH-up	CH-up	-4.41
#7	CH-up	CB-up	-4.06	#7	CH-down	MD	-4.29
#8	CH-down	DR	-3.52	#8	CH-up	AC	-3.93
#9	DB	DB	-4.42				
#10	DB	DB	-4.35				
#11	DB	DB	-4.39				
#12	DB	DB	-4.36				
#13	DB	DB	-4.42				
#14	MD	MD	-4.60				
#15	MD	MD	-4.36				
#16	MD	DB	-4.39				
#17	MD	MD	-4.07				
#18	MD	DB	-4.42				
#19	DR	DR	-3.95				
#20	DR	DR	-3.63				
#21	DR	DR	-3.70				
#22	DR	DR	-3.71				
#23	AC	CB-up	-4.30				
#24	AC	CB-down	-4.26				
#25	AC	CB-up	-4.06				

Table 2: Adsorption energies E_{ads} obtained on the deposition of a second Ni atom. Adsorption energies are calculated taking DB and CH adsorbed energies as reference.

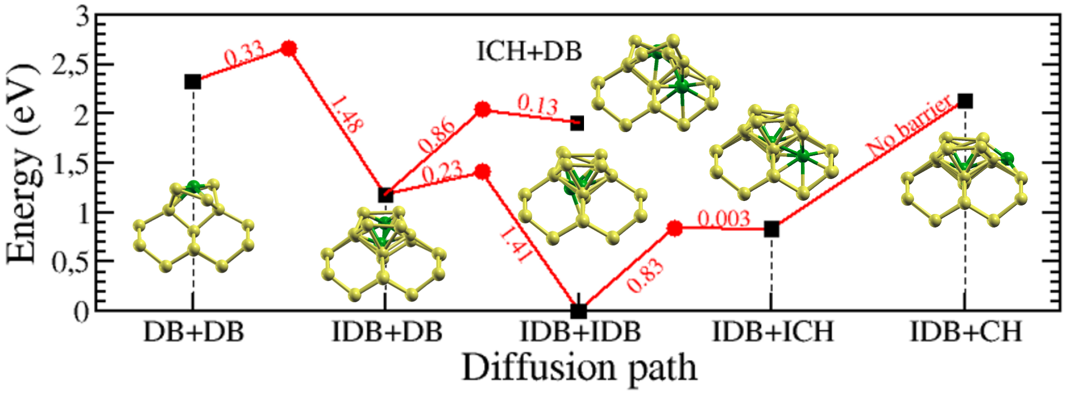

Figure 13: Insertion paths of two Ni atoms initially situated in DB configurations (from left to right) and insertion path of two Ni atoms initially situated in IDB + CH configuration (from right to left). Activation barriers (numerical values in red) are given in eV.

paths were considered. In the first path, the inserted IDB atom is pushed further to reach an ICH position. The resulting configuration is the structure DB+ICH. This diffusion requires an activation barrier of 0.86 eV and the system undergoes an energy loss of 0.73 eV, which is unfavorable. Alternatively, the system can also form a structure with two IDBs (IDB+IDB on Fig. 13), associated to an energy gain of 1.18 eV, compared to the DB/IDB configuration. This diffusion requires an activation barrier of 0.23 eV: we observe a notable decrease in the activation barrier. Thanks to the presence of IDB, the activation barrier to insert DB to IDB is then favored (compared to the insertion of a single DB (0.23 eV vs. 0.32 eV)) early in the deposition steps. Note that from this structure IDB+IDB, the diffusion of one of the IDB atoms toward an ICH position destabilizes the system and is therefore not favorable. This finding, in addition to the fact that the structure IDB+IDB is more favorable than the structure DB+ICH, suggests that silicidation forms layer by layer, from the top layer to deeper layers, but, proper demonstration requires additional calculations that are beyond the scope of the present work.

We also study the addition of a second Ni atom on an already inserted configuration IDB (from right to left on Fig. 13). Two cases have been tested: a new adsorption is performed above the IDB position, and an adsorption through the channel in close proximity of IDB.

- For the first case, the Ni atom is placed above the site #2 as defined in Figure 2-c: the added Ni atom relaxes to the DB configuration, and the IDB atom remains unchanged. The adsorption of this second Ni is associated with an adsorption energy of -4.06 eV, *i.e.* 0.35 eV less favorable compared to DB adsorption in the single atom case. In this configuration, we do not observe any local structure change.

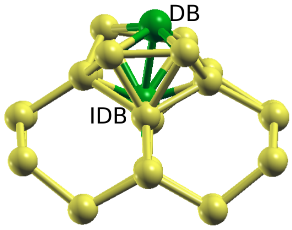

Figure 14: Adsorption of a DB atom on an IDB configuration.

- For the second case, the Ni atom is added above the site #1 as defined in Figure 5. Contrary to the case of the adsorption with a single atom, we observe here a spontaneous insertion of the Ni atom without activation barrier directly from the channel path towards the ICH configuration reaching a configuration IDB+ICH as obtained in Figure 13. We recall that for this insertion with a single atom, the activation barrier was 0.16 eV. The adsorption of this second Ni is associated with an adsorption energy of -4.85 eV, i.e. -0.27 eV more favorable than in the case of the adsorption of a single Ni atom from the gas phase or more favorable by -0.17 eV when comparing the complete paths to the ICH position. This insertion mechanism is favored because the presence of IDB locally elongates the Si-Si bonds in the channel, and more particularly modifies the local structure of the adjacent dimer (tilting and bondlength) which offers space to the atom arriving in the channel (which could be called ex-CH) to insert directly into ICH configuration. This trend is consistent with a favorable diffusion process and suggests a rapid formation of an alloy thanks to the favored insertion of Ni atom without any activation barrier.

as already said but in reverse, so reworded here, from the configuration IDB+ICH, the insertion of the atom in ICH is favorable to form the configuration IDB+IDB.

In summary, our study demonstrates that the Ni insertion is highly favorable through the channel of the reconstructed Si(100) surface during the initial stages of deposition. This insertion through the channel offers several advantages: (1) Ni diffusion to occupy the sites beneath the dimer row occurs with a relatively low activation barrier, making it more favorable through the channel compared to insertion through the dimer row itself, (2) this insertion allows occupation of the sites below the dimer row which then facilitates further insertion into the ICH sites and contributes to the system stabilization, (3) diffusion to IDB from ICH reduces the barrier to insert the Ni atom through the dimer row from the DB sites to IDB.

Our findings indicate that thermal activation is only required in the presence of dimers on the substrate surface. However, once this first barrier is overcome and the first atoms are inserted, the subsequent insertion of Ni atoms is favored across the entire surface. In the following, we will pursue the study of alloy formation based on these observations.

3.4 Towards the spontaneous formation of an alloyed layer on the surface

In this section the Ni coverage is increased with the aim of identifying the formation of a first silicide alloyed pattern from the previously identified stable structures. The idea is to identify locally the formation of Ni_xSi_y silicides such as Ni_3Si, Ni_2Si, and NiSi (Figure 15) depending on the Ni concentration. For this, first thermodynamic effects are studied when the Ni coverage is increased in order to identify the most important mechanisms in the silicide formation. Then, the formation of a local alloy is studied using mechanisms of deposition.

3.4.1 Building a high coverage pattern to study further deposition of Ni

Because we found that IDB and ICH are the most stable configuration, we initialized a final calculation with several Ni atoms at the IDB and ICH sites until obtaining a full coverage and performed energy minimization. In Fig. 16.a, we observe the Ni atoms forming a zigzag pattern where initial inserted IDB are

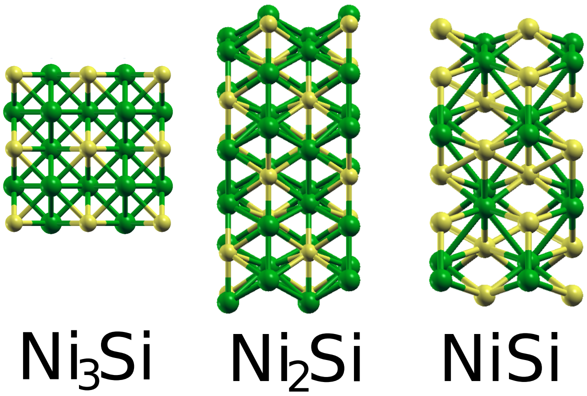

Figure 15: Structural patterns of different bulk silicides.

displaced from the previous identified configuration, while in Fig. 16.b, the Ni atoms remain in the ICH configurations. At this stage we can not state on the results obtained, either if such distorted pattern can occur at high coverage or either such effects are due to size of the simulation cell.

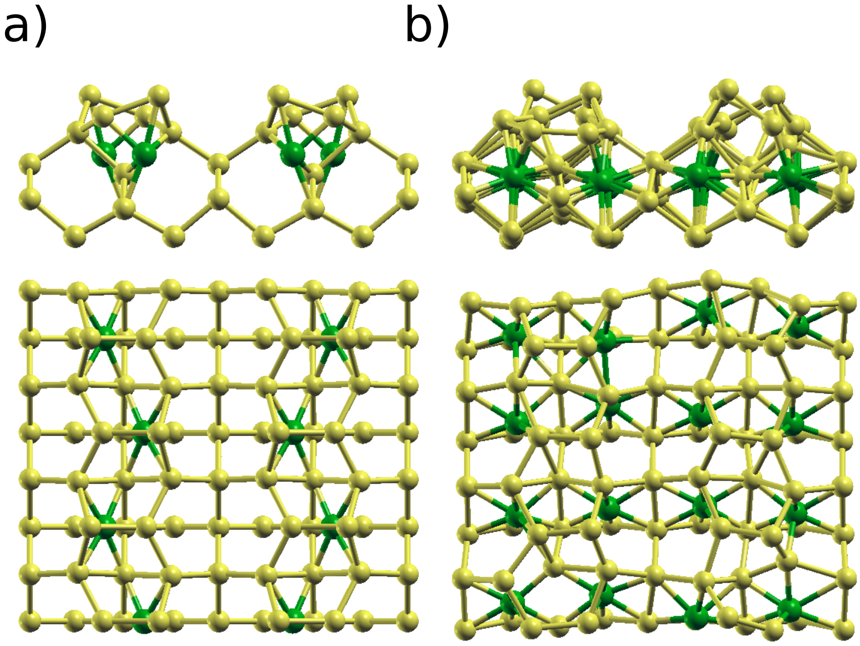

Figure 16: Relaxed atomic configurations of the silicon surface (top-view) with a full coverage a) with only IDB coverage and b) with only ICH coverage.

To pursue our study, we then modify our approach by increasing the coverage locally on the surface, where 3 IDB configurations are stabilized using 6 ICH in the vicinity. Based on the conclusions drawn in the previous section, such an assumption is justified by the favorable insertion of Ni atoms under the dimer rail, and by the spontaneous insertion of Ni atoms at the ICH site when the IDB sites are occupied. The starting point is a stable structure initially composed of three Ni atoms in IDB and six Ni atoms in ICH, for a total of 9 Ni atoms already inserted in the surface of the silicon substrate. This structure is chosen to avoid any effect related to the size of our simulation box and to avoid periodicity artefacts of the box, while reaching a sufficient number of Ni atoms to study the formation of an alloy nucleus. The relaxed configuration is shown in Figure 17. In this Figure, we notice in the final relaxed structure that two of the Ni atoms initially inserted in the ICH position (those most central in the structure), move out of their ICH position to reach a CH position as described above. We can note here that the displacement of the Ni atoms from ICH to CH contributes to the pure layer alignment of the Ni atoms as can be observed in some Ni_xSi_y alloys.

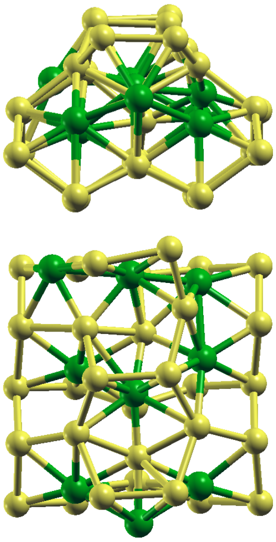

Figure 17: Relaxed 3 IDB + 6 ICH pattern to study additional Ni adsorptions.

3.4.2 Identification of an alloyed pattern

The purpose of the following paragraph is to demonstrate that by increasing the Ni coverage on the already identified insertion structures, Ni atoms can still penetrate spontaneously thus creating an alloyed mixed layer of 3:1 composition through self organization of both Ni and Si atoms.

Using this relaxed structural pattern (Figure 17), we add a Ni atom above the CH position, on a position that we have identified in blue on the Figure 18.a, for a total of ten Ni atoms. The final configuration after relaxation of this additional Ni atom is shown in Figure 18.a. Upon adsorption of this additional tenth Ni atom, we observe a structural rearrangement, of which a schematic of the structural rearrangement is provided in Figure 18.b to identify the associated movements where the panels 1 and 4 of Figure 18.b show the schematic view (slice) of Figure 18.a, respectively, and panels 2 and 3 describe the moves of both Ni and Si atoms occurring below the dimer row between the 3rd and 5th layer. We observe that the deposited Ni atom is finally adsorbed on a CH position. During this adsorption, a Ni atom initially located on a ICH site moves to a new configuration where the Ni atom goes deeper in the Si substrate. This site is labelled InsertedBulk (IB), shown in Figure 18.b in panel 4. At the same time, a Si atom is also moved slightly, to reach a centered position between four Ni atoms. The adsorption energy of this new atom is -4.87 eV. We observe this adsorption energy is more favorable than the CH adsorption on the pure Si surface (-4.87 eV vs. -4.58 eV).

Looking more closely at the local pattern formed, we find that Ni and Si atoms rearrange in a structure similar to the Ni_3Si alloy. In Figure 18.c, we present the local pattern extracted from the atomic structure shown in Figure 18.a (relaxed). If we compare this pattern with the perfect crystal structures of the Ni_3Si alloy, we clearly identify in pattern Figure 18.c an organization of the Ni and Si atoms, exhibiting thus the same local chemical environment of Ni as it exists in the Ni_3Si alloy, especially in the (011) orientation (see Figure 19). We compare the distances a and a′, and b and b′ of the Figure 18.c, and they present close values (2.62 Å and 2.48 Å, and 3.76 Å and 3.51 Å) that is to say weak relative differences of the order of 5.6 % and 7.1 % showing that the interatomic distances of the obtained pattern are close to the distances between the atoms in the Ni_3Si alloy crystal. Analyzing the a/b ratio in Figure 18.c we observe a value of 0.69. This analysis of the interatomic distances and a/b ratio corroborates with the favorable formation of an alloyed layer of composition 3:1.

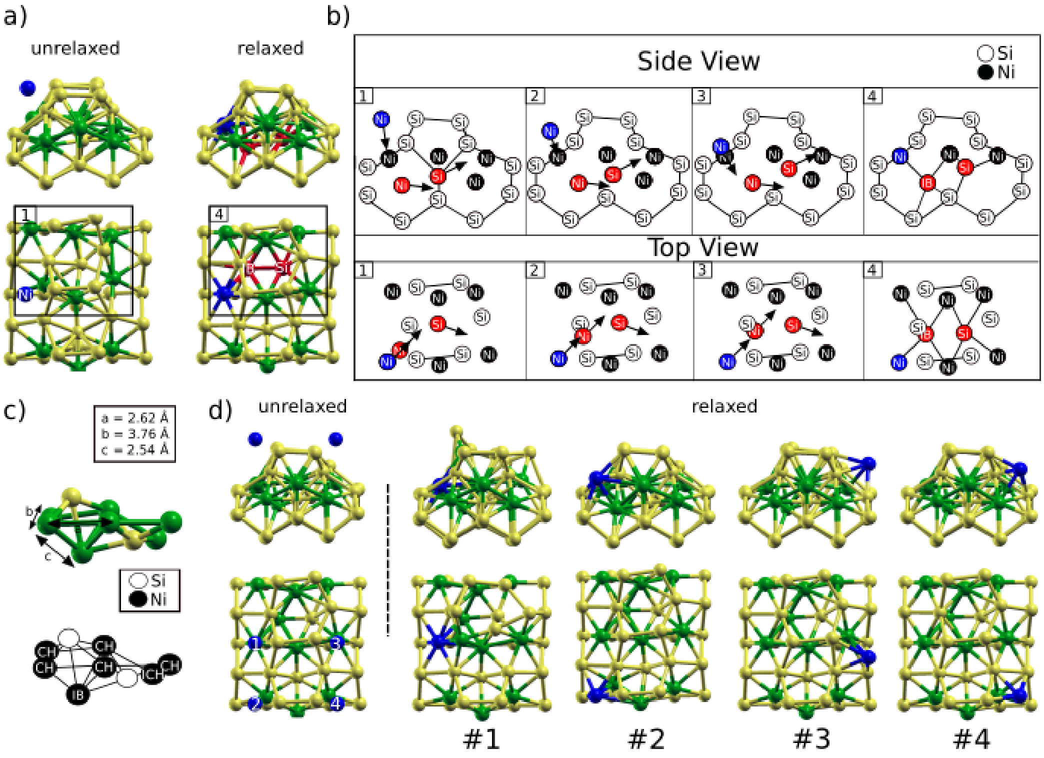

Figure 18: Results and schematic representations for the understanding of the formation of a Ni:Si alloyed layer with 3:1 composition. a) Adsorption of the tenth Ni atom. The starting configuration contains nine Ni atoms already adsorbed: three in IDB and six in ICH. The tenth deposition site is indicated by a blue sphere. The blue atom is the added Ni atom and the red atoms are the displaced Si atoms. b) Schematic representation of atomic rearrangement observed in a) Side and top view of the structures are shown from the region of interest. Panels 1 and 4 refer to the structures in a). Atoms are represented by spheres colored in grayscale according to their distance to the surface. Topmost layer is colored white. Dark green and yellow indicate respectively Ni and Si atoms having the most representative displacements. c) Local silicide formed: analysis on the distances altogether with an atomic positioning with respect to the layer indexation is shown on the left, meanwhile an identification of the atomic positions respect to the stable configurations previously identified is realized. Ni and Si atoms are represented by black/green and white/yellow respectively. d) Adsorption of the eleventh Ni atom on the relaxed structure shown in a). Initial sites for deposition are indicated by numbers on the structures.

Going further in the increase of the coverage of Ni, on the structure of Figure 18.a relaxed, the adsorption of a new Ni atom is performed at four different

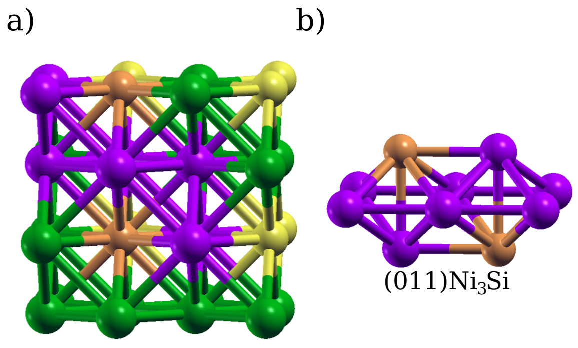

(001)Ni_3Si

(011)Ni_3Si

Figure 19: Local silicide formed. a) structural pattern of Ni_3Si is provided where the local alloy is highlighted using orange and purple colors. The correspondence with the local alloy is highlighted in b). Green and purple spheres are nickel atoms and yellow and orange spheres are silicon atoms.

sites on the surface, for a total of eleven Ni atoms. The same trend favoring mixing of Ni and Si species is observed. The initial positions are shown on Figure 18.d. We observe that the Ni positioned in 1 adsorbs between the first and second layers, thus creating space between the pure silicon layers formed by the dimers. The corresponding adsorption energy is -4.84 eV. The Ni atom cannot be further inserted spontaneously in this specific configuration because the CH site below is already occupied. The final configuration presents an interesting mechanism, allowing the upper Si layer to penetrate more Ni on the surface by an upward movement of Si atoms, which could be favorable by the further mixing of Ni and Si species. This mechanism is beyond the purpose of the paper but will be exploited later. For the tested position number 2, we obtain a typical configuration of a subsequent insertion in the substrate that is of interest for the understanding of the further mixing of the alloyed silicide layer. In particular, we observe that the deposited Ni atom takes place in a CH configuration, also pushing the ICH atom below towards the IB site, as observed above. The associated adsorption energy for this configuration is -4.29 eV, having a difference of 0.29 eV respect to the CH adsorption on pure Si surface. For investigated positions 3 and 4, we do not notice any tendency of insertion into the surface, whereas the deposited Ni atoms seems to be attracted toward the adjacent dimer row, confirming the tendency of Ni to interact with the whole silicon surface. The adsorption energies for these configurations are -4.16 and -4.54 eV, respectively. We suppose here that these reached positions are brought to stabilize further according to the degree of alloying formed on the second dimer row of our surface. We do not study further the atomic diffusion from these adsorbed configurations for clear computational limitations and we concentrate on the high coverage on a given dimer row.

Referring specifically to the adsorption from the tested position 2, we note that this spontaneous adsorption is accompanied by the movement of multiple atoms. This observation confirms that, during this additional insertion, the Ni atom becomes incorporated into the Si surface. The resulting chemical environment exhibits a composition similar to that of a Ni:Si layer with a ratio of 3:1, as evidenced by the comparable interatomic distances with its immediate neighboring atoms. Notably, this insertion process occurs without encountering any activation barriers for diffusion or atomic reorganization at the interface.

3.5 Discussion: comparison with experimental data

This thesis is being conducted within the framework of the European MUNDFAB - H2020 project. As part of this project, we were granted access to experimental data from X-Ray Reflectivity, in conjunction with High-Resolution Transmission Electron Microscopy, performed by the CNR-IMM team in Catania, Italy, using samples developed at LAAS-CNRS in Toulouse, France. In this paragraph, we utilize the data from the published article, including both the images and text. Details of how the samples were made can be found in the published article [84].

In this experimental work, a special emphasis on the comprehensive characterization of the as-deposited material and its interface with silicon using XRR analysis, in combination with HR-STEM analysis has been achieved giving us validation of the DFT calculations. XRR is an analytical technique that is sensitive to the electronic density of materials, making it particularly suitable for accurately describing potential Ni-Si intermixing and phase formation.

Figure 20.a) illustrates the XRR profile of the as-deposited sample, displaying typical interference fringes associated with layer thickness. The critical angle obtained from this profile corresponds to a density of 8.9 g/cm^3. Notably, a nickel layer is observed in the topmost region of the sample, with a thickness of approximately 8 nm. However, this value underestimates the actual deposited thickness. Consequently, a description solely consisting of a pure nickel layer on top of a silicon substrate does not fully capture the experimental curve. To achieve a more accurate fit, a refined model of the sample includes a second

layer in direct contact with the silicon substrate, as depicted in the figure's inset. This layer comprises a 3 nm-thick N-Si mixed layer with a density of 8 g/cm^3, corresponding to a Ni:Si ratio of 3:1.

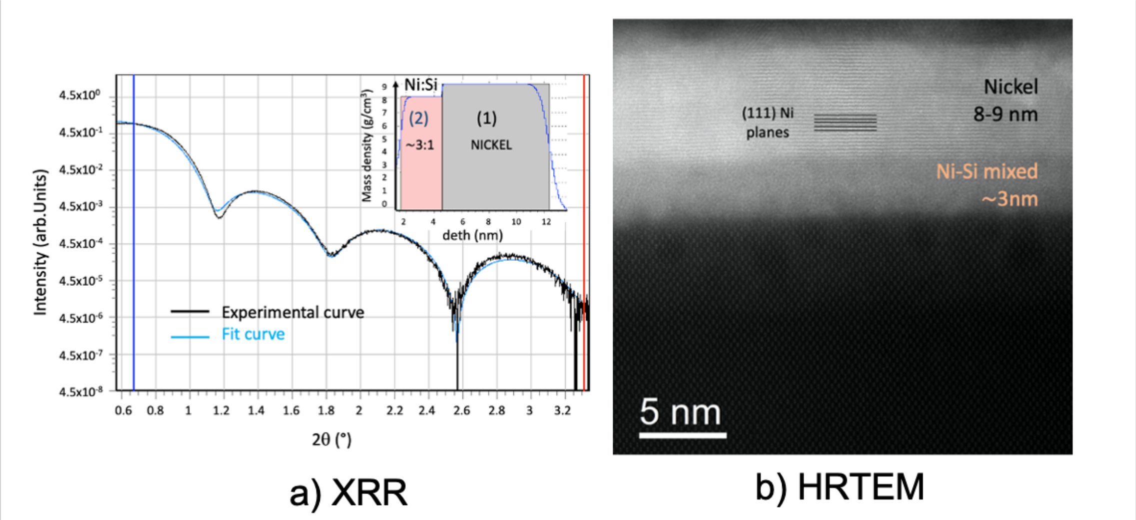

a) XRR

b) HRTEM

Figure 20: a) XRR profile of the as deposited sample, with the schematic of the layered structure and composition in the inset, b) HR-STEM cross-section of the as deposited sample. Reproduced from [84].

A similar scenario was observed through HR-STEM analyses, as illustrated in the cross-section image of the as-deposited sample presented in Figure 20.b). The topmost nickel layer consists of nanometer-sized grains, predominantly oriented along the [111] crystallographic direction. Immediately beneath the pure nickel layer, a mixed layer is detected, confirming the observation made using XRR. Notably, this mixed layer exhibits a low degree of lattice order, resembling an amorphous structure. This additional information provides further insights into the structural characteristics of the interface region.

Previous studies have reported similar Ni-Si mixing characteristics in samples where the nickel layer was deposited using sputtering techniques. However, considering that adatoms in evaporated layers are expected to possess lower energy compared to their sputtered counterparts, it is argued that intermixing arises due to adsorption-diffusion-injection mechanisms, as described in the theoretical dissertation. This suggests that the occurrence of intermixing is independent of the specific deposition method.

Furthermore, the observed Ni-Si mixing with a ratio of 3:1, as consistently identified by both experimental techniques, supports the notion of a driving force for nickel insertion into the silicon lattice. This finding aligns with the description provided by the experimental calculations, further reinforcing the validity and accuracy of the experimental results.

3.6 Conclusions

DFT calculations provide clear evidence of the formation of a native surface alloy during the deposition process, where Ni readily adsorbs and inserts onto clean Si(100) surfaces. This finding supports the experimental observation of rapid formation of the Ni_3Si alloy at the Ni/Si interface.

Our study reveals that at very low coverage, nickel atoms exhibit favorable insertion into the silicon substrate with low activation barriers. Once the initial nickel atoms are inserted, they facilitate the subsequent insertion of additional arriving atoms on the surface. However, this facilitated insertion mechanism is limited to the surface layers of the substrate, and deeper diffusions are not allowed. We therefore assume a layer-by-layer growth mode, which will be further investigated in this study.

We establish that the thermodynamic formation of this alloy occurs without encountering an activation barrier once the Ni coverage on the surface reaches a sufficient level. The as-deposited interface, formed prior to the activation of the silicidation process, consists of Si/Ni_3Si/Ni layers. Experimental results support and validate these findings.

However, it is important to note that our current analysis has focused solely on the energy aspects and does not provide a dynamic understanding of the process. To gain insight into the dynamics, larger-scale modeling techniques such as molecular dynamics and Monte Carlo kinetic methods are necessary. In particular, due to the absence of precise empirical potentials for such simulations, we will employ machine learning techniques to develop an interaction potential, enabling us to continue this purely ab initio study.

Chapter 4

Stabilization mechanisms on nickel-silicide/silicon interfaces from first principles

4.1 Introduction

In the previous chapter, it was observed that an alloyed interface with a composition rich in nickel, specifically (011)Ni_3Si, forms even at room temperature prior to any thermal activation in the silicidation process. Following the thermal activation phase, various orientations, thicknesses, and chemical compositions of silicide/Si interfaces can be found. Although the nickel-silicon system has many phases, the sequence can be divided into three stages based on the phase diagram: Ni-rich, NiSi, and $NiSi_2$ phases. While there is extensive literature available on bulk silicides [4, 15, 31, 32], there is currently limited description of interfaces. Because studying interface properties in experiments remains difficult, there is an interest in using atomistic simulations instead. In this context, the density functional theory (DFT) is a relevant tool. The study of the stability of these interfaces and their description from atomistic simulations contribute to the whole understanding of the silicidation process serving as reference points of the process, pointing to favorable silicide phases, with their orientations and stackings. In addition, the obtained structures will serve in the next chapter as a database for the development of a machine-learning interaction potential.

This chapter focuses on a thorough investigation of the stabilization mechanisms of nickel-silicide/silicon interfaces that are likely to form after the thermal activation phase of the silicidation process. DFT calculations are employed to analyze the structural and charge properties of these interfaces following energy minimization.

4.2 Results

The initial step involves a comparison between the bulk properties of silicide and silicon to serve as a basis for modeling the interfaces. This comparison entails analyzing the stacking and the orientation in order to construct the interfaces. Then, the stabilization mechanisms are studied by analyzing the structural and charge properties of the interfaces after energy minimization of both atomic positions and box sizes. For this last part, the root mean square error (RMSE) and Bader charge difference are used. In addition, a case study is presented, where atomic minimization is performed using a box fixed at the silicon lattice parameter.

4.2.1 The role of nickel-silicide and silicon structural properties on the modelling of nickel-silicide/silicon interfaces

In this part, we justify the selected structures used to build the interfaces. In terms of chemical compositions, we consider Ni_3Si, Ni_2Si, and NiSi and Si. To build the interfaces effectively we estimate the corresponding lattice parameters by DFT calculation and analyze their structural properties. Starting with the Ni_3Si composition, the Ni_3Si silicide can be found in three phases; labeled as β_1, β_2, and β_3. In this work, we use the phase β_1 which is the most stable phase at room temperature and is well described in the literature. It is indeed a face-centered cubic (fcc) structure (shown in Figure 21). We estimate its lattice parameter using DFT calculations and we obtain a great accuracy of 0.11 % when compared to experimental measurement [See Table 3]. For Ni_2Si composition, two allotropic forms are reported in the literature. These structures are labeled as δ and θ [31]. Because it is reported as the more thermodynamically stable phase at low temperatures (δ phase was found to transform to θ at 806 ^{o}C [85]) we will use the δ phase which is an orthorhombic structure. Our estimation of the lattice parameters also leads to great accuracy when compared to experimental measurements [See Table 3]. For the NiSi composition, the most stable structure has an orthorhombic primitive cell. We reproduce the experimental values with great accuracy and obtain relative errors of 1.23 %, 0.03 %, and 0.16 % with respect to experimental values. Particularly, in this case, we obtain three values when compared to DFT due to the orthorhombic nature of the NiSi structure. Finally, for silicon, the structure at room temperature is a well-known diamond structure consisting of two interpenetrating face-centered cubic (fcc) lattices. We reproduce the experimental lattice parameters with great accuracy, where we obtain a value of 0.55 % of relative error with respect to the experimental values.

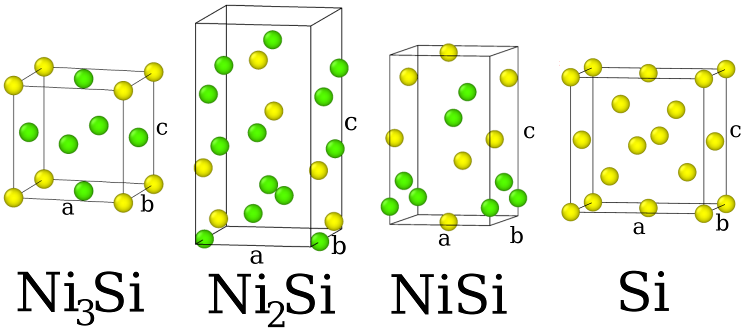

Figure 21: Structural patterns of silicides and bulk silicon. Si atoms are shown in yellow, Ni atoms in green.

Structure	Method	a (Å)	b (Å)	c (Å)
Ni_3Si	Exp [86]	3.506	3.506	3.506
	PAW	3.510	3.510	3.510
Ni_2Si	Exp [87]	3.732	5.009	7.066
	PAW	3.743	4.995	7.085
NiSi	Exp [88]	3.325	5.177	5.616
	PAW	3.366	5.179	5.607
Si	Exp [89]	5.430	5.430	5.430
	PAW	5.460	5.460	5.460

Table 3: Comparison between the lattice parameters obtained through DFT calculations in this study and the experimental values reported in the literature.

In order to model effectively different silicide/silicon interfaces, it is essential to analyze the possible silicide orientations and the structural planes in contact with the silicon. This analysis is important to minimize the mismatch between the two simulation boxes and to closely match the two different systems. This lattice mismatch imposes strain and energy loss on the systems and requires enlarging or compressing the slabs forming the interfaces. During interface construction, we compare silicide unit cells built using several crystalline orientations and rotation with the (001)Si unit cell. In the meantime, we also limit the maximum box sizes L_x and L_y to 15.45 Å to avoid excessive computational demanding calculations, where the $\hat{x}$, $\hat{y}$, and $\hat{z}$ axes are defined along the [100], [010], and [001] crystalline directions of the $\sqrt{2}$Si(100) slab. With such criteria, we select the interface minimizing lattice mismatch.

The selected orientations exhibit lattice mismatches with the silicon slab going from 1.5 % to 8.8 % (shown in Figure 22). In particular, for Ni_3Si, we first use a Ni_3Si structure oriented in (001) direction but additionally rotated in 26° respect to $\hat{z}$ axis. We name this particular orientation as (001)-26°Ni_3Si, whose lattice mismatch is of 1.5 % and 1.5 %. Then, because we demonstrated in the previous chapter that the (011)Ni_3Si orientation is likely to emerge during nickel deposition, we also include that particular interface whose lattice mismatches is much higher (3 % and 9 %). Finally, for the other chemical composition, we obtain lattice mismatches of respectively 3.1 % and 3.0 % for Ni_2Si and 8.8 % and 0.5 % for NiSi.

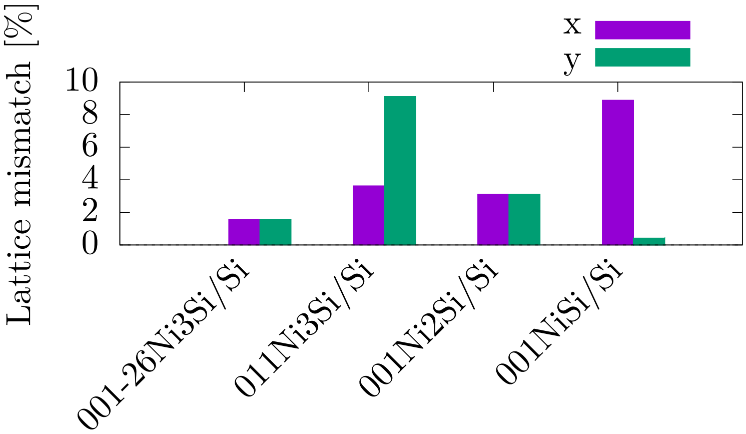

Figure 22: Lattice mismatches between the oriented silicides and silicon slabs used. The relative difference values are shown in percentage. The values in the $\hat{x}$ and $\hat{y}$ directions are shown in purple and green, respectively.

Each interface is built using a supercell of crystalline silicon that has initially a thickness of 15.45 Å in $\hat{x}$ and $\hat{y}$ directions. Along the $\hat{z}$ direction, the thicknesses of the silicon slabs are 21.85 Å, which correspond to 17 layers of silicon with 16 atoms each. On the silicide slabs, the same thicknesses of the silicon slabs are used in the $\hat{x}$ and $\hat{y}$ directions. At least 13.08 Å of thickness are used on the silicide slabs in the $\hat{z}$ direction, which corresponds to around 300 atoms per silicide slab, varying in each of the silicide structures. The two bottom layers of the silicon substrate are kept fixed to reproduce the bulk and a monolayer of thirty-two hydrogen atoms is used to saturate the dangling bonds of the bottom layer of the silicon substrate. A vacuum region of 15 Å is placed above the silicide slabs. The oriented Ni_xSi selected slabs are placed on top of the $\sqrt{2}$Si(100) slab, adapting initially the silicide box sizes to the silicon box size. Here, silicon surface reconstruction is not considered. In order to stack effectively the different slabs we take into consideration their different topologies. For this, multiple stackings are tested using single-point calculations to determine the most energetically favorable. These stackings include those where Ni and Si atoms are positioned on top of Si atoms, as well as those where Ni and Si atoms are located between two Si atoms. Once the most favorable stacking configuration is selected, the interfaces are built, as shown in Figure 23.

To analyze the selected stackings of Figure 23, we study the chemical composition and the stoichiometry of the layers in contact at the interface. On the silicon slabs, the atoms of the silicon top layers are equidistant, forming squares of 3.86 Å of side. While on the silicide slabs, the regions representatives of the silicide stoichiometries are shown by red squares on the top part of Fig 23. We can observe that on (011)Ni_3Si/Si interface, the selected stacking is such that the silicide bottom layer is composed of Ni atoms with the same position on the $\hat{z}$ direction, here the Ni-Ni distances in $\hat{x}$ and $\hat{y}$ directions are 2.57 and 3.86 Å, respectively. On the (001)-26Ni_3Si/Si interface, the selected stacking is such that the atoms of the silicide bottom layer have also the same positions in $\hat{z}$ direction, but with Ni-Ni distances equal to 2.44 Å. On the (001)Ni_2Si/Si interface, the Ni and Si atoms of the silicide slab that are in direct contact with the silicon slab have not the same position in $\hat{z}$ direction. These atoms have Ni-Ni and Si-Si distances both equal to 3.79 Å in $\hat{x}$ direction, and to 4.64 Å in $\hat{y}$ direction. On the NiSi/Si interface, the Ni and Si atoms of the silicide slab that are in direct contact with the silicon slab have not the same position in $\hat{z}$ direction. These atoms have Ni-Ni and Si-Si distances both equal to 3.86 Å in $\hat{x}$ direction, and to 5.15 Å in $\hat{y}$ direction.

4.2.2 Stabilization mechanisms on nickel-silicide/silicon interfaces

We explore the mechanisms responsible for stabilization by examining the structural and charge properties of the interfaces subsequent to the energy minimization of both atoms and boxes. In particular, we show the root mean square error (RMSE) in position compared to the bulk as well as Bader charge differences. In addition, we present a case study where the silicon lattice parameter is employed without the minimization of simulation box sizes. It is noteworthy to point out that our modeling approach involves the utilization of two joined slabs to construct the interface. In experiments, the silicon plays the role of a substrate and it is considered to have an infinite supply, necessitating the silicide to adapt to the lattice parameter of the silicon. In our study, box minimization is used to identify an optimal structure. Due to the similar thickness of the two slabs, the silicon slab playing the role of the substrate is not well represented and, as we will see in the chapter, the silicon slab can also adapt to the silicide slab.

Structural analysis

To study the stabilization mechanisms on the various interfaces built, we perform energy minimization of both atoms and simulation boxes. The resulting structures are depicted in Figure 23 showing side and top views of the interface regions in the supercells. Upon analyzing the atomic displacements within the structures, we note that the (001)NiSi/Si(100) and the (001)-26Ni_3Si/Si(100) interfaces have the largest distortions on the silicon top layers. On the (001)-26Ni_3Si(100) interface we observe that dimers formed on the silicon top layer.

The (001)NiSi/Si(100) interface exhibited substantial displacements resulting in dislocations on both silicon and silicide slabs. In the (011)Ni_3Si/Si(100) interface, the silicon top layer experienced large displacements, forming the same pattern of the silicide slab. Conversely, on the (001)Ni_2Si/Si(100) interface, apparently no distortions are observed. Therefore, we observe that the displacements of the atoms on the top silicon layer are strongly related to the stacking between slabs, which is closely related to the slab orientations and lattice mismatches. This is clearly seen on the (001)-26Ni_3Si interface, where the attempt to minimize the lattice mismatch produced significant atomic displacements at the interface region. We, therefore, can conclude that dislocations emerge at the interface regions after atomic and box minimization of the structures as stabilization mechanisms associated with the slab stackings.

In order to quantify the atomic displacements after energy minimization, we measure the RMSE when compared to the structure of the bulk reference slabs. For the latter, we select the box sizes of the minimized supercells in order to decorrelate the displacement due to box size differences and focus only on the interparticle distances. In Figure 24 we can observe the total RMSE values of each interface along with the same quantity when filtering only the silicide and silicon contributions. We observe the (001)NiSi/Si(100) interface exhibits the largest RMSE value, followed by the (001)-26Ni_3Si/Si(100), (011)Ni_3Si/Si(100) and (001)Ni_2Si/Si(100) interfaces. Looking at the slab contributions, we observe that the silicon slab contributions are larger than the silicide contributions on the (001)-26Ni_3Si/Si and (011)Ni_3Si/Si interfaces. Meanwhile, on the (001)Ni_2Si/Si and (001)NiSi/Si(100) interfaces the silicons slab contributions are similar to the silicide contributions with the silicide contribution only slightly larger in the (001)Ni_2Si/Si interface. At this stage, we do not observe a direct relation between the mismatch and the total atomic displacements on the interfaces.

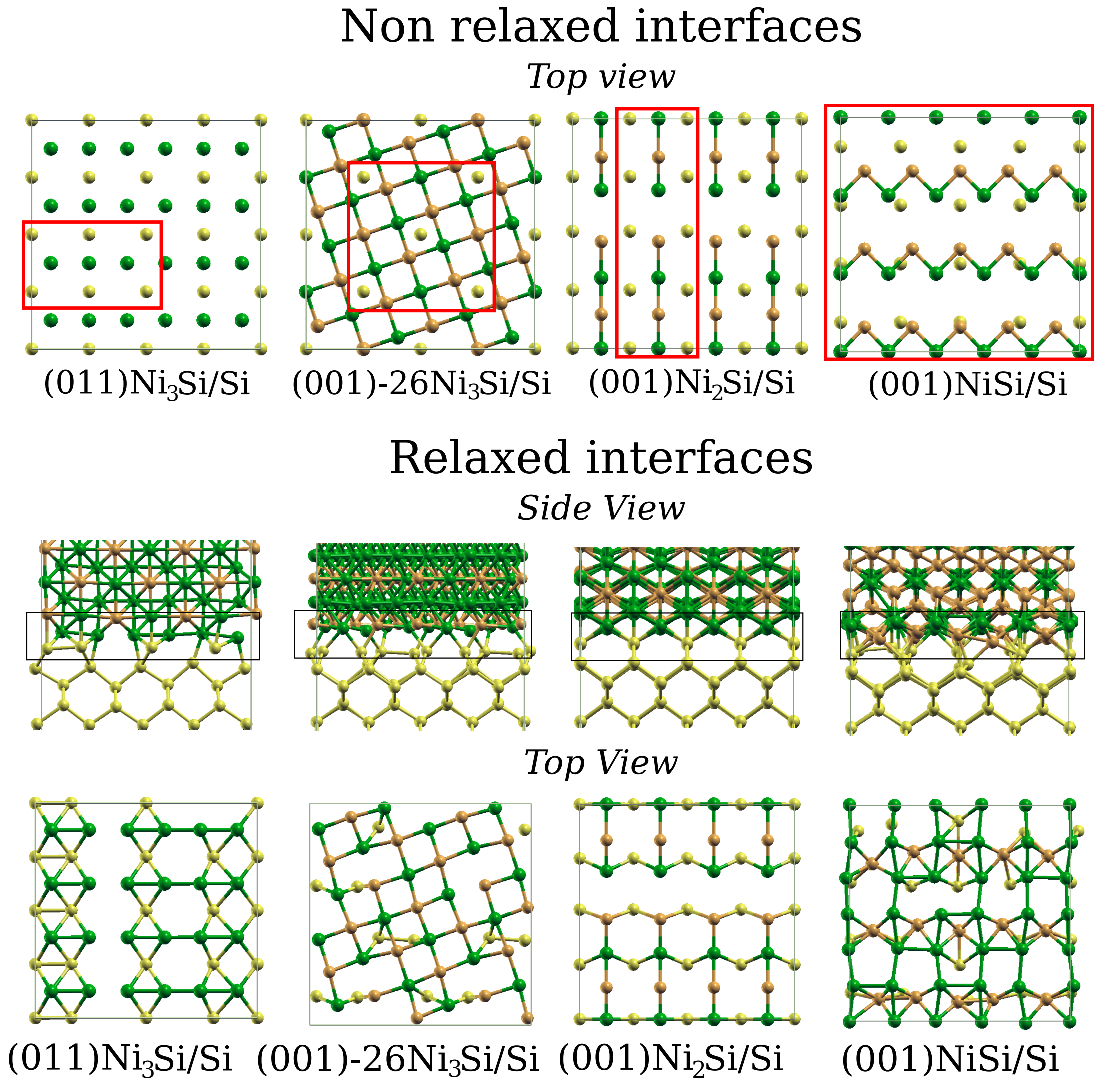

Figure 23: Interface structures before and after energy minimization. On top, the top view of the stacking of the different non-relaxed interfaces. Only the bottom silicide layer and the top silicon layer are shown. On the bottom, top and side view of the relaxed interfaces. Only interface regions are shown. Si atoms belonging to the silicon and silicide slabs are shown in yellow and orange, respectively. Ni atoms are shown in green.

The total RMSE values obtained possess contributions produced from dislocations occurring at the interface regions as well as contributions from the

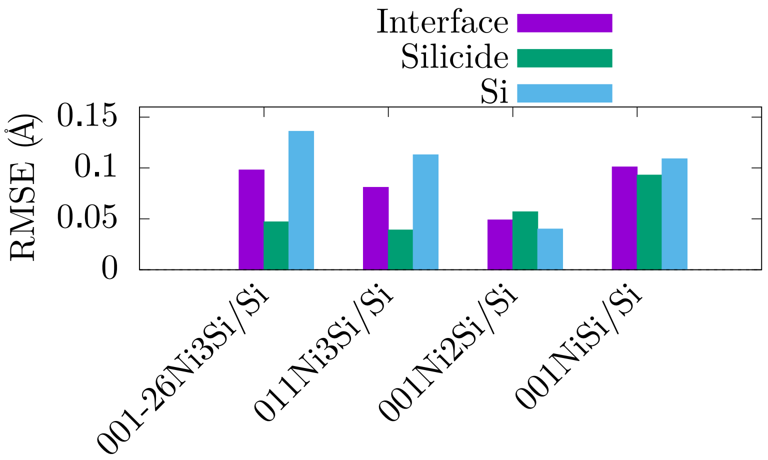

Figure 24: Analysis of the atomic displacements that occurred in the interfaces after energy minimization. The analysis is made by means of the mean square displacement error. The histogram shows the contributions of the silicide and silicon slabs. The total values are shown in purple, while the silicide and silicon contributions are shown in green and light blue respectively.

shrinking or enlargement of the entire slabs. In the following, we wish to distinguish these contributions in detail. As such, we measure the slab contributions in each of the spatial directions. The values are shown in Figure 25. Firstly, for the (001)-26Ni_3Si/Si(100) interface, we can observe that contributions from the silicide show values lower than 0.05 Å, indicating that the atoms in the slab are close to the crystalline bulk positions. On the silicon slab a large value is observed on the $\hat{x}$ direction, which is mainly produced by the large atomic displacements on the silicon top layer. The silicon slab contributions in $\hat{y}$ and $\hat{z}$ direction present values lower than 0.10 Å and 0.05 Å, respectively. Secondly, regarding the (011)Ni_3Si/Si(100) interface, the contributions from the silicide slab are lower than 0.05 Å, with a slight increase on the contribution in $\hat{z}$ direction. On the silicon slab, the contributions in $\hat{x}$ and $\hat{y}$ direction are close to zero, while a large value close to 0.18 Å is observed in $\hat{z}$ direction. This large value corresponds mainly to a shrinking of the silicon slab without the presence of dislocations at the interface region. This result seems to be only related to a stabilization mechanism produced by the elastic energy of the system. Thirdly, in the case of the (001)Ni_2Si/Si(100) interface, we observe that the silicide contribution in the $\hat{x}$ direction is close to zero, while the contribution in the $\hat{y}$ direction is lower than 0.10 Å. The contribution in the $\hat{z}$ direction is close to 0.05 Å. On the silicon slab, the contributions in the $\hat{x}$ and $\hat{y}$ direction are close to zero, while the contribution in the $\hat{z}$ direction is close to 0.05 Å. Finally, on the (001)NiSi/Si(100) interface the silicide contribution in the $\hat{x}$ direction is close to 0.05 Å. The contribution in the $\hat{y}$ direction is the smallest contribution of the slab with a value lower than 0.05 Å, while the contribution in the $\hat{z}$ direction is close to 0.10 Å. On the silicon slab the contributions in the $\hat{x}$, $\hat{y}$, and $\hat{z}$ direction are similar, with values close to 0.80 Å.

Therefore, after analyzing in detail the RMSE contributions in the $\hat{x}$, $\hat{y}$, and $\hat{z}$ direction, we conclude that with the studied interfaces, the contributions in the $\hat{x}$ and $\hat{y}$ directions are strongly related to the stacking of the joined slabs, while the silicon slab contributions in the $\hat{z}$ direction are strongly related to the lattice mismatches of the interfaces. We note that the RMSE contributions of the silicon slabs are in the same order as the average values of the lattice mismatches.

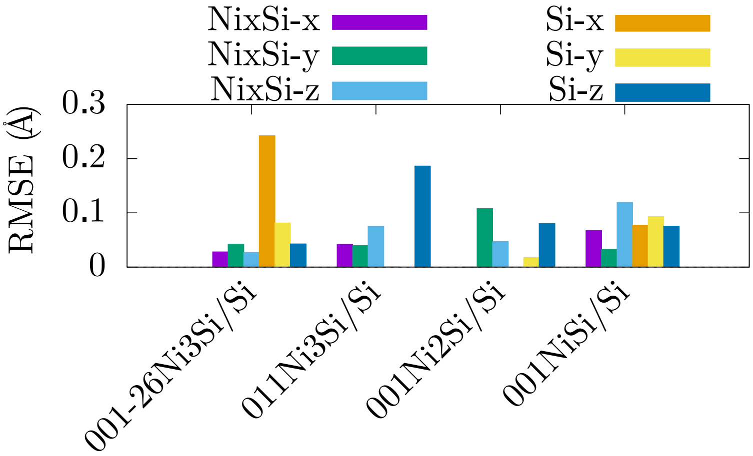

Figure 25: Detailed analysis of the atomic displacements that occurred in the interfaces after energy minimization. The analysis is made by means of the mean square displacement error. The histogram shows the detailed contributions of the silicide and silicon slabs in the $\hat{x}$, $\hat{y}$, and $\hat{z}$ directions. Silicide contributions in the $\hat{x}$, $\hat{y}$, and $\hat{z}$ directions are shown in purple, green, and light blue, while silicon contributions in the $\hat{x}$, $\hat{y}$, and $\hat{z}$ directions are shown in orange, yellow and dark blue.

In summary, our structural analysis demonstrates that dislocations serve as stabilization mechanisms, which are influenced by the orientations of the slabs, lattice mismatches, and stackings. In particular, when attempting to reduce the lattice mismatch by rotating the silicide slabs, significant dislocations are observed at the interface regions. A detailed analysis of the atomic displacements on the silicon slabs along the $\hat{x}$, $\hat{y}$, and $\hat{z}$ directions reveals a correlation between the lattice mismatch and the atomic displacements in $\hat{z}$ direction, in the absence of dislocations. This particular finding seems that the elastic energy resulting from the initial lattice mismatch contributes to this stabilization mechanism.

Charge properties

In this section, we are interested in correlating the charge properties to the stabilization mechanisms occurring at the interfaces. For that purpose, we first evaluate the atomic charges using the Bader approach [90], which only considers valence electrons, and then compare the values obtained in the interfaces with what is expected in the bulk regime. Ultimately, we measure the charge transfers occurring at the interface regions. We expect to observe a correlation between charge transfers and the nickel concentration of the silicides slabs, the chemical composition of the layers in contact, and the dislocations occurring at the interface regions. Figure 26 shows the charge differences on the relaxed interfaces when compared with their respective bulk charges. Additionally, average values of these charge differences are quantified in Figure 27. We only focus on the charge differences at the interface regions due to the negligible values obtained at the bulk regions, and additionally, surface effects are out of the scope of this work.

Looking at Figure 26, the analysis of the charge differences clearly shows charge transfers on the (011)Ni_3Si/Si, (001)Ni_2Si/Si and 001NiSi/Si interfaces at the interface regions. On the (011)Ni_3Si/Si interface we observe that the silicon top layer experienced charge transfer values lower than 0.5 electrons, while some rows of silicon atoms below experienced charge transfer values in a range that goes from -2 to 2 electrons. On the silicide slab, we note small charge differences, where the Ni atoms have gained 0.10 electrons while Si atoms lost 0.10 electrons. The average value for the charge difference at the interface region in this interface has a value of 0.24 electrons/atom. On the (001-26)Ni_3Si/Si interface, we note that although several dislocations of the silicon atoms at the interface are observed, the charge differences are negligible. The silicide slab presents charge differences similar to those described in the (011)Ni_3Si/Si case. In this interface, the average value for the charge differences at the interface region has a value of 0.14 electrons/atom. By comparing the charge differences obtained between the (011)Ni_3Si/Si and (001)-26Ni_3Si/Si interfaces we note that different charge transfers occurred. This result is attributed to the fact that the layers that are in contact with the silicon slab in these two interfaces have different chemical compositions. Also, the dislocations occurred in these interfaces are different due to their different stackings. On the (001)Ni_2Si/Si interface, we can observe that most of the charge differences occurred on the silicide slab. Here, we can observe that some of the silicon atoms of the silicide slab that are in contact with the Si slab lost 2 electrons, while there is a row of Ni atoms that

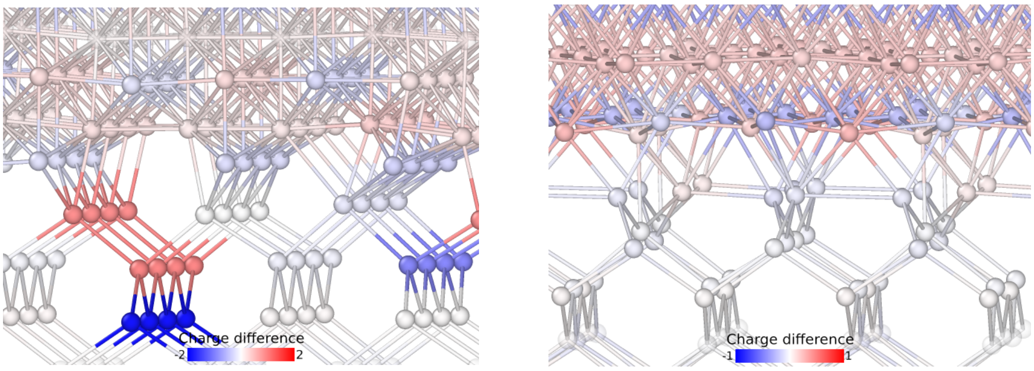

(011)Ni_3Si/Si (001)-26Ni_3Si/Si

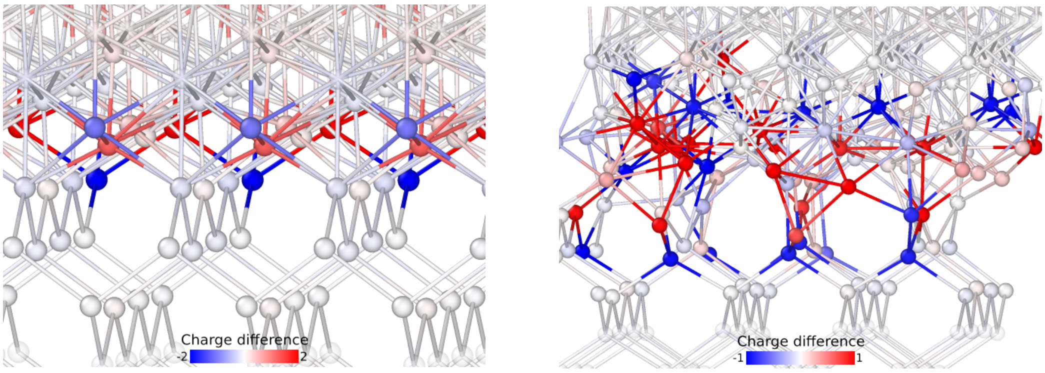

(001)Ni_2Si/Si (001)NiSi/Si

Figure 26: Charge differences of the relaxed interfaces compared to bulk charges. The interfaces are shown in a 3D view at the interface regions. The charge differences are shown in a gradient color coding going from blue to red, where blue and red represent negative and positive values respectively. Each interface has its own scale.

gain 1 electron. On the silicon slab, we observe a row of silicon atoms that gain 2 electrons. We note that in this interface the silicide contribution to the RMSE displacements is larger than the Si slab contributions. In this interface, the average value for the charge differences at the interface region has a value of 0.24 electrons/atom. On the (001)NiSi/Si interface, we observe that the charge differences occurred at both silicide and silicon slabs, where all the dislocations at the interface region seems to exhibit charge differences. These charge differences are in the order of the 2 electrons. By looking at the atomic displacements at the interface on Figure 24, we observe that this interface presents large numbers for both silicide and silicon slabs. In this interface, the average value for the charge differences at the interface region has a value of 0.24 electrons/atom.

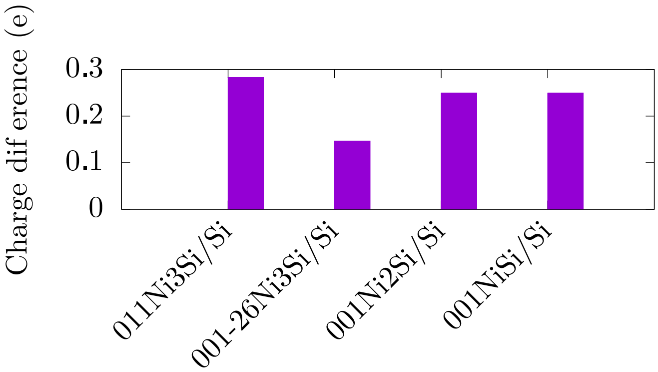

Figure 27: Charge difference average values of the different interfaces. Charge differences are measured in the unit of electrons, and only atoms at the interface regions are considered.

From this study of the Bader charges, we conclude that the atomic displacements after interface minimization are accompanied by a charge transfer at the interface regions in values varying from 1 to 2 electrons. In addition, the (001)-26Ni_3Si/Si interface is the one experiencing the smallest charge transfer at the interface regions, with a value of only 0.14 electrons/atom while the (011)Ni_3Si/Si interface is the largest with a value of 0.24 electrons/atom. The different values obtained are attributed to the different chemical compositions of the layers in contact as well as the different dislocations occurring at the interface regions.

The case of the (011)Ni_3Si/Si at Si lattice parameter

Previously we studied the structural and charge properties of the interfaces after both atomic and box minimization. In the following, we focus on the particular case of the (011)Ni_3Si/Si interface when the simulation box size is fixed at the Si lattice parameter. For this, we apply atomic minimization without performing box minimization. We remind that, as can be seen in Figure 22, the (011)Ni_3Si/Si interface has high mismatch values. In this study, we expect to observe large dislocations on the silicide slab, produced by the high strain that is imposed on the slab.

After applying atomic minimization, the structure obtained is shown in Figure 28-b. By analyzing qualitatively the structural properties of this structure we observe that the silicon slab exhibits atomic displacements that are similar to those obtained in the (011)Ni_3Si/Si interface when both atomic and box minimization was applied. On the silicide slab, we observe that large atomic displacements occurred, and the structure changed completely its structural stoichiometry. In particular, the atomic rearrangement obtained in the silicide slab resembles the Ni_2Si pattern [See Figure 28-a], besides having different chemical compositions. Particularly, we observe that some nickel atoms of the (011)Ni_3Si silicide seem to be placed on the sites that the silicon atoms have in the Ni_2Si bulk structure. To have a quantitative comparison of the similarity between the minimized (011)Ni_3Si silicide slab and the Ni_2Si pattern, we use the Iterative Rotations and Assignments (IRA) code [91]. For this, a distance is defined to analyze the similarity between the two structures. The results are shown in Figure 28-c. In this figure, the distance values range from 0 to 2.5. We observe that the Ni atoms belonging to the (011)Ni_3Si slab exhibit a distance value close to zero, meaning that these Ni atoms are placed in the same sites as in the Ni_2Si pattern. Contrary, we observe that most of the Si atoms of the (011)Ni_3Si have high distance values as they are not in right position from a chemical concern.

Based on the structural analysis made, we conclude that the (011)Ni_3Si structure seems to mimic the Ni_2Si structure when the (011)Ni_3Si/Si simulation box size is fixed at the Si lattice parameter and no box minimization is performed. This result is attributed to a stabilization mechanism that is produced due to the high elastic energy that is imposed on the (011)Ni_3Si slab.

Finite size effects

Before closing this chapter, we would like to highlight a technical issue related to our current calculations. Indeed, because of the computational of DFT calculations, a choice was made in terms of the slab thickness and it is important to evaluate the error that it imposes on our calculations. On the one hand, we assess the presence of the bulk regions on the silicide and silicon slabs after atomic and box minimization. For this, we analyze the atomic displacements that have occurred within the supercell. This analysis is shown in Figure 29, where we can observe the RMSE of the atomic displacements along the $\hat{z}$ direction when compared with the initial bulk positions. The silicide surface region and fixed silicon layers are not plotted. We can observe that the atomic displacements adopt an increasing linear trend on the silicon slabs. Here, the (011)Ni_3Si/Si and (001)-26Ni_3Si/Si interfaces which possess the largest and the smallest lattice mismatches among the four considered interfaces also present the largest and smallest slopes respectively. In the meantime, for the (001)Ni_2Si/Si and the

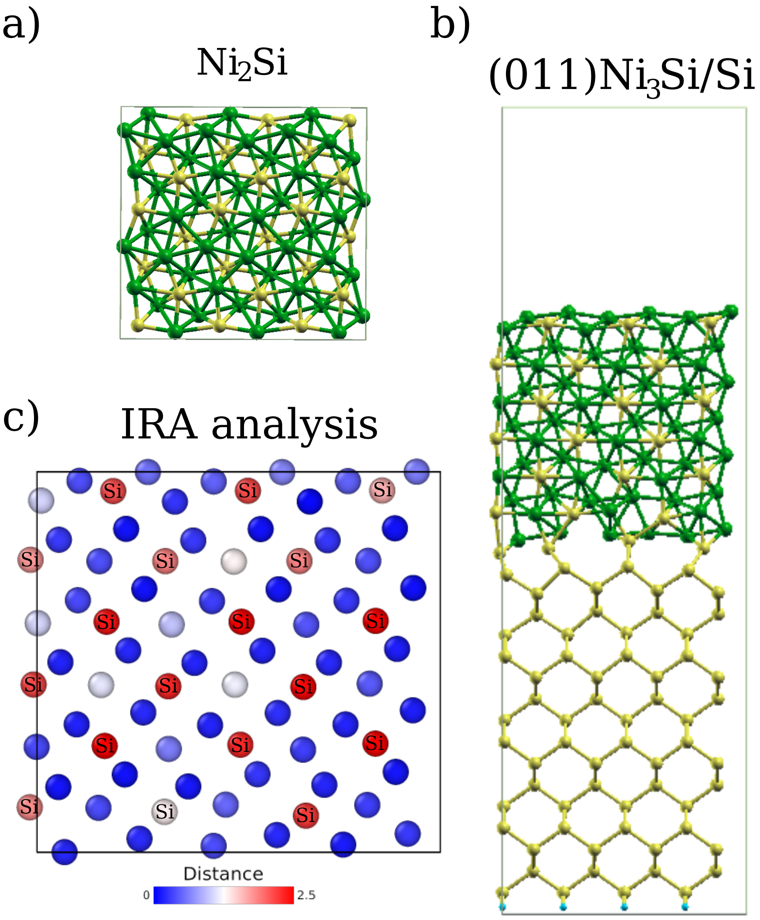

Figure 28: Structural analysis of the (011)Ni_3Si/Si interface at Si lattice parameter. a) Ni_2Si pattern b) atomic relaxed interface c) structural comparison between (011)Ni_3Si slab and Ni_2Si pattern by using IRA code, a distance value in a range from 0 to 2.5 is defined to evaluate the similarity between two structures. These distances are plotted in gradient color coding from blue to red, where blue and red indicate high and low similarity, respectively.

(001)NiSi/Si interfaces which exhibit similar lattice mismatches, we find similar slopes for the RMSE in the $\hat{z}$ direction. As such, we note the correlation between the slope of the increase and the initial mismatch. After reaching the interface positions, the RMSE values decrease when the position of the atoms increases.

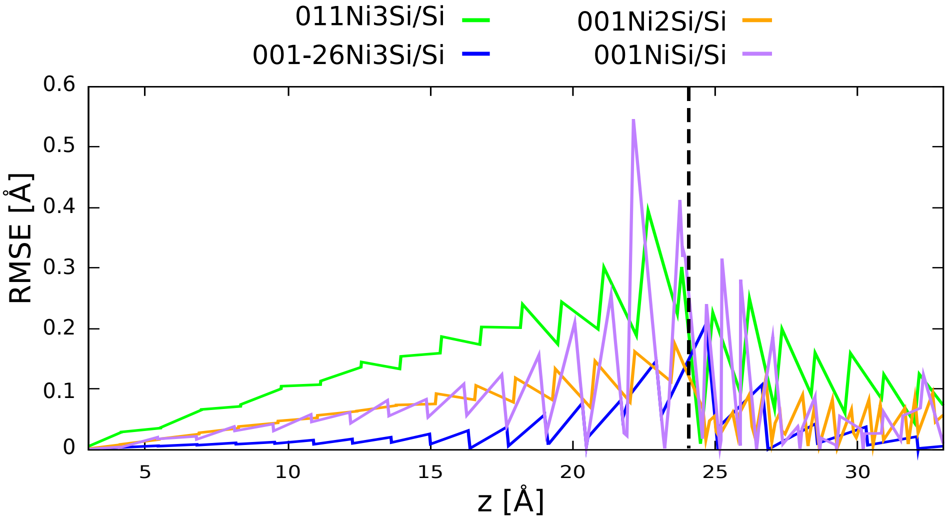

Figure 29: Atomic displacements occurred in $\hat{z}$ direction after atomic and box minimization of different interfaces. The analysis is made by means of the root mean square displacement error. A vertical dashed line indicates the interface positions before energy minimization.

4.3 Conclusions

The mechanisms for stabilizing nickel-silicide/silicon interfaces are thoroughly studied using DFT calculations combined with an analysis of structural and charge properties for selected interfaces. The choice of interfaces we have investigated is motivated by application considerations (fixed substrate, alloy orientation selection, etc.) and the need to develop an interatomic potential suitable for a comprehensive study of nickel silicide alloys.

Initially, a comparison of several properties of silicides and silicon is conducted to construct the interfaces, taking into account their orientations and stacking arrangements.

Then to study the stability of each silicide on the Si substrate, we applied energy minimization and analyzed the structural and charge properties of the relaxed interfaces. Structural analysis reveals that rotation step applied to reduce lattice mismatch can lead to significant dislocations in the interface regions. Total displacements are studied, and a detailed analysis of the contributions from silicide and silicon in the $\hat{x}$, $\hat{y}$, and $\hat{z}$ directions is performed, revealing a narrowing of the Si interface in the $\hat{z}$ direction for the (011)Ni_3Si/Si interface without the presence of dislocations. We observe that atomic displacements after interface minimization are accompanied by a modification of charge transfer in the interface regions, ranging from 1 to 2 electrons in magnitude, with the (001)-26Ni_3Si/Si interface exhibiting the smallest charge transfers and the (001)NiSi/Si interface exhibiting the largest. No correlation was found between charge transfers and total RMSE atomic displacements.

In future work, it would be necessary to study the thermodynamic properties to identify the energetically most favorable interfaces among different compositions of silicides. In conclusion, this preliminary study of nickel silicide-silicon interfaces reveals an evident link between interface structure, reconstructions, dislocations, atomic arrangements, chemical composition, etc. We emphasize the need for a dedicated study on interfaces using a more conventional protocol as encountered in computational materials science. In our study, we were clearly influenced by the imposed box size, the choice of only a few interfaces primarily for one orientation, and rigor in selecting terminations. In the future, automatic search algorithms should be employed to obtain a more comprehensive picture of interface structures.

However, it should be noted that the primary goal of this study is to create a database for constructing a new PLIP-type interatomic potential, which is described in the following chapter.

Chapter 5

Development of a linearized machine learning potential for the silicide/silicium interface

5.1 Introduction

To understand the silicidation process, it would be insightful to perform large-scale simulations of hundreds of atoms in the nanosecond regime. By initializing a simulation with an interface composed of nickel-rich silicide and silicon, one could observe how thermal activation can lead to the formation of each of the other silicide stoichiometries. However, such large-scale simulations can hardly be obtained with the current state of the art in terms of computational tools. When aiming for ab initio precision, it proves to be challenging: the formation of Ni silicide on the Si(001) substrate was studied by DFT-based MD simulations [37] with a system composed of only 191 atoms, not representative of an actual interface. When one wants to process larger systems with less precision, a classical interaction potential is an alternative: a modified embedded atom model (MEAM) [74] was developed for NiSi systems which remains inaccurate when it comes to delicate silicidation processes. In this context, machine-learning interaction potentials (MLIP) have been proposed in recent years to bridge the gap between the quantum accurate models and classical potentials [92]. In general, MLIP relies on a set of DFT calculations from which a database is constructed using forces and energies of given structures and on a machine-learning engine to train the interaction potential. The success of these methods can be seen in the large variety of materials that they managed to model including pure metals [93], organic molecules [94], water [95], amorphous materials [96], and hybrid perovskites [97].

The main aim of this chapter is to develop a linearized machine-learning interaction potential for investigating the silicidation process. To reach our objective, we have chosen to employ the Physical LassoLars Interaction Potential (PLIP) which has been previously introduced and explained in detail in the Method chapter. To assess the accuracy of the PLIP model, we conduct a comprehensive comparison with DFT calculations in terms of forces, energy, and various physical properties. After the validity of the model is established, we perform MD simulations to explore the effects of thermal activation at the silicide/Si(100) interfaces. Our analysis encompasses the identification of the crystalline structure, concentration profiles, as well as diffusion coefficients.

5.2 Database

The development of a MLIP describing the silicidation process is challenging because the structures to be simulated present a large variety of interatomic interactions. On the one hand, our model must accurately retrieve both bulk and interface systems. On the other hand, the chemical nature of the interactions also varies with the stoichiometry ranging from covalent silicon to metallic nickel and passing through mixed bonding in silicide. As such, the developed MLIP model requires a large variety of structures to account for this complexity. In this section, we describe the construction of the database used for the generation of different gradually improved versions of our MLIP.

To establish the database, we use the procedure shown in Figure 30.

- As a starting point, initial structures of interests are selected and minimized with DFT calculations (see in Figure 30-a)).
- Then, we apply MD simulations to melt the selected structures with a ramp of temperature (Figure 30-b)).
- Next, using DFT calculations, we compute the quantum accurate forces for snapshots that are selected along the MD simulation (see Figure 30-c)).
- Finally, we collect the position of atoms in each snapshot along with the corresponding forces to train the machine-learning model (see Figure 30-d).

In our case, the MD simulations are first performed using a MEAM potential [74]. Two bulk nickel-silicide phases Ni_2Si and NiSi, pure Ni, and pure Si are considered as initial structures. Here, box sizes of roughly 15 Å of side are used, which contain around 250 atoms per structure. We note that the MEAM potential is so inaccurate for Ni_3Si that we could not include this stoichiometry

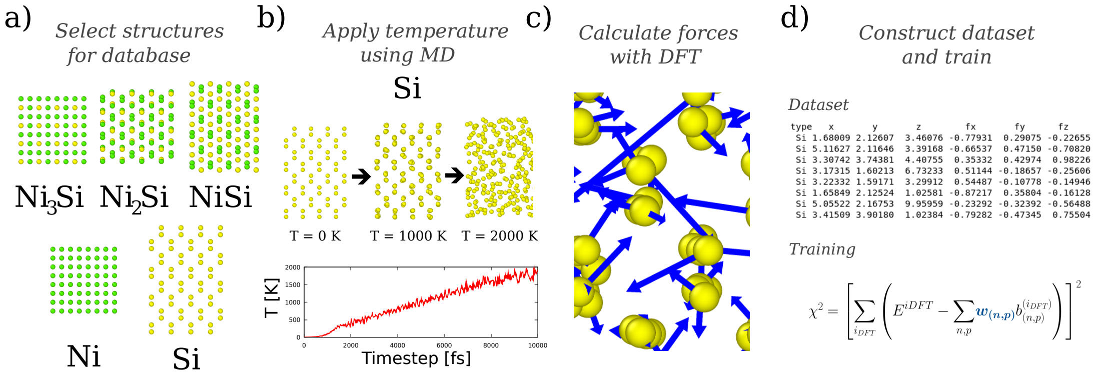

```
type    x        y         z        fx        fy        fz
 Si 1.68009 2.12607  3.46076 -0.77931  0.29075 -0.22655
 Si 5.11627 2.11646  3.39168 -0.66537  0.47150 -0.70820
 Si 3.30742 3.74381  4.40755  0.35332  0.42974  0.98226
 Si 3.17315 1.60213  6.73233  0.51144 -0.18657 -0.25606
 Si 3.22332 1.59171  3.29912  0.54487 -0.10778 -0.14946
 Si 1.65849 2.12524  1.02581 -0.87217  0.35804 -0.16128
 Si 5.05522 2.16753  9.95959 -0.23292 -0.32392 -0.56488
 Si 3.41509 3.90180  1.02384 -0.79282 -0.47345  0.75504
```

Figure 30: Schematic representation of the procedure used for the generation of a database. a) Targeted structures are selected b) Molecular dynamics calculations of melting are performed on the selected structures and the evolution of the system is collected in a set of structures c) Forces are calculated in these structures using DFT d) Positions and forces are all collected and used in the training procedure.

yet. Then, each crystal structure is melted using a temperature ramp from 0 K to 2000 K during 0.01 ns with a time step of 1 fs. We extracted 100 snapshots for each melting path and computed forces with the same DFT framework as in our previous chapter. With the obtained database, we construct a first model that we will call *PLIP-v1*.

Then, with MD simulations based on PLIP-v1, we create a second loop of melting bulk database using the same temperature range and structures yet including this time Ni$_3$Si. We call this version *PLIP-v2*. Using PLIP-v2, we also added structures based on different silicide/Si interfaces that were initially obtained in the previous chapter. In particular, we considered the (011)Ni$_3$Si/Si, (001)Ni$_2$Si/Si, and (001)NiSi/Si interfaces. We recall that, according to the reference system defined in the previous chapter, these interfaces have thicknesses of roughly 15 Å in $\hat{x}$ and $\hat{y}$ directions, while 35 Å in $\hat{z}$ direction. The structures contain around 600 atoms, each. The two bottom layers of the silicon substrate are kept fixed to reproduce bulk behavior, but this time no monolayer of hydrogen atoms is used in the training of the potential. A vacuum region of 15 Å is placed above the silicide slabs. Because the PLIP-v2 has never been trained on interfaces, their stability is very poor at this stage and run the MD simulation only at low-temperature (0-50 K). We obtained structures exhibiting only vibrations around equilibrium positions. With these snapshots, we created the potential version called PLIP-v3. Using this potential, a second loop of melting was generated in the interfaces where we could increase the temperatures up to 1500 K. After obtaining this so-called *PLIP-v4*, we performed final MD simulations at 1000 K where diffusion of Ni atoms is observed and the associated snapshots are included in the database to obtain the final version of MLIP denoted *PLIP-v5*.

In the context of database generation, the overall concept entails utilizing a classical model such as MEAM to sample structurally reasonable configurations. Then, the MLIP models are iteratively enhanced by including an increasing number of structures of various characteristics. In our study, we started with bulk simulations excluding one particular silicide phase. Then, we included that phase in the next version of the potential. Next, interface systems were considered beginning at very low temperatures and continuing with gradually higher temperatures.

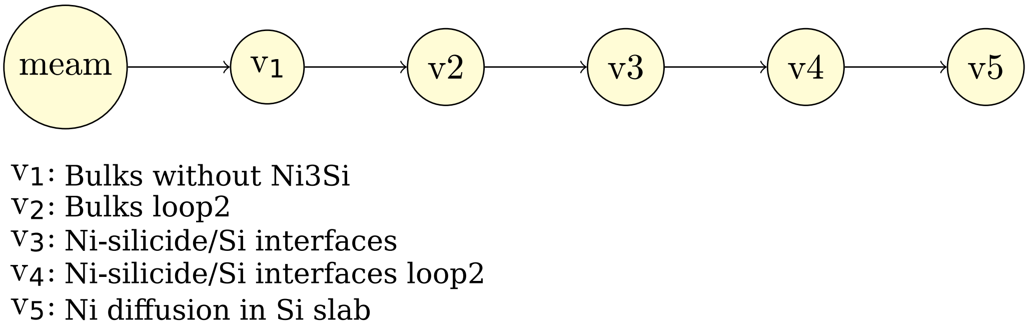

Figure 31: Diagram representation of the procedure used for the generation of different versions of our PLIP potential. Initially, a meam potential is used for the database generation, then the different versions of the potential are improved iteratively. The different versions of the PLIP potential generated are enumerated, and their databases are shown on the left-down part of the figure.

5.3 Results

Here, the results section is divided into two parts. In the first part, we perform measurements to validate the accuracy of the obtained potential. In this part, we show characteristics of the potential related to the training parts, structural properties, and the validity of the potential when a fixed temperature is applied to interface structures. In the second part, we investigate the silicide formation on at a silicide/silicon interface using equilibrium simulations at different temperatures.

5.3.1 Testing of the potential

We perform measurements to validate the accuracy of the potential created. The potential version selected to perform these measurements is the potential version PLIP-v$_3$, where the choice is discussed at the end of the chapter. Our analysis focuses on the predicted forces of our potential as well as measurements of structural properties when compared with DFT. The root mean square error (RMSE) is used for this purpose. In addition, we compare the results obtained with the potential version PLIP-v$_1$.

Training

To begin, we compare the forces predicted by our potential and those obtained with DFT when varying the α parameter of fitting. For that purpose, the database is split into two parts, training and testing, with a ratio of 95 % and 5 %, respectively. This analysis is made for the PLIP-v3 potential using RMSE measurements and the results are shown in Figure 32. PLIP-v$_1$ is also shown for comparison. On the left, the first observation is that both the testing and training parts reach similar values of RMSE, which suggests the lack of overfitting at this stage. In addition, one can observe that the decrease of the RMSE with α is inversely correlated with an increase of N_{coeff} (right part of the figure) which is the number of descriptors selected by the LassoLars algorithm. This behavior illustrates one of the advantages of using PLIP, which allows us to finely control the balance between accuracy and computational cost which is proportional to the number of selected descriptors. Finally, the convergence of both the RMSE and N_{coeff} for small values of α means that no additional descriptors can provide any improvement for the model. Here, the optimal value of α gives us a satisfying average difference of 0.16 eV/Å when compared with DFT.

Once we found an optimal value for the α parameter, we compare the forces predicted by our potential and those obtained with DFT for that given value of α. To make this comparison, forces are measured on the train and test sets. The forces predicted by the model and the DFT forces are plotted in $\hat{y}$ and $\hat{x}$ axes of Figure 33. Meam forces are also shown for comparison. In this figure, we can observe that, in the results obtained by PLIP, a linear relation between the PLIP and DFT forces is obtained for the structures in the train and in the test sets. In the meantime, when doing the same kind of measurements with the MEAM potential, results are way less convincing reaching RMSE values up to 150 eV/Å.

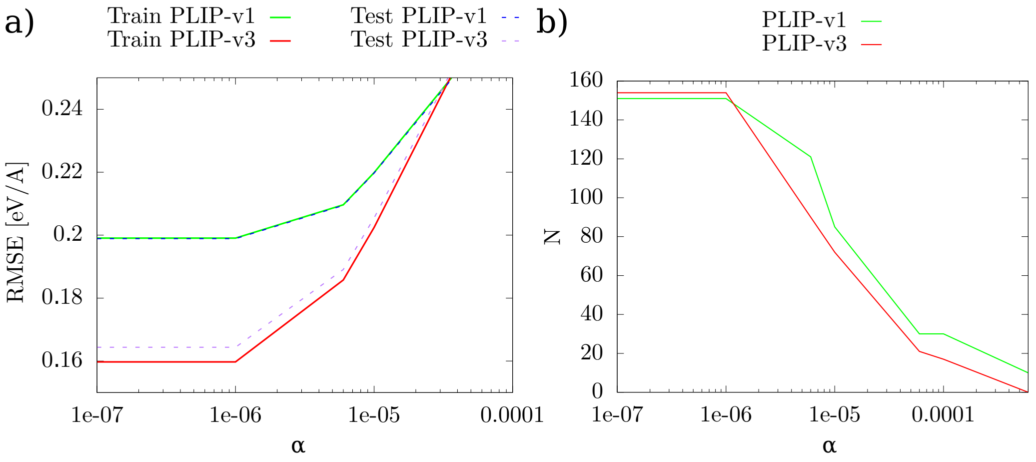

Figure 32: Measurements of accuracy and complexity of PLIP-v_3 potential as a function of a α parameter. On the left, the accuracy of the potential is studied using RMSE measurements that compare PLIP-predicted forces with DFT forces. On the right, the complexity of the potential is measured by the number of fitting parameters that the potential contains. PLIP-v_1 is shown for comparison.

Validation in bulk structures

To further validate the potential's accuracy we test bulk properties. For the lattice parameter prediction, we use the crystalline structures used in the bulk database, such as pure Ni, Ni_3Si, Ni_2Si, NiSi, and Si. In these structures, we apply atomic and box minimization and compare with DFT values through RMSE measurements. We additionally show the results obtained with the MEAM potential for comparison. The results are shown in Figure 34. In this figure, we can observe that the lattice parameter prediction has good accuracy, with values that are below 0.8 % for both, PLIP-v3 and PLIP-v1 potential versions. On the PLIP-v1 version, we can observe the values are lower than 0.4 %, exhibiting similar values between them. Particularly, the RMSE value for NiSi is close to zero, while the RMSE value for bulk Si is close to 0.2 %. On the PLIP-v3 version, we can observe that the RMSE values present variations depending on the chemical composition of the structures. Pure Ni and Si bulks present the highest values, while silicides values are lower (except for NiSi). Particularly, the Ni_3Si has a low RMSE value close to 0.1 %. In the meantime, we note than although the MEAM potential shows reasonable results for NiSi, it remains completely bad when it comes to the other two forms of silicide thus confirming the need of the obtained MLIP.

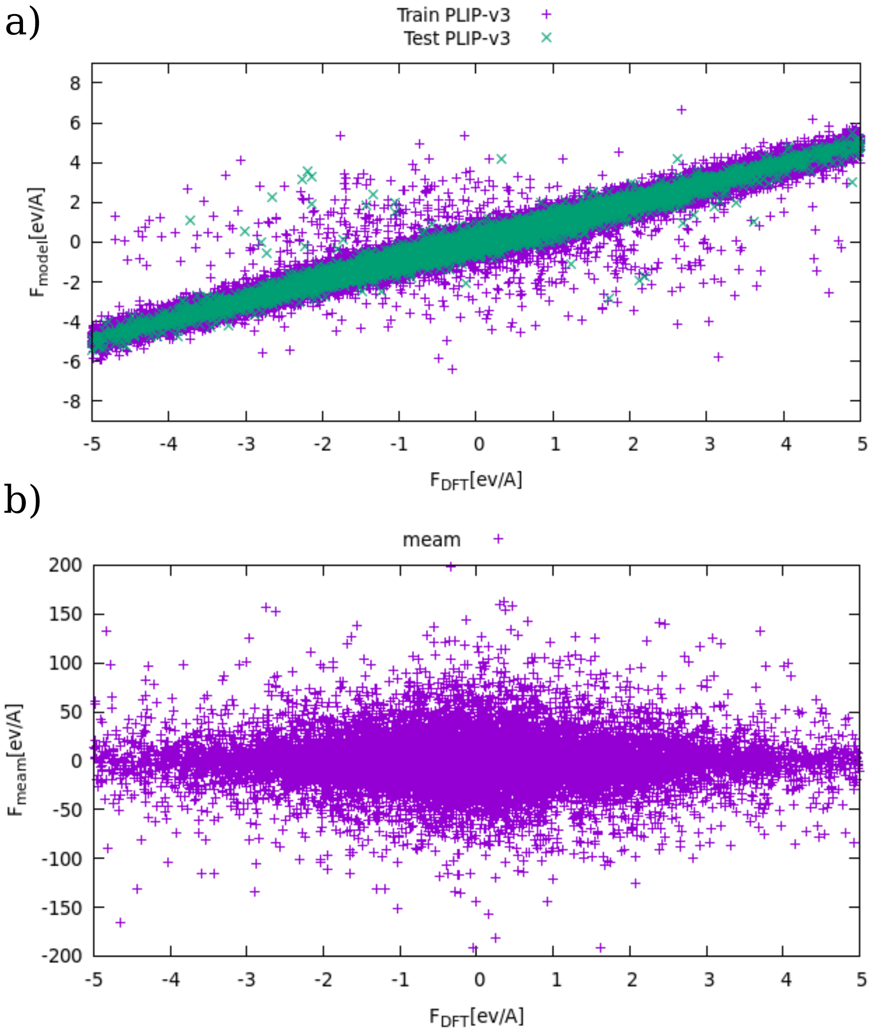

Figure 33: a) Comparison of predicted PLIP-v_3 forces with DFT forces when the α value is optimal. Forces are measured in the database structures, which are split into Train and Test sets. Forces on the Train and Test sets are shown in purple and green, respectively. b) Meam forces are shown for comparison.

After analyzing the lattice parameter prediction, we measure atomic relaxation predictions on bulk structures and compare with DFT. Results obtained with the MEAM potential are also shown. The results are shown in Figure 35. In this figure, we can observe that for the PLIP versions, the RMSE values measured have good accuracy in all cases. While the Ni_3Si, Ni, and Si structures have RMSE values that are close to zero. The other two forms of silicide show

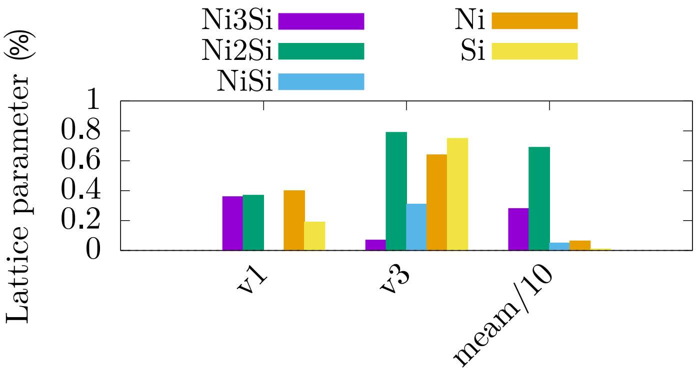

Figure 34: Histogram showing the lattice parameter prediction of the potentials PLIP-v3, PLIP-v1, and MEAM when compared with DFT values. The analysis is made for the bulk silicide structures Ni_3Si, Ni_2Si, and NiSi, and for pure Ni and Si structures. Values are shown in percentages. Particularly, MEAM values are divided by 10 for better visualization.

different results depending on the employed potential. In particular, while the PLIP-v1 exhibits errors up to 0.1 Å, the PLIP-v3 leads to improvements with values lower than 0.01 Å. On the results obtained using the MEAM potential, we note that although reasonable values are obtained for the pure Ni and pure Si structures, the relaxation prediction in the silicides structures is approximately five times larger when compared with the results obtained by PLIP. At this stage, we believe that we have evidence to justify the need of PLIP in bulk structures, particularly in bulk silicides.

Next, we study the bulk modulus prediction when compared with DFT values. Calculations were done using the standard LAMMPS procedure which is detailed in the following reference [98]. The results are shown in Figure 36. With PLIP-v1, we can observe that the silicide structures present higher values when compared with pure Ni and Si, having the NiSi structure the highest value. Particularly, the bulk modulus increases as the nickel concentration decreases on the silicide structures. On the other hand, the pure Ni and Si structures present values that are close to 10 and 20 %, respectively. With PLIP-v3, we can observe that the bulk modulus prediction is highly improved. Here, we observe that the Ni_3Si, Ni_2Si, and Ni structures have values close to 10 %, while the NiSi has a value close to 5 %. Particularly, the Si value has a value close to 30 %.

After studying bulk modulus prediction, we study atomic relaxation prediction after adding a vacancy to the bulk structures. For this purpose, single vacancies are created considering all the possible sites in all the structures. After each vacancy is created, atomic relaxation is applied with PLIP and compared

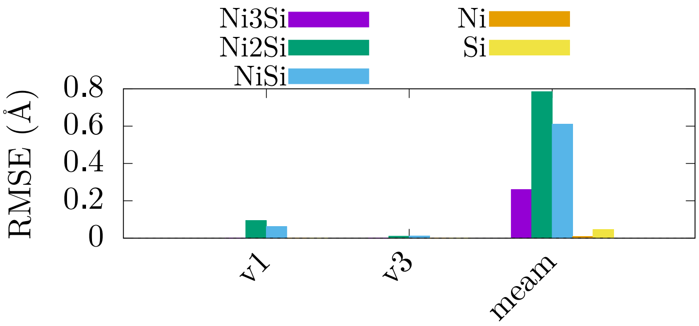

Figure 35: Atomic relaxation prediction performed using the PLIP-v1 and PLIP-v3 potentials and compared with DFT. The comparisons are made by RMSE measurements of the atomic displacements that occurred when PLIP relaxation is applied in a DFT-relaxed structure. The analysis is made for the bulk silicide structures Ni_3Si, Ni_2Si, and NiSi, and for pure Ni and Si structures. Atomic relaxation is applied with simulation boxes fixed at DFT values and only the maximum RMSE values obtained are shown. RMSE values are shown in Å.

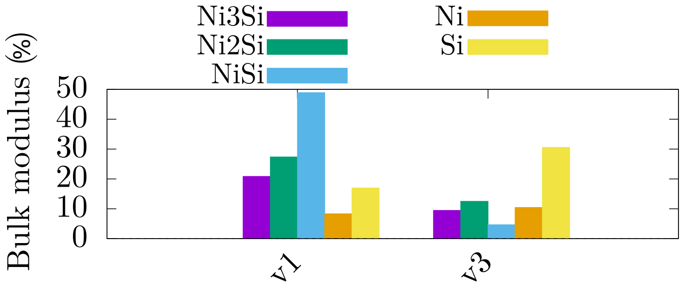

Figure 36: Bulk modulus prediction performed using the PLIP-v1 and PLIP-v3 potentials and compared with DFT. The analysis is made for the bulk silicide structures Ni_3Si, Ni_2Si, and NiSi, and for pure Ni and Si structures. The comparisons are made by RMSE measurements shown in percentage.

with DFT results. The RMSE maximum values obtained for each structure are shown in Figure 37. With PLIP-v1, we can observe that the Ni_3Si and the pure Ni structures have the lowest values which are lower than 0.05 Å, while the Ni_2Si, NiSi, and pure Si structures have the largest values, which are close to 0.2 Å. With PLIP-v3, the values of the Ni_3Si, pure Ni, and pure Si structures remain mostly unchanged but an improvement of roughly 0.1 Å is observed in the Ni_2Si and NiSi structures thus justifying the need for PLIP-v3.

Another additional test consists in comparing the atomic relaxation following a random displacement inside the bulk structures. The idea is to measure

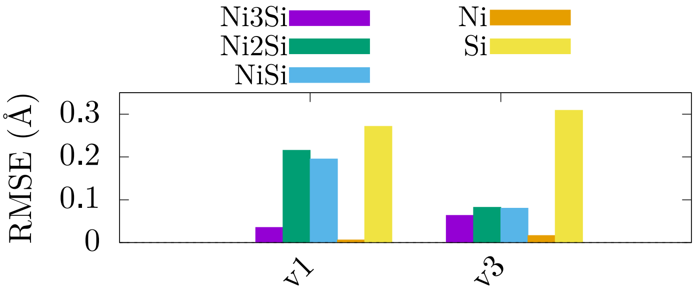

Figure 37: Atomic relaxation prediction performed using the PLIP-v1 and PLIP-v3 potentials when vacancies exist in the structures. The PLIP relaxed structures are compared with DFT relaxed structures. The analysis is made for the bulk silicide structures Ni_3Si, Ni_2Si, and NiSi, and for pure Ni and Si structures. Atomic relaxation is applied with simulation boxes fixed at DFT values and only the maximum RMSE values obtained are shown. RMSE values are shown in Å.

the capability of the potential to recover the crystalline configurations after such a random geometric perturbation in the system. For this, we apply random displacements to all the atoms contained in the systems in the three spatial dimensions. Here, the displacements are sampled from values between -0.3 to 0.3 Å. After atomic relaxation is performed we compare with the crystalline structures predicted by DFT. The RMSE maximum values obtained for each structure are shown in Figure 38. With PLIP-v1, we can observe that the Ni_3Si, Ni, and Si structures have the lowest values, which are close to 0.02 Å, while the Ni_2Si and the NiSi structures have the largest values, which are close to 0.1 Å. Similar to previous tests, the PLIP-v3 allows reaching lower values of the RMSE when compared with PLIP-v1 with all the structures having values close to 0.02 Å.

Validation in silicide/silicon interface structures

As mentioned in the procedure of the creation of the different versions of the potential, silicide/silicon interfaces were added to the database of the PLIP-v3 version. For this, we considered the minimized (011)Ni_3Si/Si, (001)Ni_2Si/Si, and (001)NiSi/Si interfaces obtained in the previous chapter. To validate the accuracy of the PLIP-v3 version in these interface structures, we first study the force prediction in one of these interfaces and compare with DFT. The results are shown in Figure 39, where we also include the results obtained by MEAM potential. In this figure the forces predicted by PLIP-v3 version has been multiplied by a factor of 10.0 for better visualization, while MEAM forces divided in a

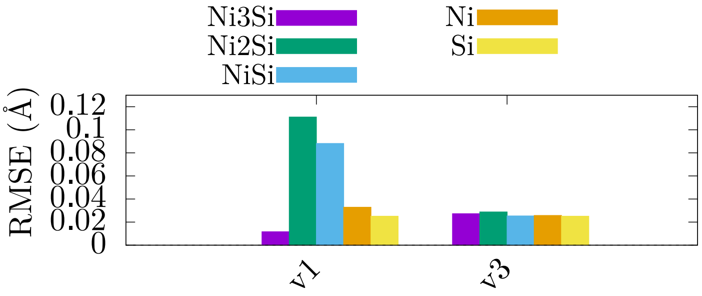

Figure 38: Atomic relaxation prediction performed using the PLIP-v1 and PLIP-v3 potentials when random displacements are applied in the structures. Initially, random displacements are applied in all the atoms of a determined structure, then PLIP relaxation is applied are compared with DFT relaxed structures. The analysis is made for the bulk silicide structures Ni_3Si, Ni_2Si, and NiSi, and for pure Ni and Si structures. Atomic relaxation is applied with simulation boxes fixed at DFT values and only the maximum RMSE values obtained are shown. RMSE values are shown in Å.

factor of 10.0. On the results we observe that for both potentials, the largest differences of the forces when compared with DFT are on the interface and surface regions. Notably, the forces predicted by the PLIP-v3 version are two orders of magnitude smaller than the MEAM forces, thus justifying without a doubt the development of the PLIP potential. Even further, when atomic relaxation was applied in this interface by using the MEAM potential (not shown here), the silicide and silicon slabs forming the interface got separated in more than 10 Å.

Next, we verify we are able to recover the box size predicted by DFT after box relaxation. In Figure 40, we can observe the simulation box values obtained in box relaxation prediction when compared with DFT. In this figure, we observe that the values are lower than 0.4 %. Particularly, we observe that the (001)NiSi/Si interface has a low value, which is around 0.1 %.

Finally, we study atomic relaxation prediction when random displacements are applied in the silicide/silicon interface structures. Here, the same procedure adopted in the creation of random displacements in bulk structures is adopted. After atomic relaxation is performed we compare the obtained structure with the minimized structures predicted by DFT. The RMSE maximum values obtained are shown in Figure 41. In the figure, we can observe all the values are less than 1 Å. Here, the (011)Ni_3Si/Si interface has a value around 0.7 Å, the (001)Ni_2Si/Si interface a value around 0.4 Å, and the (001)NiSi/Si interface a value around 0.9 Å. By comparing these results with the atomic relaxation prediction without the creation of random displacements (not shown here), we

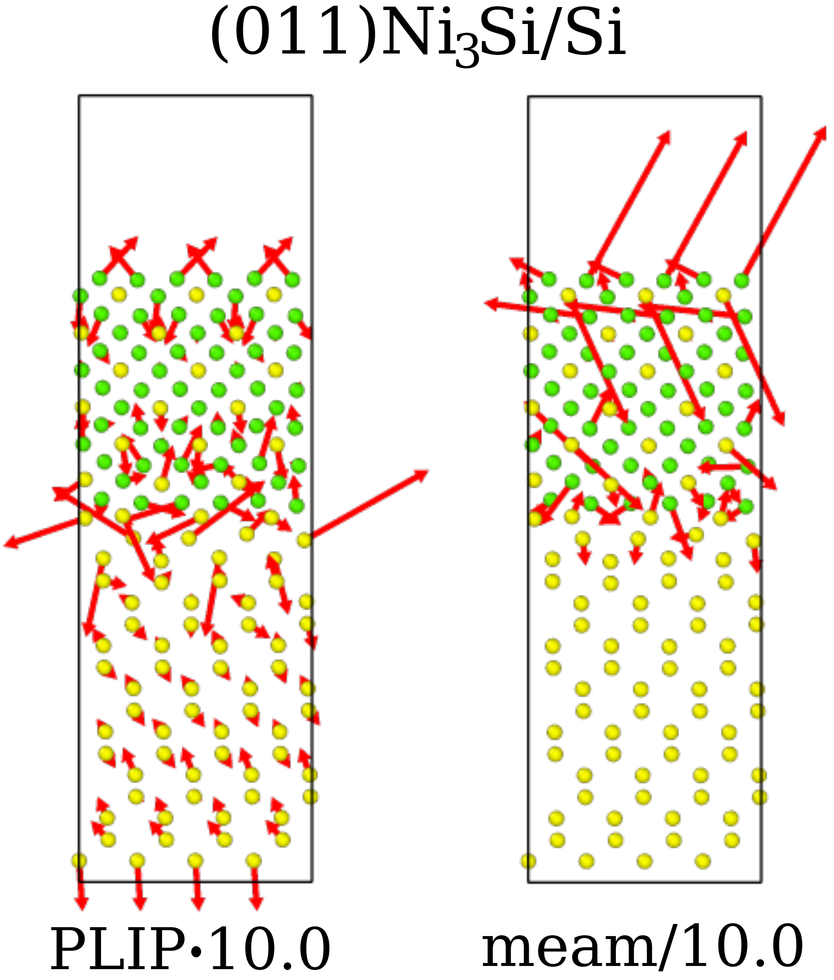

Figure 39: Difference of forces predicted by PLIP-v3 and MEAM potentials when compared with DFT. Force evaluation is performed in the (011)Ni$_3$Si/Si interface. Forces predicted by PLIP-v3 version has been multiplied by a factor of 10.0 for better visualization, while MEAM forces divided in a factor of 10.0. Nickel and silicon atoms are shown in green and yellow respectively.

observe negligible differences.

Overall, a key element of this series of tests lies in the inclusion of additional structures within the database, going from PLIP-v1 to PLIP-v3, which resulted in significant enhancements to the overall model and improved its applicability to diverse scenarios. In addition, we also showed that even with some of bulk structures, the previously employed MEAM potential is not accurate for the purpose of the intended study. In the end, our results demonstrate that PLIP-v3

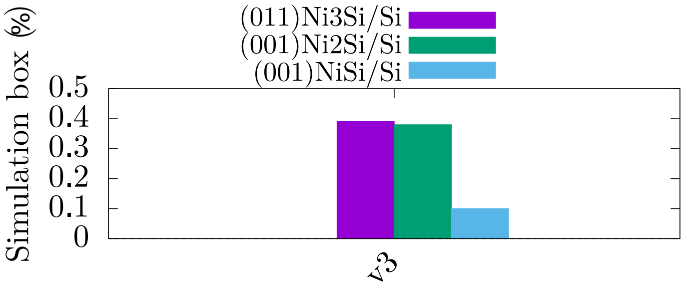

Figure 40: Box relaxation prediction performed using the PLIP-v3 potential on interface structures. Comparisons are made by using the relative difference error in simulation box sizes when compared with DFT values. The analysis is made in the (011)Ni_3Si/Si, (001)Ni_2Si/Si, and (001)NiSi/Si interfaces.

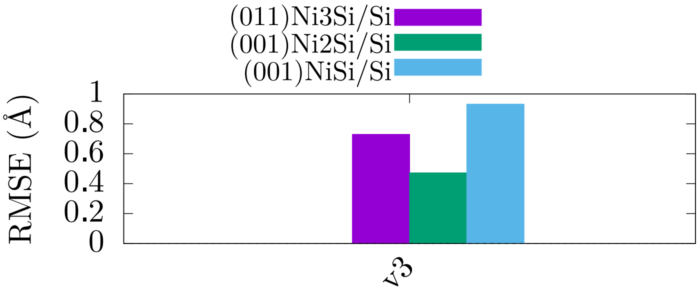

Figure 41: Atomic relaxation prediction performed in interface structures using the PLIP-v3 potential when random displacements are applied in the structures. Initially, random displacements are applied in all the atoms of a determined structure, then PLIP relaxation is applied are compared with DFT relaxed structures. The analysis is made in the (011)Ni_3Si/Si, (001)Ni_2Si/Si, and (001)NiSi/Si interfaces. Atomic relaxation is applied with simulation boxes fixed at DFT values and only the maximum RMSE values obtained are shown. RMSE values are shown in Å.

is able to reproduce silicide in various cases including different chemical compositions as well as different types of systems ranging from bulk to interfaces.

Validation of diffusion in silicide/silicon interface structures

To validate the accuracy of the potential under diffusion conditions, we perform equilibrium molecular dynamics (MD) simulations and compare the forces on atoms with those obtained from density functional theory (DFT). We use the

(011)Ni_3Si/Si, (001)Ni_2Si/Si, and (001)NiSi/Si interfaces. In this case, we eliminate the inclusion of a vacuum region, fix the top layer of the silicide slab and the bottom layer of the silicon slab, and remove periodic boundary conditions in the $\hat{z}$ direction. As such,there is no need to model exposed surface with vacuum, as they were never included in our database. In particular, MD simulations are run during 1.0 ns at three different temperatures (800, 950, and 1000 K). Forces are measured and compared with DFT every 0.25 ns. The RMSE average values obtained are found to vary slightly around the 0.18 eV/Å, regardless of the simulation time or applied temperature. In addition, it is worth noting that incorporating a second or third set of interface structures into the database (as in the versions PLIP-v4 and PLIP-v5), does not yield significant improvements in these RMSE average values. This finding supports the use of the version PLIP-v3 for the study of diffusion in silicide/silicon interfaces.

5.3.2 Analysis of diffusion process in a silicide/silicon interface structure

Once the validation of the potential is obtained, we study the silicidation process by performing fixed temperature simulations in a silicide/silicon interface. For this study, we use the (011)Ni_3Si/Si interface because, as shown in Chapter 3, it was found to be likely formed during nickel deposition in a silicon surface. The choice is also in agreement with experimental studies that report the Ni_3Si chemical composition as the first silicide phase formed before the thermal activation phase of the silicidation process is applied [24]. For these simulations, we increase the simulation box size in $\hat{z}$ direction in order to observe the diffusion process during long simulation times and to avoid finite size effects. Silicide and silicon thicknesses are increased to roughly 56 and 63 Å respectively, obtaining a box size of roughly 120 Å. We note that these large-scale simulations could only be done with the PLIP models which combines DFT accuracy with low computational costs. Additionally, as in the validation step of diffusion in the interface system, the vacuum region is deleted, the top and bottom layers of the silicide and silicon slabs are kept fixed respectively, and periodic boundary conditions in the $\hat{z}$ direction are deleted. We perform simulations using fixed temperatures of 800, 950, and 1000 K in a timescale that ranges between 0 to 2.2 ns. The results are shown in Figure 42, where the initial interface for all the simulations is shown in the top left part of the figure. Here, only 80 Å of the interface regions are shown.

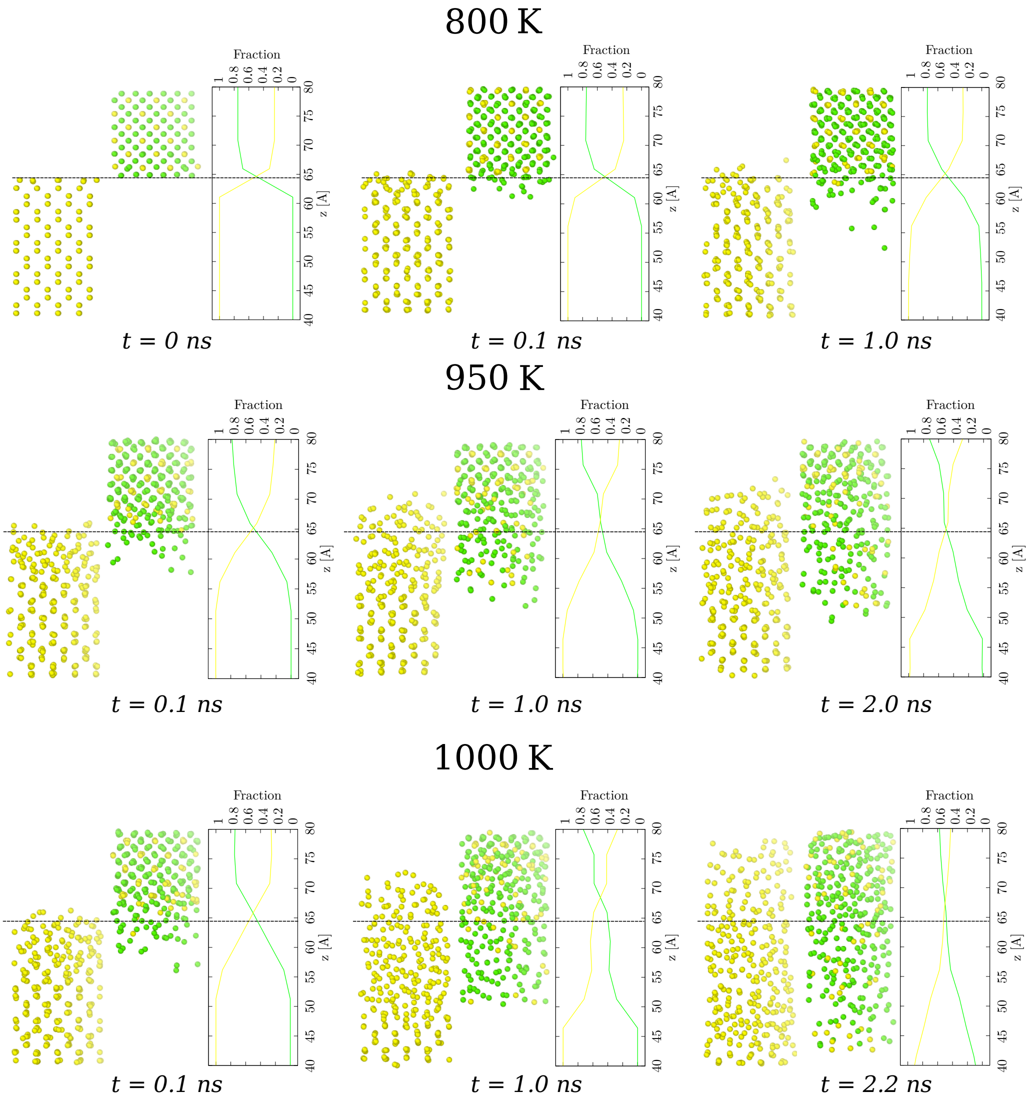

800 K

t = 0 ns

t = 0.1 ns

t = 1.0 ns

950 K

t = 0.1 ns

t = 1.0 ns

t = 2.0 ns

1000 K

t = 0.1 ns

t = 1.0 ns

t = 2.2 ns

Figure 42: Study of the silicidation process through assisted molecular dynamics simulations. Budgets of temperature are applied in a (011)Ni_3Si/Si interface. Simulations are performed using fixed temperatures of 800, 950, and 1000 K in a timescale that ranges between 0 to 2.2 ns. The initial configuration of the interface for all the simulations is shown in the top left part of the figure. The initial position of the interface is shown in all the structures. Atomic positions altogether with concentration profiles are shown at different times of the simulations. Only 80 Å of the interface regions are shown.

To analyze the results, we study the atomic positions altogether with their associated concentration profiles at the interface regions at different times. The initial position of the interface is shown in all the structures as reference. The first observation is that the diffusion of atoms from the silicide slab to the silicon slab occurs from the very beginning of the simulations (times lower than 0.1 ns) even for the lowest investigated temperate (800 K). This diffusion increases with temperature in terms of the number of atoms that have diffused as well as the penetration depth into the silicium substrate. In the simulation of 800 K we observe that at the 1.0 ns of simulation nickel atoms have diffused into the silicon slab and increased the nickel concentration of the region that goes from the 55 to the 60 Å of the interface. On the simulation of 950 K, we can observe that at 1.0 ns of simulation, a bigger amount of nickel atoms have diffused into the silicon substrate when compared with the simulation at 800 K. Indeed, after 1.0 ns, not only nickel atoms but also silicon atoms belonging to the silicide slab have diffused in the silicon substrate. Notably, we can also observe that silicon atoms belonging to the silicon slab diffuse to the silicide slab. On the simulation of 1000 K, we can observe that after at 1.0 ns similar results are obtained when compared with the simulation at 950 K, and after 2.2 ns, the diffusion region extends from the 40 to the 80 Å. In our results, we were able to prove the high capacity of nickel to diffuse into the silicon substrate, as known in the literature [12]. We point out that the diffusion of atoms from the silicon slab to the silicide slab is not a expected result at first look, due to the just mentioned nickel diffusivity. However, this result has been observed already in the literature by performing molecular dynamic simulations in a Ni/Si interface composed of roughly 100 of atoms [37]. Being able to reproduce these important trends gives account of the high capacity of the PLIP model.

To have quantitative measurements of the penetration velocity of the interface position for the applied temperatures, we measure the interface position as a function of the time. The position of the interface is determined by measuring when the decrease of the concentration profile in the silicon substrate reaches 5 %. In Figure 43, we can observe that, independently of the applied temperature, the interface position moves in discrete steps. This result is due to the methodology used in the measurements of the concentration profiles, which divides the simulation box into a finite number of bins. Due to a finite number of bins is used, the position of the interface remains constant until the number of atoms that have penetrated inside the bin that is most close to the interface position is enough to decrease the concentration profile by 5 %. On the 800 K simulation, we observe that the interface position decreases quickly until the 60 Å in the first 0.01 ns of the simulation, then the interface position remains constant with small oscillations appearing after 0.6 ns. The oscillation of the interface position is produced by the diffusion of nickel atoms that penetrate deeply into the silicon substrate but diffuse back to the interface position after a certain number of simulation steps. On the simulation at 950 K we can observe that, similar to the simulation at 800 K, the interface position decreases quickly until the 60 Å in the first 0.01 ns of the simulation, then the interface position decreases in two discrete steps that last approximately 0.2 and 0.4 ns respectively. After 0.7 ns, the interface position remains constant at 58 Å with small oscillations. On the simulation at 1000 K, we can observe that the interface position remains constant in the first 0.01 ns, then the interface position lows in four discrete steps of roughly 0.5 ns. In this simulation, the duration of the simulation is not sufficient to determine the convergence of the interface position.

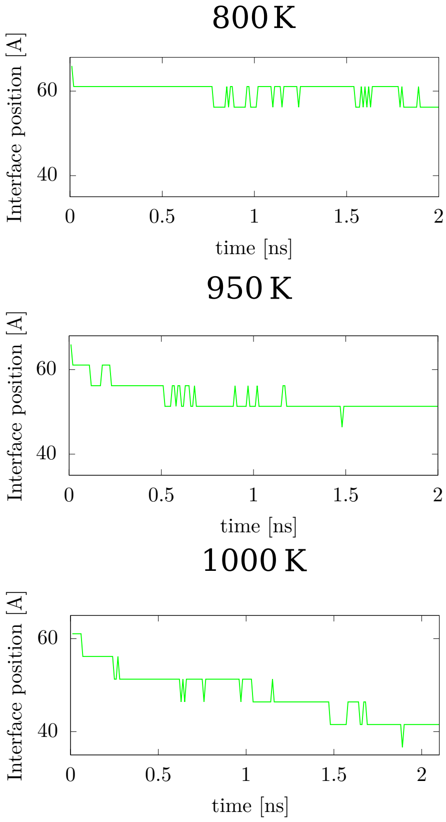

Figure 43: Position of the interface as a function of the time of simulation for the different applied temperatures. The position of the interface is estimated by measuring the decrease of the concentration profiles in the silicon substrates. The interface position is considered moved when the concentration on the silicon slab decreases by 5 %. The interface positions are reported in Å , while simulation time is shown in nanoseconds.

5.4 Conclusions

The nickel silicidation process after thermal activation is studied thanks to the development of an interatomic interaction potential of Machine Learning type based on linear regression methods (Lassolars). For this, we used the Physical LassoLars Interaction Potential (PLIP). The development of this potential is challenging due to the large variety of interatomic interactions that need to be simulated. The creation of the database was performed iteratively, starting with structures obtained using a MEAM potential and then including in the database more and more structures of various natures. At the end, the database accounts for bulk structures (such as bulk silicides, pure Ni, and pure Si) as well as silicide/silicon interface structures. For the construction of MLIP, we started by setting a parameter that controls the complexity of the potential. Here, the optimal value of this parameter gave us a linear correlation for the predicted forces when compared with DFT, with a satisfying average difference of 0.16 eV. We point out that the advantage of PLIP is the presence of this fitting parameter, that allows for controlling the accuracy and the complexity of the potential which are related to the computational cost of the simulations. Then, we tested the accuracy of potential in bulk structures by comparing with DFT on the basis of forces as well as numerous physical properties such as lattice parameter, bulk modulus, and atomic relaxation predictions. In this validation, we observed good accuracy in the lattice parameter prediction, with values that are below 0.8 %. We note that MEAM potential is not able to retrieve two of the three silicide chemical composition thus justifying the need for our PLIP model. In the bulk modulus prediction, we observed also small differences with DFT, reporting values lower than 10 % in all the cases, except for the pure silicon whose value was up to 30 %. On the atomic relaxation prediction, the creation of vacancies and random displacements were additionally considered, obtaining very small differences when compared with DFT. Here, the maximum RMSE values were lower than 0.1 Å in almost all the cases. We also tested the accuracy of potential in the silicide/silicon interfaces, by studying box relaxation, atomic relaxation as well as force prediction when a fixed temperature simulations are performed in the interfaces. Initially, we compared the forces predicted by our potential with DFT in one of the interfaces. Here, we also showed the forces predicted by the MEAM potential. Notably, when comparing with DFT, the differences in the forces predicted by our potential were two orders of magnitude smaller than the MEAM forces, thus justifying without a doubt the development of the PLIP potential. Even further, when atomic relaxation was applied in the interface by using the MEAM potential, the silicide and silicon slabs forming the interface got separated in more than 10 Å. In the results obtained by our potential we also obtained good accuracy in box relaxation prediction, which differences were lower than 0.5 % when compared with DFT. On the atomic relaxation prediction, the creation of random displacements was additionally considered. Here, the maximum RMSE values reported were up to 1.0 Å, where the main atomic displacements were produced at interface regions. To study the accuracy of the potential in dynamical conditions, force prediction during MD simulations lead RMSE of around 0.18 eV/Å which is similar to the fitting error obtained during the training.

Once the validation of the potential was obtained, we performed preliminary simulations of the silicidation process by applying fixed temperature MD with the (011)Ni_3Si/Si interface. Three temperatures were considered (800, 950, and 1000 K) with a duration up to 2.2 ns. To analyze the results, we studied the atomic positions along with the associated concentration profiles at the interface regions at different times. The first observation is that the diffusion of nickel atoms from the silicide slab to the silicon slab occurs from the very beginning of the simulations (times lower than 0.1 ns) even for the lowest temperature used (800 K). This diffusion increases with temperature in terms of the number of atoms that have diffused and the penetration depth. A remarkable result is that if the temperature is up to 950 K, not only nickel atoms but also silicon atoms belonging to the silicide slab diffuse in the silicon substrate, and the diffusion of atoms from the silicon slab to the silicide slab can also be observed. To have quantitative measurements of the penetration velocity of the interface position, we measure the interface position as a function of the time of the simulations. Here, our measurements reported the interface position moving in discrete steps independently of the applied temperature. However, we pointed out that these results are only related to the methodology used in the measurements since the concentration profiles are obtained after dividing the simulation box into a finite number of bins. On the simulation at 800 K, we observed that the interface position decreases quickly in the first 0.01 ns of the simulation, then the interface position remained constant with small oscillations. As discussed, the oscillations of the interface position are produced by the diffusion of nickel atoms that penetrate deeply into the silicon substrate but return to the interface position after a certain number of simulation steps. In the simulation at 950 K, we observed that the interface position decreases in two discrete steps that last approximately 0.2 and 0.4 ns respectively to the final interface position. After 0.7 ns of simulation, the interface position remains constant with small oscillations. In the simulation at 1000 K, we observed that the interface position decreases in four discrete steps of roughly 0.5 ns each. In this simulation, the time simulated does not allow us to determine the convergence of the interface position. Altogether, the results of these first large scale simulations using the PLIP are already promising and demonstrating that the overall methodology allows for observing diffusion at long timescales and with large number of atoms.

As a perspective, regarding the validation of the potential accuracy, we will test additional properties in both bulk and interface structures. These additional properties include mechanical properties and atomic relaxation prediction in the presence of interstitial atoms. We will also test surface properties such as surface energies and surface reconstruction prediction. In all the cases we will include the necessary structures in the database. Regarding the study of the silicidation process, we will perform a detailed characterization of the silicide formation in the simulations presented in this work. For this, we propose to use a structure recognition tool such as IRA, which was introduced in the previous chapter. Additionally, MD simulations at fixed temperatures will be performed using more silicide/silicon interfaces, such as the (001)Ni_2Si/Si interface.

Chapter 6

Conclusions

Going further in the miniaturization of devices and continuously improving their performance has become a necessity in the microelectronics. However, the reduction of the size of its components, such as transistors, still suffers from numerous limitations, and the selection of suitable materials in the manufacturing processes is crucial to ensure compatibility with the new emerging constraints. Within this context, the use of silicides has been significant, with different types of silicides being employed based on the technological application and transistor dimensions. Silicides are alloy compounds that are directly integrated into a silicon substrate, through a solid-state reaction between a metal and the silicon material. Particularly, to achieve increasingly thinner devices, nickel-based silicides became widely used. Among them, the NiSi silicide is one of the most promising silicides for the development of new technologies. However, the successful integration of NiSi silicide requires a perfect control over the formation of the silicide layer for its technological integration, which can only achieved with a comprehensive understanding of the silicidation process. An important fact is that the silicidation process is governed by the initial interactions between nickel and silicon during the deposition of nickel on the silicon substrate, requiring the need for a thorough comprehension of the process starting from its early stages. Then, once a thermal activation is performed, it is crucial to understand the associated phase transformation throughout the entirety of the silicidation process. the mechanisms underlying NiSi formation remain poorly understood and controlled.

In this thesis, we use atomic-scale simulations to understand the silicidation of nickel. A multilevel modeling strategy was employed, integrating first-principles calculations, molecular dynamics simulations, and machine learning methods, to describe key steps of the silicidation process. While Density Functional Theory calculations enable us to simulate the initial stages of the silicidation process during deposition, their high computational cost hinders the simulation of the activation phase. To simulate thermal activation, we opt for molecular dynamics. As at the beginning of the work, there was a lack of empirical interatomic potentials suitable for molecular dynamics simulations that can adequately model the silicidation process. It was necessary to develop a new interatomic potentials using a machine-learning interaction potentials (MLIP), which can bridge the gap between atomistic and quantum models, but their utilization necessitates the construction of an appropriate database. Using this MLIP we study the dynamics of atoms at the critical nickel silicide / silicon interface.

Initially, DFT calculations were performed to investigate the initial stages of the deposition process, aiming to obtain a realistic picture of the as-deposited material before thermal activation. Precise atomic-scale characterization was conducted, and potential pathways for nickel adsorption, diffusion, and insertion into the surface layers of the silicon substrate were identified, leading to the formation of a nucleation interface alloyed layer. We also employed the activation-relaxation technique (ART) coupled with the DFT methodology to characterize precisely transition states and identify new minimized structures. Our findings unambiguously demonstrated the formation of a native surface alloy during deposition, with nickel readily adsorbing and inserting onto clean Si(100) surfaces. Moreover, we successfully determined that this interfacial layer exhibits a nickel-rich composition, (011)Ni_3Si, which is favored by the ability of nickel atoms to penetrate the topmost layers of the silicon substrate. This finding is in agreement with experimental observations indicating the rapid formation of the Ni_3Si alloy at the Ni/Si interface, even at room temperature. We demonstrate that the formation of this alloy occurs thermodynamically without any activation barrier, once the Ni coverage on the surface is sufficient. Consequently, the as-deposited interface formed prior to the activation of the silicidation process can be represented as Si/Ni_3Si/Ni. Understanding this initial interface is crucial to understand the origin of the sequence of silicide phases that arise during the silicidation process and the state of the material before thermal activation, leading to the formation of the final silicide.

Subsequently, with the objective of constructing an ab initio database for the development of an interatomic machine learning potential, we modelled various silicide/silicon interfaces using DFT. We pointed out that the investigation of these interfaces is not only valuable for the establishment of the desired database, but also holds significance in understanding the silicidation process. In this context, the density functional theory (DFT) is an appropriate tool that can offer precise atomic scale characterization of the possible stabilization mechanisms taking place in the interfaces likely to appear during the silicidation process. For this reason, in this thesis, stabilization mechanisms on nickel-silicide/silicon interfaces were thoroughly investigated using DFT calculations combined with structural and charge properties analysis. Initially, a comparative analysis of the bulk properties of silicides and silicon was conducted, to construct the interfaces considering their orientations and stacking properties. Then, energy minimization was employed to assess the stability of each silicide on the Si substrate, and the structural and charge properties of the relaxed interfaces were studied. The structural analysis revealed that rotation of the slabs aimed at decreasing the lattice mismatch can be accompanied by large dislocations at the interface regions. Particularly, detailed analysis revealed a shrinking of the silicon slab when a nickel-rich silicide was used, without the presence of dislocations. Furthermore, the study of the interface charges after energy minimization revealed that the atomic rearrangements taking place at the interface regions were accompanied by a charge transfer in an order of magnitude that varied from 0 to 2 electrons. As a perspective, we want to study thermodynamical properties to identify the most energetically favorable interfaces between different silicides compositions. We have shown that several parameters play a key role in the formation of the interface layer, particularly its structure. On the basis of these results, we want to carry out an exhaustive study of possible interfaces using a more systematic and conventional study. This study could also be carried out with the help of tools such as automatic search algorithms to reach a more complete picture of the interface structures.

Upon completion of the investigation of nickel silicide/silicon interfaces, we worked on the development of a machine-learning interaction potential. The objective of this part was to develop the interaction potential capable of studying the thermal activation step of the silicidation process through assisted molecular dynamic simulations. To reach our objective, we employed the Physical LassoLars Interaction Potential (PLIP) model, which relies on linear regression methods (Lassolars). The development of this potential proceeded iteratively, starting with a Modified Embedded Atom Method (MEAM) potential and then including more and more structures with diverse characteristics into the database. The used database contained bulk structures (such as bulk silicides, pure Ni, and pure Si) as well as nickel silicide/silicon interface structures. During the creation of the potential, we pointed out the advantage of a fitting parameter in the PLIP model enabling precise control over the accuracy and complexity of the potential. Then, we tested the accuracy of potential within bulk structures by comparing it with numerous physical properties measured with DFT. In this validation, we observed good accuracy in terms of the lattice parameter prediction (<1 %), bulk modulus prediction (∼10 %), and atomic relaxation prediction (<0.3 Å) following both the creation of vacancies and random displacements. We also tested the accuracy of the PLIP model in the silicide/silicon interfaces, obtaining good accuracy in terms of box relaxation (<0.5 %), atomic relaxation (<1.0 Å), as well as force prediction in static and dynamical scenarios (0.18 eV/Å). An important fact is that just a minimal amount of interface database was required to reach satisfactory results, providing evidence for the transferability of the PLIP model. Following the validation of the potential, we studied the silicidation process by conducting equilibrium temperature simulations in the (011)Ni_3Si/Si interface. It is important to point out that we forced the simulations employing elevated temperatures higher than those typically employed in experimental setups. Moreover, no validation procedure was conducted to observe if the melting temperatures of the structures in the database are recovered, necessitating careful interpretation of the results. Still, we maintain that we have successfully elucidated the diffusion mechanisms inherent in the silicidation process. In particular, the first observation was that the diffusion of nickel atoms from the silicide slab to the silicon slab occurs from the very beginning of the simulations even for the lowest temperature used (800 K). A remarkable result is that as the temperature increases, not only nickel atoms diffuse but the diffusion of atoms from silicon to the silicide substrate is also observed. We found that irrespective of the employed temperatures, the interface position moves quickly at the beginning of the simulations, but then it converges to a constant value. As a perspective of this work, we will test additional properties such as mechanical properties, atomic relaxation in the presence of interstitial atoms, and surface properties. Furthermore, we will perform a detailed characterization of the silicide formation during the simulations by using a structure recognition tool. Expanding our investigation to encompass a wider range of nickel silicide/silicon interfaces, in particular the alloys encountered during silicidation such as the (001)Ni_2Si/Si interface, holds potential for gaining further insights.

This study is currently in its preliminary stages, and this thesis work could hold immense value in supporting experimentalists and addressing various objectives aligned with experimental and technological requirements. Understanding the transition from NiSi to undesired $NiSi_2$-rich phases would be particularly beneficial for technologists, as it would enhance their understanding of the effect of process parameters on the achieved material. By shedding light on this transition, we aim to contribute to technologists' knowledge and enable them to optimize their processes accordingly. Interface stability is another critical issue that we addressed in the introduction. Enhancing interface stability is of paramount importance, and we could help for significant contributions in this area. During experimental structural characterizations, so-called "diffusive" layers have been observed, the underlying mechanisms of which remain elusive. Understanding these layers is crucial, as they directly impact the final performance of devices. To gain insights into this phenomenon, we will again conduct a comprehensive study combining Density Functional Theory (DFT) and Machine Learning Molecular Dynamics (ML-MD). From a methodological perspective, we have demonstrated the added value of coupling DFT and MD methods with Machine Learning approach. Building upon the results obtained, we plan to expand the complexity of our systems. Specifically, we will investigate larger systems to explore the diffusion of nickel deep into the silicon. Additionally, we will introduce further complexity by studying a Ni/silicide/Si interface to investigate the role of the Ni layer as a reservoir capable of supplying Ni to the intermediate silicide layer. This approach will enable a more comprehensive understanding of the underlying processes and pave the way for further advancements in the field.

Bibliography

[1] More Moore. "International Roadmap for Devices and Systems: 2017 Edition". In: *IEEE Advancing Technology for Humanity* (2017).

[2] Ratnesh K Pandey et al. "New insights on Ni-Si system for microelectronics applications". In: *Microelectronic Engineering* (2022), p. 111871.

[3] Gordon E Moore et al. *Cramming more components onto integrated circuits*. 1965.

[4] Alessandra Alberti and Antonino La Magna. "Role of the early stages of Ni-Si interaction on the structural properties of the reaction products". In: *Journal of Applied Physics* 114.12 (2013), 11_1.

[5] Markku Hannula et al. "Fabrication of topographically microstructured titanium silicide interface for advanced photonic applications". In: *Scripta Materialia* 119 (2016), pp. 76–81.

[6] RW Mann and LA Clevenger. "The C49 to C54 phase transformation in TiSi2 thin films". In: *Journal of The Electrochemical Society* 141.5 (1994), p. 1347.

[7] C Lavoie et al. "Effects of alloying elements on cobalt silicide formation". In: *Journal of electronic materials* 31 (2002), pp. 597–609.

[8] Karen Maex. "Silicides for integrated circuits: TiSi2 CoSi2". In: *Materials Science and Engineering: R: Reports* 11.2-3 (1993), pp. vii–153.

[9] C Lavoie et al. "Towards implementation of a nickel silicide process for CMOS technologies". In: *Microelectronic Engineering* 70.2-4 (2003), pp. 144–157.

[10] A Valletta et al. "Surface-scattering effects in polycrystalline silicon thin-film transistors". In: *Applied physics letters* 82.18 (2003), pp. 3119–3121.

[11] Sung-Jin Choi et al. "High-performance polycrystalline silicon TFT on the structure of a dopant-segregated schottky-barrier source/drain". In: *IEEE Electron device letters* 31.3 (2010), pp. 228–230.

[12] Jeanette Lindroos et al. "Nickel: A very fast diffuser in silicon". In: *Journal of applied physics* 113.20 (2013), p. 204906.

[13] Liang Yin and Peter Borgesen. "On the root cause of Kirkendall voiding in Cu3Sn". In: *Journal of Materials Research* 26.3 (2011), pp. 455–466.

[14] Willian Guertler and G Tammann. "Metallographische Mitteilungen aus dem Institut für anorganische Chemie der Universität Göttingen. XXVI. Die Silicide des Nickels". In: *Zeitschrift für anorganische Chemie* 49.1 (1906), pp. 93–112.

[15] Tatsuya Tokunaga et al. "Thermodynamic assessment of the Ni–Si system by incorporating ab initio energetic calculations into the CALPHAD approach". In: *Calphad* 27.2 (2003), pp. 161–168.

[16] H Okamoto, PR Subramanian, and L Kacprzak. "ASM International: Materials Park, OH, 1990". In: *Google Scholar There is no corresponding record for this reference* ().

[17] GM Alonzo-Medina et al. "Understanding the thermal annealing process on metallic thin films". In: *IOP Conference Series: Materials Science and Engineering*. Vol. 45. 1. IOP Publishing. 2013, p. 012013.

[18] Ryuji Tomita et al. "Improvement on sheet resistance uniformity of nickel silicide by optimization of silicidation conditions". In: *Microelectronics Reliability* 53.5 (2013), pp. 665–669.

[19] Chang-Geun Ahn et al. "A two-step annealing process for Ni silicide formation in an ultra-thin body RF SOI MOSFET". In: *Materials Science and Engineering: B* 147.2-3 (2008), pp. 183–186.

[20] G Maity et al. "Growth of low resistive nickel mono-silicide phase under low energy Si ion irradiation at room temperature". In: *Thin Solid Films* 733 (2021), p. 138826.

[21] SS Lau, JW Mayer, and King-Ning Tu. "Interactions in the Co/Si thin-film system. I. Kinetics". In: *Journal of Applied Physics* 49.7 (1978), pp. 4005–4010.

[22] Jianbao Gao et al. "Dewetting of Ni silicide thin film on Si substrate: In-situ experimental study and phase-field modeling". In: *Acta Materialia* 223 (2022), p. 117491.

[23] M. Grégoire et al. "On the influence of Ni(Pt)Si thin film formation on agglomeration threshold temperature and its impact on 3D imaging technology integration". In: *Microelectronic Engineering* 271-272 (2023), p. 111937.

[24] Alessandra Alberti et al. “Low temperature formation and evolution of a 10 nm amorphous Ni–Si layer on [001] silicon studied by in situ transmission electron microscopy”. In: *Journal of Applied Physics* 105.9 (2009), p. 093506.

[25] Alessandra Alberti et al. “Pseudoepitaxial transrotational structures in 14 nm-thick NiSi layers on [001] silicon”. In: *Acta Crystallographica Section B: Structural Science* 61.5 (2005), pp. 486–491.

[26] EJ Van Loenen, JF Van Der Veen, and FK LeGoues. “Ni-Si mixing: A new model for low temperature silicide formation”. In: *Surface Science* 157.1 (1985), pp. 1–16.

[27] Yu-Jeng Chang and JL Erskine. “First phase nickel silicide nucleation and interface structure at Si (100) surfaces”. In: *Journal of Vacuum Science & Technology A: Vacuum, Surfaces, and Films* 1.2 (1983), pp. 1193–1197.

[28] R Kilper, S Teichert, and P Oelhafen. “In situ investigation of the formation of an intermixed phase at the Ni/Si (100) interface by photoelectron spectroscopic methods”. In: *Applied surface science* 123 (1998), pp. 550–554.

[29] DK Sarkar et al. “Role of buried ultra thin interlayer silicide on the growth of Ni film on Si (100) substrate”. In: *Applied Physics A* 70 (2000), pp. 681–684.

[30] L Ehouarne et al. “In situ study of the growth kinetics and interfacial roughness during the first stages of nickel–silicide formation”. In: *Microelectronic engineering* 83.11-12 (2006), pp. 2253–2257.

[31] Damien Connétable and Olivier Thomas. “First-principles study of nickel-silicides ordered phases”. In: *Journal of Alloys and Compounds* 509.6 (2011), pp. 2639–2644.

[32] Damien Connétable and Olivier Thomas. “First-principles study of the structural, electronic, vibrational, and elastic properties of orthorhombic NiSi”. In: *Physical review B* 79.9 (2009), p. 094101.

[33] Gianni Profeta et al. “Supersoft silicides: Ab initio study of (001) T Si surfaces and (001) Si/T Si (T= Fe, Co, and Ni) interfaces”. In: *Physical Review B* 70.23 (2004), p. 235338.

[34] Hua Wu, Peter Kratzer, and Matthias Scheffler. “Ab initio study of transition-metal silicide films on Si(001)”. In: *AIP Conference Proceedings* 772.1 (June 2005), pp. 311–312.

[35] T Nakayama and K Kobinata. “Physics of Schottky-barrier change by segregation and structural disorder at metal/Si interfaces: First-principles study”. In: *Thin Solid Films* 520.8 (2012), pp. 3374–3378.

[36] Tomoki Hiramatsu et al. “First-principles evaluation of penetration energy of metal atom into Si substrate”. In: *Japanese Journal of Applied Physics* 53.5 (Apr. 2014), p. 058006.

[37] M Christensen et al. “Formation of nickel-platinum silicides on a silicon substrate: Structure, phase stability, and diffusion from ab initio computations”. In: *Journal of Applied Physics* 114.3 (2013), p. 033533.

[38] Wonseok Jeong et al. “Efficient atomic-resolution uncertainty estimation for neural network potentials using a replica ensemble”. In: *The Journal of Physical Chemistry Letters* 11.15 (2020), pp. 6090–6096.

[39] Bing-Yue Tsui et al. “Improvement of the thermal stability of NiSi by germanium ion implantation”. In: *Journal of the Electrochemical Society* 157.2 (2009), H137.

[40] Chih-Ming Hsieh et al. “Thermal stability improvement of NiSi on gate by high dosage Germanium implantation”. In: *Electrochemical and Solid-State Letters* 12.6 (2009), H226.

[41] Chel-Jong Choi et al. “Effects of hydrogen implantation on the structural and electrical properties of nickel silicide”. In: *Journal of The Electrochemical Society* 149.9 (2002), G517.

[42] SL Chiu et al. “Effects of Ti interlayer on Ni/Si reaction systems”. In: *Journal of The Electrochemical Society* 151.7 (2004), G452.

[43] Tsung Lin Lee et al. “Highly reliable nickel silicide formation with a Zr capping layer”. In: *Electrochemical and solid-state letters* 6.5 (2003), G66.

[44] Tsung Lin Lee et al. “Improvement of junction leakage by using a Zr cap layer on a 30 nm ultrashallow nickel-silicide junction”. In: *Journal of The Electrochemical Society* 152.2 (2005), G158.

[45] Shigeaki Zaima et al. “Interfacial reaction and electrical properties in Ni/Si and Ni/SiGe (C) contacts”. In: *Applied surface science* 224.1-4 (2004), pp. 215–221.

[46] O Cojocaru-Mirédin et al. “Snowplow effect and reactive diffusion in the Pt doped Ni–Si system”. In: *Scripta materialia* 57.5 (2007), pp. 373–376.

[47] LL Xu et al. “Thermodynamic assessment of the Pt–Si binary system”. In: *Calphad* 32.1 (2008), pp. 101–105.

[48] An-Yuan Hou et al. “Atomic-scale silicidation of low resistivity Ni-Si system through in-situ TEM investigation”. In: *Applied Surface Science* 538 (2021), p. 148129.

[49] Tuan T Tran et al. "In-situ nanoscale characterization of composition and structure during formation of ultrathin nickel silicide". In: *Applied Surface Science* 536 (2021), p. 147781.

[50] W Kohn and Sham L J. "Self-Consistent Equations Including Exchange and Correlation Effects". In: *Physical Review* 140 (1965), A1133.

[51] Ben Leimkuhler and Charles Matthews. "Molecular dynamics". In: *Interdisciplinary applied mathematics* 39 (2015), p. 443.

[52] Pascal Friederich et al. "Machine-learned potentials for next-generation matter simulations". In: *Nature Materials* 20.6 (2021), pp. 750–761.

[53] Paraskevi Gkeka et al. "Machine learning force fields and coarse-grained variables in molecular dynamics: application to materials and biological systems". In: *Journal of chemical theory and computation* 16.8 (2020), pp. 4757–4775.

[54] V. Botu et al. "Machine Learning Force Fields: Construction, Validation, and Outlook". In: *J. Phys. Chem. C* 121.1 (Jan. 2017), pp. 511–522.

[55] Max Veit et al. "Equation of State of Fluid Methane from First Principles with Machine Learning Potentials". In: *J. Chem. Theory Comput.* 15.4 (Apr. 2019), pp. 2574–2586.

[56] Tobias Morawietz and Jörg Behler. "A Density-Functional Theory-Based Neural Network Potential for Water Clusters Including van der Waals Corrections". In: *J. Phys. Chem. A* 117.32 (Aug. 2013), pp. 7356–7366.

[57] Gabriele C. Sosso et al. "Understanding the thermal properties of amorphous solids using machine-learning-based interatomic potentials". In: *Mol. Simul.* 44.11 (July 2018), pp. 866–880.

[58] Ryosuke Jinnouchi et al. "Phase Transitions of Hybrid Perovskites Simulated by Machine-Learning Force Fields Trained on the Fly with Bayesian Inference". In: *Phys. Rev. Lett.* 122.22 (June 2019), p. 225701.

[59] Normand Mousseau et al. "The Activation-Relaxation Technique: ART Nouveau and Kinetic ART". In: *Journal of Physics B: Atomic, Molecular and Optical Physics* 2012 (2012), p. 925278.

[60] Antoine Jay et al. "Finding Reaction Pathways and Transition States: r-ARTn and d-ARTn as an Efficient and Versatile Alternative to String Approaches". In: *J. Chem. Theory Comput.* 16.10 (Oct. 2020), pp. 6726–6734.

[61] P Giannozzi et al. "QUANTUM ESPRESSO: a modular and open-source software project for quantum simulations of materials". In: *Journal of Physics: Condensed Matter* 21 (2009), p. 395502.

[62] Magali Benoit et al. “Measuring transferability issues in machine-learning force fields: the example of gold–iron interactions with linearized potentials”. In: *Machine Learning: Science and Technology* 2.2 (2020), p. 025003.

[63] David S. Sholl and Janice A. Steckel. *Density Functional Theory*. Mar. 2009.

[64] Eberhard Engel and Reiner M. Dreizler. *Density Functional Theory*. Berlin, Germany: Springer.

[65] Walter Kohn and Lu Jeu Sham. “Self-consistent equations including exchange and correlation effects”. In: *Physical review* 140.4A (1965), A1133.

[66] Peter E Blöchl. “Projector augmented-wave method”. In: *Physical Review B* 50.24 (1994), p. 17953.

[67] Georg Kresse and Daniel Joubert. “From ultrasoft pseudopotentials to the projector augmented-wave method”. In: *Physical Review B* 59.3 (1999), p. 1758.

[68] David Rodney and Christopher Schuh. “Distribution of thermally activated plastic events in a flowing glass”. In: *Physical review letters* 102.23 (2009), p. 235503.

[69] Marco Baiesi et al. “Graph theoretical analysis of the energy landscape of model polymers”. In: *Physical Review E* 80.1 (2009), p. 011905.

[70] Houssem Kallel, Normand Mousseau, and François Schiettekatte. “Evolution of the potential-energy surface of amorphous silicon”. In: *Physical Review Letters* 105.4 (2010), p. 045503.

[71] Laurent Karim Béland et al. “Kinetic activation-relaxation technique”. In: *Physical Review E* 84.4 (2011), p. 046704.

[72] Fedwa El-Mellouhi, Normand Mousseau, and Laurent J Lewis. “Kinetic activation-relaxation technique: An off-lattice self-learning kinetic Monte Carlo algorithm”. In: *Physical Review B* 78.15 (2008), p. 153202.

[73] Antoine Jay et al. “Activation–Relaxation Technique: An efficient way to find minima and saddle points of potential energy surfaces”. In: *Comput. Mater. Sci.* 209 (June 2022), p. 111363.

[74] Michael I Baskes, JE Angelo, and CL Bisson. “Atomistic calculations of composite interfaces”. In: *Modelling and Simulation in Materials Science and Engineering* 2.3A (1994), p. 505.

[75] Aidan P Thompson et al. “LAMMPS-a flexible simulation tool for particle-based materials modeling at the atomic, meso, and continuum scales”. In: *Computer Physics Communications* 271 (2022), p. 108171.

[76] Jörg Behler and Michele Parrinello. "Generalized Neural-Network Representation of High-Dimensional Potential-Energy Surfaces". In: *Phys. Rev. Lett.* 98.14 (Apr. 2007), p. 146401.

[77] Albert P. Bartók et al. "Gaussian Approximation Potentials: The Accuracy of Quantum Mechanics, without the Electrons". In: *Phys. Rev. Lett.* 104.13 (Apr. 2010), p. 136403.

[78] Gauthier Tallec et al. "Potentials based on linear models". In: *Quantum Chemistry in the Age of Machine Learning*. Walthm, MA, USA: Elsevier, Jan. 2023, pp. 253–277.

[79] Alexandra M. Goryaeva, Jean-Bernard Maillet, and Mihai-Cosmin Marinica. "Towards better efficiency of interatomic linear machine learning potentials". In: *Comput. Mater. Sci.* 166 (Aug. 2019), pp. 200–209.

[80] Bradley Efron et al. "Least angle regression". In: *Ann. Stat.* 32.2 (Apr. 2004), pp. 407–499.

[81] A Alberti, C Bongiorno, and P Alippi. "A. La Magna, C. Spinella, and E. Rimini". In: *Acta Crystallograph. B* 62 (2006), p. 729.

[82] Alessandra Alberti et al. "Critical nickel thickness to form silicide transrotational structures on [001] silicon". In: *Applied physics letters* 89.10 (2006), p. 102105.

[83] A Hemeryck et al. "Multi-scale modeling of oxygen molecule adsorption on a Si(100)-p(2×2) surface". In: *Journal of Non-Crystalline Solids* 353.5-7 (2007), pp. 594–598.

[84] C Jara Donoso et al. "A comprehensive atomistic picture of the as-deposited Ni-Si interface before thermal silicidation process". In: *Applied Surface Science* 361 (2023), p. 157563.

[85] K Toman. "The structure of Ni2Si". In: *Acta Crystallographica* 5.3 (1952), pp. 329–331.

[86] Yoshihiro Oya and Tomoo Suzuki. "The nickel-rich portion of the Ni-Si phase diagram". In: *International Journal of Materials Research* 74.1 (1983), pp. 21–24.

[87] F Bosselet et al. "Solid states solubility of aluminum in the δ-Ni2Si nickel silicide". In: *Materials Science and Engineering: A* 167.1-2 (1993), pp. 147–154.

[88] DF Wilson and OB Cavin. "Thermal expansion behavior of NiSi/NiSi sub 2". In: *Scripta Metallurgica et Materialia;(United States)* 26.1 (1992).

[89] C Kittel. "Introduction to solid state physics 7 Wiley New York". In: *Search Google Scholar Export Citation* (1996).

[90] Richard FW Bader. “A quantum theory of molecular structure and its applications”. In: *Chemical Reviews* 91.5 (1991), pp. 893–928.

[91] Miha Gunde et al. “IRA: A shape matching approach for recognition and comparison of generic atomic patterns”. In: *Journal of Chemical Information and Modeling* 61.11 (2021), pp. 5446–5457.

[92] Pavlo O. Dral. *Quantum Chemistry in the Age of Machine Learning*. Walthm, MA, USA: Elsevier, 2022.

[93] I. I. Novoselov et al. “Moment tensor potentials as a promising tool to study diffusion processes”. In: *Comput. Mater. Sci.* 164 (June 2019), pp. 46–56.

[94] Tristan Bereau et al. “Non-covalent interactions across organic and biological subsets of chemical space: Physics-based potentials parametrized from machine learning”. In: *J. Chem. Phys.* DETC2018.1 (June 2018), p. 241706.

[95] Thuong T. Nguyen et al. “Comparison of permutationally invariant polynomials, neural networks, and Gaussian approximation potentials in representing water interactions through many-body expansions”. In: *J. Chem. Phys.* DETC2018.1 (June 2018), p. 241725.

[96] Volker L. Deringer and Gábor Csányi. “Machine learning based interatomic potential for amorphous carbon”. In: *Phys. Rev. B* 95.9 (Mar. 2017), p. 094203.

[97] Jonathan Lahnsteiner, Ryosuke Jinnouchi, and Menno Bokdam. “Long-range order imposed by short-range interactions in methylammonium lead iodide: Comparing point-dipole models to machine-learning force fields”. In: *Phys. Rev. B* 100.9 (Sept. 2019), p. 094106.

[98] M. Catti. “Calculation of elastic constants by the method of crystal static deformation”. In: *Acta Cryst. A* 41.5 (Sept. 1985), pp. 494–500.